Master of Science Thesis

Aerodynamic Analysis of Drag Reduction Devices for the Tractor-Trailer Gap

An Experimental and Numerical Analysis

William P.K.M. Mulkens

September 2, 2016

Aerodynamics

TU Delft

Faculty of Aerospace Engineering

Delft University of Technology

Aerodynamic Analysis of Drag Reduction Devices for the Tractor-Trailer Gap

An Experimental and Numerical Analysis

Master of Science Thesis

For obtaining the degree of Master of Science in Aerospace Engineering
at Delft University of Technology

William P.K.M. Mulkens

September 2, 2016

Faculty of Aerospace Engineering · Delft University of Technology

Delft University of Technology

DELFT UNIVERSITY OF TECHNOLOGY
DEPARTMENT OF AERODYNAMICS

The undersigned hereby certify that they have read and recommend to the Faculty of Aerospace Engineering for acceptance the thesis entitled **"Aerodynamic Analysis of Drag Reduction Devices for the Tractor-Trailer Gap"** by **William P.K.M. Mulkens** in fulfillment of the requirements for the degree of **Master of Science**.

Dated: September 2, 2016

Supervisors:

Dr.ir. B.W. van Oudheusden

Dr.ir. A.H. van Zuijlen

Dr.ir. G.M.R. Van Raemdonck

Dr. D. Ragni

Preface

This thesis represents the final achievement of my master Aerodynamics at the Delft University of Technology and of my all student years in Delft. It was a very challenging topic that required a lot of time, perseverance, technical skills and creativity; especially due to the demanding combination of an experimental and numerical analysis. However combining both experimental and numerical research also made it even more interesting.

I would like to thank a few persons, without them the result of this thesis would not have been the same. A lot of thanks go to my daily supervisor Sander van Zuijlen for all his time, helpful tips and knowledge. I would also like to thank my other daily supervisor Gandert Van Raemdonck for his inspirational passion and enthusiasm for heavy-duty vehicles.

I really appreciate all the help of Thomas Gheyssens, who learned me the basics of Fluent and our discussions in the basement helped me understanding the basics of bluff body aerodynamics. Simon Bal, Ragiel Wildvank, André Popinhak and Peter Duyndam, thank you for helping me out during the challenging wind tunnel campaign.

During the 12 months of my thesis I worked in the basement of aerodynamics, also known as the souterrain. Although that the room itself is rather depressing as it is underground, the people of the basement are great. Not only was it nice to have breaks together or to ask for someone's opinion about your thesis, I also really enjoyed our movie nights, our Friday atmosphere evenings, football matches and other fun events. Thanks to all the basement students: Remco, Jaap, Annemiek, Alberto, Edgar, Emel, Matthijs, Kitso, Steve, Sofia, Li, Woosik, Koen, Quan, Aman, Martyna, Thomas, Jordi, Tariq, Wiebe, Frouke, Olaf, Govert, Deborah, Andrea, Peter, Ankur, Fleur, Rucheet and Jiggar.

Finally I would like to thank my girlfriend, all my friends and my family. In particular my parents for supporting me in all kind of ways and for giving me the chance to study at the TU Delft and to give me the unique opportunity to spend a life-changing semester abroad in Illinois.

Summary

Heavy-duty vehicles are responsible for a significant part of the greenhouse gas emissions caused by the transportation sector. By improving the efficiency of these heavy-duty vehicles one will not only reduce the greenhouse gas emission, but also reduce the operational costs of the haulers. One way to improve the efficiency of these vehicle is by reducing the aerodynamic drag. This study will focus on the tractor-trailer gap as this is one of the main contributors to the total aerodynamic drag of the vehicle.

In the past quite some research has been done on drag reduction devices for the tractor-trailer gap of North-American heavy-duty vehicles. However, no extensive study has been found on this topic which focused on modern European heavy-duty vehicles. Therefore the goal of this study is to identify the best type of passive flow control drag reduction device for the tractor-trailer gap of a modern European heavy-duty vehicle considering various crosswind conditions. The test model applied in this study is based on real heavy-duty vehicles driving on the road in Europe and as well based on the GETS model. Five different baseline models are developed with a varying gap length and with and without extenders attached to the cabin of the vehicle. Multiple different drag reduction devices (also called add-on devices) are numerically and experimentally tested to analyze their effect on the drag coefficient of the five baseline models.

The numerical analysis method is performed with RANS simulations and the $\kappa - \omega$ SST closure model with the use of the software package Fluent. The sensitivity of the mesh is analyzed by performing a mesh sensitivity study. Furthermore the mesh is slightly adjusted when a yaw angle is applied.

With the experimental analysis more add-on devices can be tested as executing the numerical simulations is a very time-consuming process. Besides that, the experimental analysis acts as a validation for the numerical simulations. The experiment was carried out in the Open Jet Facility of the TU Delft at a Reynolds number of $8.5 \cdot 10^5$ based on the square root of the cross-sectional area of the model. During the wind tunnel campaign force and pressure measurements were performed on the model and also some flow visualization was applied with the use of tufts and a plume of smoke.

The numerical analysis showed that a significant amount of air flowing along the sides and the top of the cabin enters the tractor-trailer gap and impinges on the trailer frontal surface.

At a yaw angle of 0° two large counter-rotating vortices develop inside the gap. When the yaw angle is increased more air enters the gap at the windward side of the vehicle and inside the gap one can observe a distinct stream of air from the windward to the leeward side and only one large vortex. Furthermore depending on the configuration and the yaw angle flow separation can occur at the leeward side of the vehicle.

According to the numerical simulations the tractor-trailer gap of a modern European heavy-duty vehicle (S-E baseline model) is responsible for only 15 drag counts at a yaw angle of 0°. When the gap length is increased up to a normalized gap length of 0.688 (L-E baseline model), the drag caused by the tractor-trailer gap increases up to 87 drag counts. The CFD results showed that this goes together with an increase of the average pressure coefficient on the trailer frontal surface. For the S-E baseline model the average pressure coefficient is equal to -0.186, while it equals 0.041 for the L-E model. Furthermore a similar effect can be seen when the side and roof extenders are removed from the cabin of the S-E baseline model, then the average pressure coefficient on the trailer frontal surface increases with 0.033 and the drag caused by the gap increases with 27 drag counts. The numerical results also show that adding a splitter plate to the trailer frontal surface decreases the drag coefficient of the L-E model significantly, up to 339 drag counts (39.6%) at a yaw angle of 9°. The effect of the splitter plate on the drag coefficient of the S-E model is negligibly small (i.e. less than 1%).

The experimental results show that the wind averaged drag coefficient of the baseline model with a normalized gap length of 0.483 (M-E baseline model) is 46 drag counts larger than the wind averaged drag coefficient of the L-E baseline model. This is because the latter mentioned model has a lower drag coefficient at 6° and 9° yaw angle compared with the M-E baseline model. This counterintuitive behavior was also observed by Hammache and Browand (2004). According to the experimental results the splitter plate is one of the most effective add-on devices, with a maximum drag reduction of 138 drag counts for the M-E model. The effect of the add-on devices on the drag coefficient of the S-E model was smaller than the sensitivity of the performed tests. The possible gain of using add-on devices cannot be large as the results of the S-E baseline model lie close the results of the baseline model without a gap.

When the numerical results are compared with the experimental results it is clear that the CFD method has difficulties with correctly predicting the drag coefficient when a yaw angle is applied and when the effective gap length is large. The hypothesis is that the numerical method is not capable of accurately predicting the onset of flow separation on the leeward side of the vehicle. Also the pressure coefficients on the model predicted by the numerical simulations do not match with the experimentally obtained data.

To summarize the splitter plate is one of the most effective add-on devices of all tested add-on devices. The difference in wind averaged drag coefficient between the S-E baseline model and the No Gap baseline model is negligibly small. In other words the potential gain of adding drag reduction devices on modern European heavy-duty vehicles is very limited. Finally it is important to note that RANS with the $\kappa - \omega$ SST closure model is often not capable of accurately predicting the drag and pressure coefficients when a yaw angle is applied.

Table of Contents

Nomenclature

Abbreviations

CFD	Computational Fluid Dynamics
CO	Cooling Unit
CSP	Cabin Splitter Plate
CVTD	Cross Vortex Trap Device
DES	Detached-Eddy-Simulation
DNS	Direct Numerical Simulation
GCM	Generic Conventional Model
GETS	Generalized European Transport System
HC	Horizontal Cylinders
L-E	Large tractor-trailer gap baseline model with extenders
LBM	Lattice Boltzmann Method
LES	Large Eddy Simulation
LSE	Large Side Extenders
M-E	Medium tractor-trailer gap baseline model with extenders
NG	No Gap baseline model without a tractor-trailer gap
NLR	Netherlands Aerospace Center
OJF	Open Jet Facility
PIV	Particle Image Velocimetry

RANS	Reynolds-Averaged Navier-Stokes
RE	Rounded Edges
S-E	Small tractor-trailer gap baseline model with extenders
S-NE	Small tractor-trailer gap baseline model without extenders
SAE	Society of Automotive Engineers
SBC	Sides Bottom Covered
SC	Sides Covered
SP	Splitter Plate
STC	Sides and Top Covered
URANS	Unsteady Reynolds-Averaged Navier-Stokes
VC	Vertical Cylinders

Greek Symbols

Δ	Difference	
μ	Dynamic viscosity	$[Ns/m^2]$
μ	Mean value	
ν	Kinematic viscosity	$[m^2/s]$
ρ	Density	$[kg/m^3]$
σ	Standard deviation	
τ	Solid blockage constant	
τ	Wall shear stress	$[Pa]$

Latin Symbols

A	Cross-sectional area	$[m^2]$
$\bar{C_T}$	Wind averaged drag coefficient	$[-]$
C	Duplex test-section area,	$[m^2]$
C_e	Effective nozzle area	$[m^2]$

C_f	Friction coefficient	$[-]$
C_p	Pressure coefficient	$[-]$
C_T	Drag coefficient in the longitudinal direction of the vehicle	$[-]$
ϵ_n	Nozzle blockage factor at the model	$[-]$
ϵ_{qn}	Nozzle blockage factor at the nozzle	$[-]$
ϵ_s	Solid blockage factor at the model	$[-]$
F	Force	$[N]$
$f_{x,y,z}$	Body forces (x, y, z components)	$[N]$
G	Gap length	$[m]$
H	Height	$[m]$
L	Length	$[m]$
p	Pressure	$[Pa]$
R_n	Hydraulic radius of duplex nozzle	$[m]$
Re	Reynolds number	[-]
S	Frontal area	$[m^2]$
t	Time	$[s]$
u, v, w	Velocity components in respectively x, y, z direction	$[m/s]$
u^*	Friction velocity	$[m/s]$
U_c	Blockage corrected velocity	$[m/s]$
U_m	Measured velocity	$[m/s]$
V	Model volume	$[m^3]$
V	Velocity	$[m/s]$
W	Width	$[m]$
x_m	Distance between the center of the model and the nozzle	$[m]$
x_s	Distance between source and the nozzle	$[m]$
y^+	Non-dimensional wall distance	$[-]$

Subscripts

∞	Free stream
δ	Boundary layer
m	Model

Chapter 1

Introduction

1.1 Background on road transportation

All around the world heavy-duty vehicles are transporting enormous amounts of cargo from one place to another. According to the European Commission 44.92% of the freight transport within the European Union in 2012 was road transport, significantly more than sea (37.17%), rail (10.80%), inland waterways (3.98%), pipelines (3.05%) and air (0.08%) (European Commission (2014)). If one takes a look at the CO_2 emissions the share of road transport is even bigger. As can be seen in Figure 1.1 in the year 2010 73.9% of the transport CO_2 emissions came from road transportation of which almost half was caused by heavy-duty vehicles and buses (Miller and Façanha (2014)). Therefore improving the efficiency of heavy-duty vehicles can have a big impact on the total emission of CO_2 worldwide.

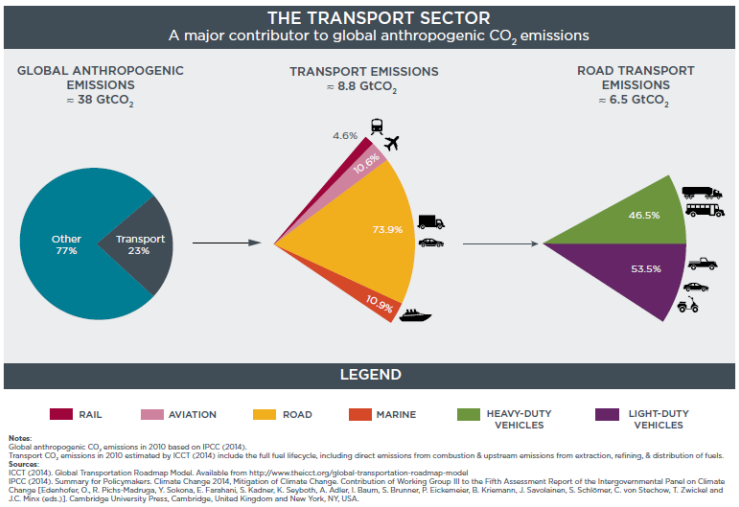

Figure 1.1: Transport life cycle CO_2 emissions in 2010 (Miller and Façanha (2014))

Besides the environmental reason, there is also an economical reason why improving the efficiency of heavy-duty vehicles is important. In general fuel and taxes on fuel are responsible for approximately one third of the total costs of EU haulers (Faber Maunsell (2008)). Although this number can vary a bit depending on the fuel price and other uncertainties, the cost of fuel is one of the biggest cost for haulers. So also in this perspective there is a large interest in making heavy-duty vehicles more efficient.

When driving at a constant speed, the energy coming from the fuel is mainly used to overcome two forces. On the one hand there is rolling resistance from the tires which are in contact with the road, on the other hand there is aerodynamic drag. The magnitude of both forces depends, among other things, on the velocity of the heavy-duty vehicle. Figure 1.2 shows that from approximately 65 km/h the aerodynamic drag is responsible for more than 50% of the total resistance force (ETSU and MIRA (2001)). The faster the vehicle goes, the bigger the aerodynamic drag component becomes in comparison with the rolling resistance. This shows that reducing the aerodynamic drag of heavy-duty vehicles is a good way to improve the road transportation in Europe and to reduce the costs of the operators.

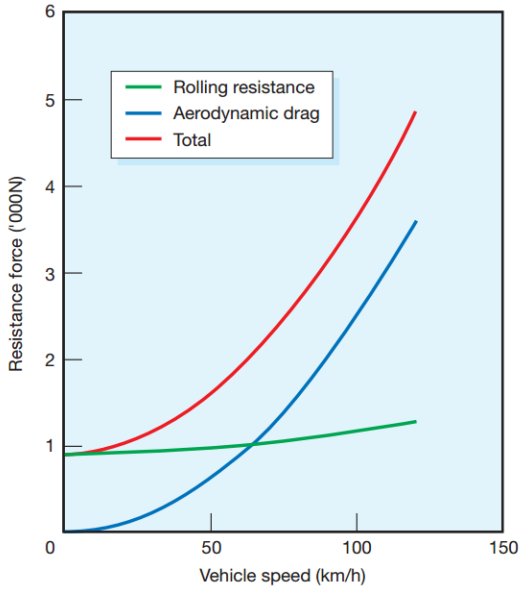

Figure 1.2: Force required to overcome the two main drag contributions (ETSU and MIRA (2001))

By reducing the aerodynamic drag of heavy-duty vehicles, one can significantly decrease the fuel consumption and greenhouse gas emissions of the vehicle. To find out how the aerodynamic drag can be reduced, first one has to analyze the aerodynamics of these vehicles and look at the state-of-art research performed on heavy-duty vehicles.

1.2 Bluff body aerodynamics

Due to operational constraints and legislations heavy-duty vehicles are in general very bulky designed. The shape of a heavy-duty vehicle is very angular and can be considered as a bluff body. The benefits of this shape are that it provides easy access, good viewing angles, fast loading of cargo, etc. However having a bluff body leads to high pressure drag. As was shown by Wood (2004) the pressure drag heavy ground vehicles experience can contribute up to 90% of their total aerodynamic drag (see Figure 1.3). Around the vehicle there are multiple over- and underpressure regions. For example when the heavy-duty vehicle is riding the air hits the front of the cabin creating a high stagnation pressure region. The same is valid for the front side of the wheels and the front of the trailer. However at the base of the trailer and the cabin there is an underpressure region. These differences in pressure cause pressure drag.

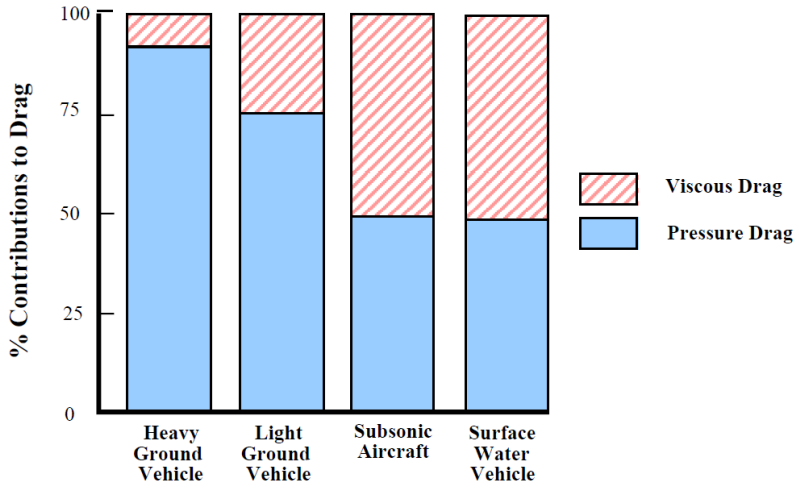

Figure 1.3: Contribution of pressure and viscous drag on total drag of vehicles (Wood (2004))

As was stated by multiple authors including Van Raemdonck (2012); Altaf et al. (2014) heavy-duty vehicles have large regions of separated flow. Behind the trailer the wake consists out of separated flow due to the rectangular rear shape. In the wake of the vehicle one can observe unsteady flow behavior where large recirculation bubbles develop as was mentioned by Choi et al. (2014). By Krajnovic and Davidson (2002) called as the development of a large vortex ring. In the past the corners of the cabin were sharp resulting in separated flow, but nowadays the manufactures of the cabin adjusted the radius of the corner to prevent separation and avoid additional drag (Choi et al. (2014); ETSU and MIRA (2001)). As was stated by Van Raemdonck (2012) the flow around heavy-duty vehicles is furthermore characterized by viscous effects in the thick turbulent boundary layer along the model.

The flow around heavy-duty vehicles is not only characterized by large regions of separated flow, but also by several other aerodynamic characteristics. First of all the flow can be assumed to be incompressible. The velocity of heavy-duty vehicles driving on the highway in Europe is around 85 km/h. At standard atmospheric conditions this will result in a Mach number lower than 0.3 and thus the flow can be assumed to be incompressible.

Besides the Mach number there is another important similarity parameter: the Reynolds number. This number represents the ratio between the inertia and the friction forces (see Equation 1.1).

$$Re = \frac{\rho V L}{\mu} \tag{1.1}$$

L stands for the characteristic length of the body, for heavy-duty vehicles often the width or the square root of the cross-sectional area is taken as the characteristic length. It is important to scale the flow analysis with the Reynolds number as this has an effect on the measured drag coefficient as was investigated by Storms et al. (2004). According to the same article a Reynolds number based on the width of the truck between 1 and 6 million is typical for real-life road conditions (Storms et al. (2004)). This is confirmed by others for example by Ortega et al. (2013) who performed a full-scale wind tunnel test at with a velocity of 25.9 m/s resulting in a Reynolds number based on the width of the truck of 4.6 million.

If you take a look at the aerodynamic drag of a heavy-duty vehicle four regions can be identified as the main contributors to the drag (Wood and Bauer (2003)). The biggest contributors to the drag are the forebody of the vehicle and the base drag, each responsible for approximately one third of the aerodynamic drag (Wood and Bauer (2003)). The gap region between the cabin and the trailer creates around 20% of the aerodynamic drag depending on the wind conditions (Wood and Bauer (2003)). The last important drag contributing region is the underbody and the wheels of the vehicle (around 13% of the aerodynamic drag) (Wood and Bauer (2003)). An overview can be seen in Figure 1.4. There are many academic articles available that discuss the reduction of underbody drag (Ortega and Salari (2008, 2004); Storms and Ross (2006)), forebody drag (Chen et al. (2013); Leuschen and Cooper (2006); Kim (2000)) and base drag (Seifert et al. (2008); Croll et al. (1996); Kim et al. (2004); Freeman and Roy (a,b); Ortega and Salari (2004); Browand et al. (2005)), but this research will investigate the tractor-trailer gap drag. By analyzing the flow behavior inside the tractor-trailer gap, the cause of this high drag contribution can be determined and a solution can be found in order to decrease the tractor-trailer gap drag.

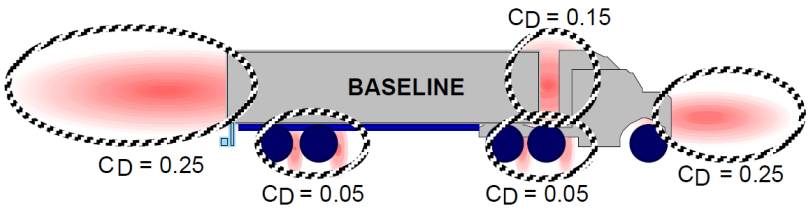

Figure 1.4: Overview major drag contributing regions in crosswind conditions (Wood and Bauer (2003))

1.3 Characteristics of gap flow

As was mentioned in the previous section the gap between the cabin and the trailer of a heavy-duty vehicle is one of the four main regions that significantly contribute to the drag of the vehicle. Some research has already been done on this specific region. Hammache and Browand (2004) investigated the flow structure in the gap of a simplified tractor-trailer model by means of particle image velocimetry (PIV) and force & moment balance measurements. Their wind tunnel experiments were performed at a Reynolds number of approximately 310,000 based on the square root of the cross-sectional area (A). The simplified tractor-trailer model can be imagined as two bluff bodies which are not connected to each other such that there is a gap along the complete cross-sectional area. The authors normalized the gap length (G) by dividing it through the square root of the cross-sectional area and measured the drag force which resulted in Figure 1.5 (Hammache and Browand (2004)).

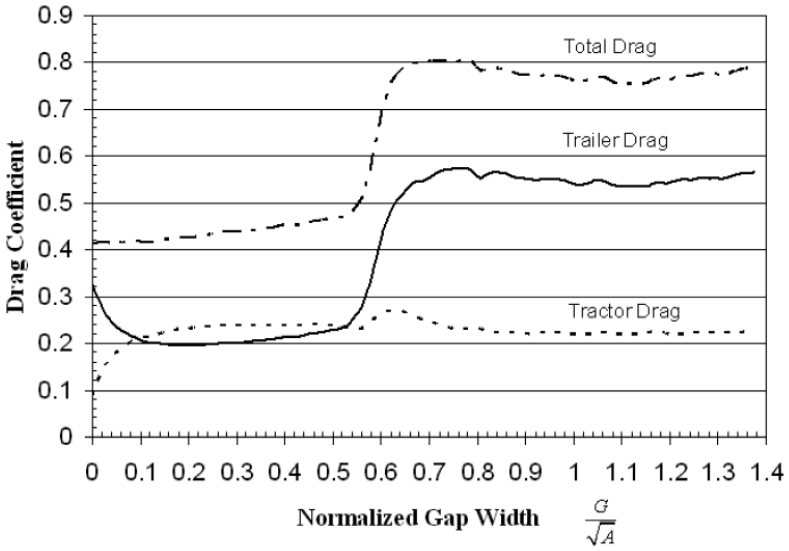

Figure 1.5: Relation of drag coefficient to gap length for a tandem configuration of two bluff bodies (Hammache and Browand (2004))

As can be seen in Figure 1.5 below a normalized gap length of approximately 0.5 $G/\sqrt{A}$ the drag coefficient is significantly lower than when the normalized gap length is larger than 0.5 $G/\sqrt{A}$. There is a drastic increase of the drag coefficient of the trailer between 0.5 and 0.7 $G/\sqrt{A}$ resulting in a significant shift of the total drag coefficient (Hammache and Browand (2004)). Hammache and Browand (2004) state that the drag coefficient of the trailer is lower when the gap length is smaller than 0.5 $G/\sqrt{A}$, because then the trailer is shielded by the presence of the tractor. In other words behind the tractor there is a low pressure region and when the tractor-trailer gap length is increased, the front of the trailer is exposed to high stagnation pressure, increasing the drag of the vehicle.

It is interesting to take a closer look at what exactly happens in the gap. When the gap length is below 0.5 $G/\sqrt{A}$ the flow structure in the gap is steady and a vortex ring can be observed in the gap (Hammache and Browand (2004)). A 2D visualization of the flow obtained by

performing planar PIV measurements shows that the flow is symmetric and contains two counter-rotating vortices which are actually a 2D observation of the vortex ring (Hammache and Browand (2004)). These two counter-rotating vortices were also observed by Storms et al. (2006).

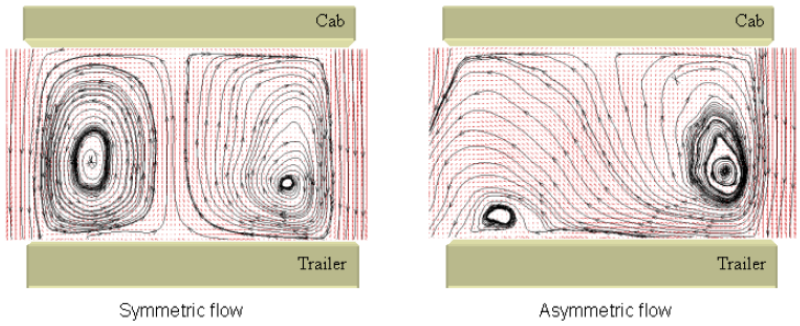

Figure 1.6: Streamlines of the flow inside the tractor-trailer gap at $0.55\ G/\sqrt{A}$ for 0° yaw angle (Hammache and Browand (2004))

When the gap length is increased beyond the normalized gap length of $0.5\ G/\sqrt{A}$, the flow is not longer always symmetric and steady, but periodically the structure of the flow becomes asymmetric (Hammache and Browand (2004)). This is clearly shown in Figure 1.6. The figure on the left shows the symmetric flow structure which can be observed during some periods, the periodically asymmetric flow behavior for the same gap length can be seen on the right figure. During the asymmetric flow periods there is much more crossflow through the gap as was described by Arcas et al. (2004). This significant increase in crossflow is the cause of the drastic increase in drag coefficient as was observed in Figure 1.5 (Arcas et al. (2004)). This periodically behavior results in fluctuating measurements (Hammache and Browand (2004)). As can be seen in Figure 1.7 the measured drag force oscillates significantly at a low frequency when the normalized gap length is larger than $0.5\ G/\sqrt{A}$ (Hammache and Browand (2004)).

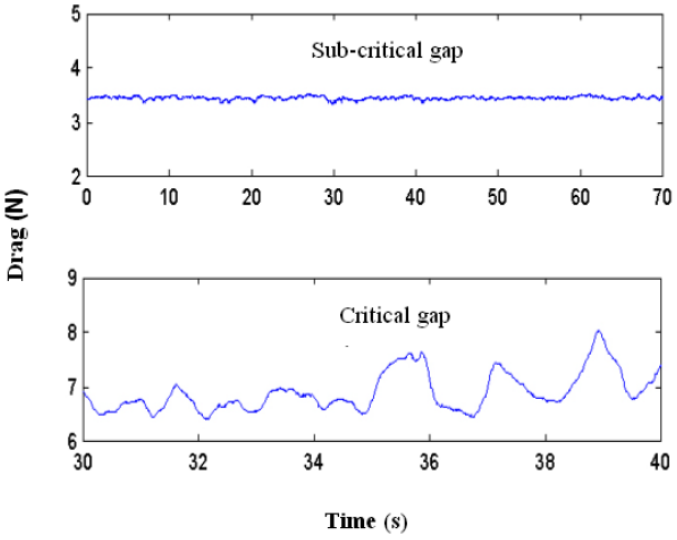

Figure 1.7: Time dependent drag forece measurement (Hammache and Browand (2004))

Hyams et al. (2011) confirm this unsteady behavior of the flow caused by the tractor-trailer gap. However in their Detached Eddy Simulations (DES) they also observe that the tractor-trailer gap causes asymmetric vortex shedding along the sides of the trailer (see Figure 1.8) (Hyams et al. (2011)). It is remarkable that this happens at a relatively small normalized gap length of around 0.32, which is significantly smaller than the critical gap length observed by Hammache and Browand (2004).

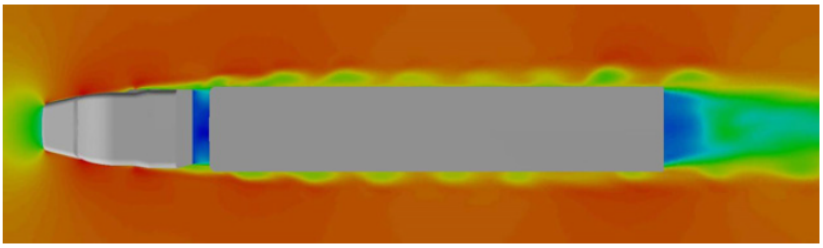

Figure 1.8: Velocity contours at a yaw angle of 0° (Hyams et al. (2011))

1.4 Crosswind conditions

In real-life conditions heavy-duty vehicles experience most of the time crosswind conditions. The exact crosswind condition (wind speed, wind direction, etc.) can vary each time, but it is important to include the possibility of crosswind conditions in the aerodynamic analysis. Crosswind will affect the flow behavior around the vehicle and can result into some specific aerodynamic phenomena like separation and unsteadiness as was mentioned by Choi et al. (2014). For example a separation bubble can develop at the leeward front side of the truck as was shown by Maddox et al. (2004). The wind tunnel experiment on a very simplified heavy-duty vehicle model performed by Hammache and Browand (2004) shows that in general the drag coefficient increases with increasing yaw angle (see Figure 1.9). As can be seen in Figure 1.9 the normalized gap length also influences the drag coefficient, but there is no clear pattern between the gap length and the drag coefficient.

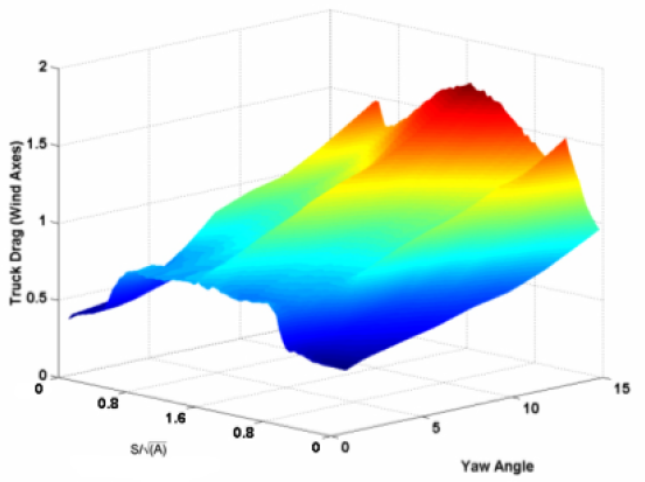

Figure 1.9: Influence of the yaw angle and normalized gap length on the drag, wind tunnel experiment performed on a very simplified heavy-duty vehicle model (Hammache and Browand (2004))

The crosswind has a major impact on the flow structure inside the gap. Wood and Bauer (2003) clearly explain the effect of crosswind on the flow behavior in their study. More flow at a higher velocity enters the gap increasing the pressure at the front of the trailer (Wood and Bauer (2003)). So the shielding effect of the tractor on the trailer has partially disappeared. According to the same article the low pressure zone behind the tractor is reduced due to the presence of the crosswind (Wood and Bauer (2003)). The crosswind flow can also cause separated flow at the leeward side of the trailer (Wood and Bauer (2003)). Figure 1.10 shows a DES simulation of the North-American Generic Conventional Model (GCM) at a yaw angle of 10° at a Reynolds number of $1.15 \cdot 10^6$ based on the trailer width (Hyams et al. (2011)). This figure clearly shows separated flow at the leeward side of the trailer.

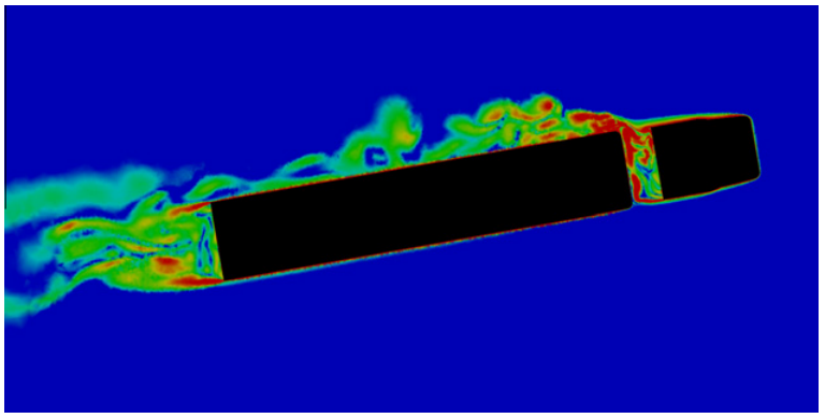

Figure 1.10: DES analysis of the vorticity around the GCM heavy-duty vehicle at 10° yaw angle (Hyams et al. (2011))

Some papers analyzed the flow field inside the gap in more detail by means of PIV. The measurements performed on the North-American GCM by Storms et al. (2004) showed that the

flow field inside the gap becomes asymmetric under crosswind conditions. This experimental study was performed for various Reynolds numbers varying from $0.5 \cdot 10^6$ to $6 \cdot 10^6$ based on the width of the vehicle. As can be seen in Figure 1.11 the asymmetric flow behavior was also experimentally observed by Storms et al. (2006) for the GCM model at a Reynolds number of $4.8 \cdot 10^6$ based on the width of the vehicle.

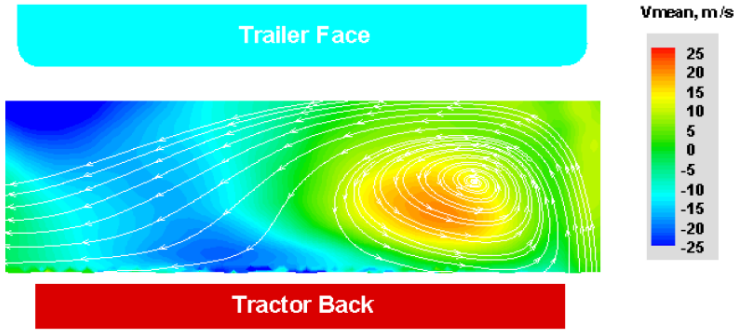

Figure 1.11: PIV measurements on a North-American heavy-duty vehicle model showing an asymmetric flow field inside the gap at 10° yaw angle (Storms et al. (2006))

1.5 Add-on devices

Since the tractor-trailer gap is responsible for a significant part of the drag of a heavy-duty vehicle, multiple researchers investigated if add-on devices can reduce this drag. There are two types of drag reduction devices: active and passive flow control devices. Active flow control devices actively change the flow structure, for example plasma actuators or blowing slots. A few studies investigated how active flow control devices can be applied on heavy-duty vehicles. The research of Ortega et al. (2009) showed that tractor base bleeding reduces the drag coefficient and that it has some good potentials, however there are also many concerns, especially regarding the power and operational requirements of such devices. Therefore active flow control devices will not be further considered in this research.

The first add-on devices that were developed to reduce the tractor-trailer gap drag were cabin side and roof extenders as was explained by Storms et al. (2006). In this paper and in the paper of Heineck et al. (2004) the effect of side extenders on the flow in the gap was analyzed by means of wind tunnel experiments on a GCM, which is a simplified model of a North-American heavy-duty vehicle. In the experimental study performed by Storms et al. (2006) the wind averaged drag coefficient decreased with around 0.06 when the model was equipped with side and roof extenders. Nowadays the cabins of heavy-duty vehicles are standardly equipped with side and roof extenders.

Another often applied drag reduction device is the splitter plate, which can be attached to the trailer frontal surface or the cabin base surface. In the past this add-on device was also frequently analyzed, amongst others by Leuschen and Cooper (2006); Hyams et al. (2011);

Storms et al. (2006). The cross vortex trap device is a patented tractor-trailer gap add-on device designed by Wood (2006). It is constructed out of 6 splitter plates attached parallel to each other on the trailer frontal surface (Wood and Bauer (2003)). According to Wood and Bauer (2003) it can reduce the fuel consumption of a North-American heavy-duty vehicle by 3.5 to 8.3%, but according to Leuschen and Cooper (2006) the obtained drag reduction for a North-American Volvo VN660 is negligibly small.

Furthermore some companies developed commercially available drag reduction devices for the tractor-trailer gap. Two examples are shown in Figure 1.12. The Don-Bur Aeris is an extendable add-on device that automatically fills the tractor-trailer gap when the heavy-duty vehicle is driving at least 49 *mph* (Don-Bur (2015)). The Laydon Composites Ltd. Vortex Stabilizer can be regarded as a splitter plate attached to the trailer frontal surface. However it is unclear if these commercially available add-on devices actually reduce the drag coefficient and by which amount, as no published academy study could be found.

(a) Don-Bur Aeris, an automatically extending gap filler (Don-Bur (2015))

(b) Laydon Composites Ltd. Vortex Stabilizer (Laydon Composites Ltd.)

Figure 1.12: Examples of commercially available tractor-trailer add-on devices

1.6 Design and regulations of heavy-duty vehicles

As could be read in the previous sections, quite some researchers analyzed the aerodynamics of the tractor-trailer gap. However almost all of the research was performed on North-American heavy-duty vehicles and not on European heavy-duty vehicles. This section will describe the differences between the two kind of vehicles and the impact on the aerodynamics.

There is a significant difference between European and North-American heavy-duty vehicles as was explained by Hjelm and Bergqvist (2009). The most important differences are the

velocity and geometry and they are both due to difference in legislation. European heavy-duty vehicles are in average limited to a maximum velocity of around 85 km/h which is lower than in the USA. In the USA the reference velocity for heavy-duty vehicles driving on the highway can be considered to be around 65 mph, which is approximately 105 km/h. This can have a small impact on the aerodynamics as it slightly affects the Reynolds number. The Reynolds number of the North-American and the European heavy-duty vehicles is behind the transitional regime, so the impact will probably be small (Hjelm and Bergqvist (2009)). In the same article of Hjelm and Bergqvist (2009) it was explained that in Europe the maximum length of a heavy-duty vehicle is defined by the total length of the complete vehicle, but in the USA the length is measured by the length of the trailer as can be seen in Figure 1.13. This difference in legislation leads to differences in the design of the heavy-duty vehicles. Because the total length is limited European heavy-duty vehicles commonly have their cab on top of their engine while North-American heavy-duty vehicles have a conventional design with a hood (Hjelm and Bergqvist (2009)). Another consequence of this limited total length and because haulers want to transport as much cargo as possible is that the gap length is minimized for European heavy-duty vehicles (Hjelm and Bergqvist (2009)). In North-America the gap between the cabin and the trailer can be 3.5 times bigger compared to European heavy-duty vehicles (Hjelm and Bergqvist (2009)). As was explained earlier the length of the gap has a very significant effect on the flow field inside the gap and on the drag coefficient of the entire vehicle.

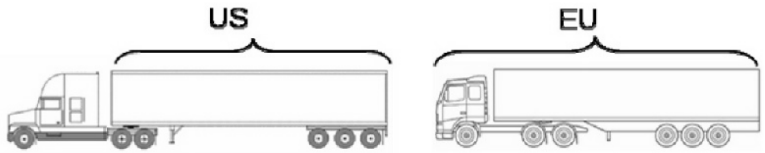

Figure 1.13: Difference in legislation and resulting geometry of heavy-duty vehicles in Europe and the US (Hjelm and Bergqvist (2009))

One can wonder why there is a gap between the tractor-trailer and why they do not fully close the gap. The main reason is that it would decrease the turn radius of the heavy-duty vehicle. According to Welfers et al. (2011) the maximum turning radius is set by the European Union to be 12.5 m. Furthermore the tractor is designed such that it can carry trailers from multiple different manufacturers. The back of the tractor should also be accessible (ETSU and MIRA (2001)). So due to operational and legislative requirements there should be at least a small gap between the tractor and the trailer.

1.7 Present study

As could be read in the previous sections, there is big interest in reducing the aerodynamic drag caused by the tractor-trailer gap. Reducing this drag will make the heavy-duty vehicle more efficient leading to less fuel costs and less greenhouse gas emissions. As was pointed out in section 1.3 quite some research has been done on the fundamentals of the flow structure between two bluff bodies. In section 1.5 it was shown that a few researchers performed tests

to look for the most suitable add-on device to reduce the tractor-trailer aerodynamic drag. However all these investigations were considering North-American heavy-duty vehicles, which differ significantly from European heavy-duty vehicles. Therefore the question of how to reduce the tractor-trailer gap drag of European heavy-duty vehicles still remains unanswered.

Although there is a large interest in optimizing the tractor-trailer gap aerodynamics, there has not been a thorough analysis and comparison of ways to reduce this drag focusing on European heavy-duty vehicles. Therefore the goal of this master thesis is to identify the best type of passive flow control drag reduction device for the tractor-trailer gap of European heavy-duty vehicles by measuring the drag coefficient at various yaw angles. This main goal leads to the following main question.

"Which type of passive flow control drag reduction device for the tractor-trailer gap results in the largest wind averaged drag coefficient reduction for European heavy-duty vehicles?"

Two analysis methods will be applied in order to be able to answer this main question: a numerical and an experimental analysis. The next chapter describes the complete numerical analysis, including the set-up and the results. The wind tunnel test set-up and the experimental results will be discussed in chapter 4. Afterwards the results of both methods will be discussed and compared with each other and all the possible differences will be explained. This discussion of the results can be found in chapter 5. Finally the conclusions and the recommendations will be described in chapter 6.

Chapter 2

Project Approach

It is now clear that there is a large interest in reducing the aerodynamic drag caused by the tractor-trailer gap. Reducing this drag will lead to less greenhouse gas emissions and less operational costs for the haulers. As was stated in the previous chapter the goal of this study is therefore to analyze the aerodynamics of passive drag reduction devices for the tractor-trailer gap of European heavy-duty vehicles and to see the effect on the drag coefficient of the vehicle.

This chapter will describe how this project is approached and which steps are taken before the actual analysis methods will be performed. Firstly a proper model of an European heavy-duty vehicle has to be designed. This is discussed in section 2.1. Afterwards the passive drag reduction devices will be selected and designed, which is described in section 2.2. An overview of all the test configurations is given in section 2.3. Finally some important parameters will be explained in section 2.4.

2.1 Design of the test model

2.1.1 The S-E model

It is of crucial importance to have a well-designed heavy-duty vehicle model on which the analysis can be performed. The model should accurately represent the shape of heavy-duty vehicles which are driving nowadays on the road. However the test model should not be too complex as this complicates the production of the wind tunnel model and the meshing for the numerical analysis. Furthermore a simple design of the test model is beneficial for this analysis as then only a limited amount of factors can affect the results. A simple design focuses more on the effects of the tractor-trailer gap on the flow, while other effects on the flow behavior are minimized. The disadvantage of a simple design of the test model is that it is less representative for actual heavy-duty vehicles driving on the road. Omitting side mirrors,

mud flaps, the grill, etc. in the design of the test model will influence the obtained results. As this study mainly focuses on the trends of different gap designs on the drag coefficient of the vehicle and on the flow field inside the gap, it was decided to use a simple design for the test model.

Van Raemdonck (2012) developed a generic model of a modern European tractor-trailer combination, the Generalized European Transport System (GETS), which is shown in 2.1(a). This model has been frequently used in past research, amongst others by Gheyssens (2016); van Leeuwen (2009); Van Ginderdeuren (2010), but cannot be used in this study as it does not have a tractor-trailer gap. Therefore it was decided to design a new simple model which represents a modern European heavy-duty vehicle, but which contains more details than the GETS model.

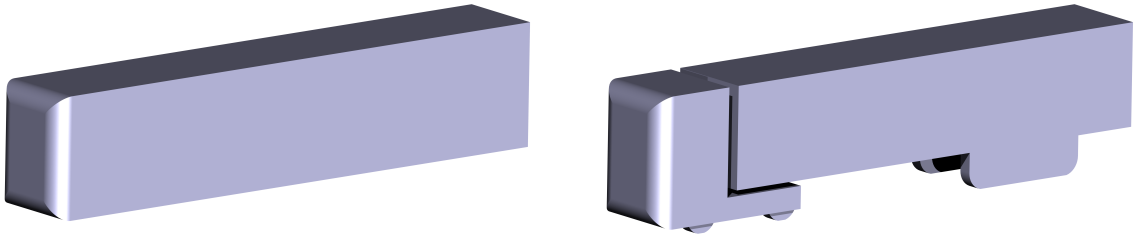

(a) The GETS model

(b) The S-E model

Figure 2.1: Two different European test models

A few heavy-duty vehicles that were driving on the road in Europe were photographed and their dimensions were measured. All these measurements were combined and an average value was computed for each dimension. These measurements were combined with the design of the GETS model to create the new generic heavy-duty vehicle model, called the S-E model. The S in the name stands for small gap length and the E indicates that there are extenders (both side and roof extenders) attached to the cabin. A rendering of the S-E model is shown in 2.1(b). The new design has the same outer dimensions (16.5 m long, 2.6 m wide and 4 m high) as the GETS model, as these were based on the maximum allowable dimensions for tractor-trailer combinations in Europe (Van Raemdonck and Van Tooren (2008)). Also the front edges of the S-E model are based on the GETS model as the front edges of the GETS model were designed in such a way that front edge flow separation does not occur at a yaw angle of 0° (Van Raemdonck and Van Tooren (2008)). The S-E model has side and roof extenders attached to the cabin as this is very common for modern European heavy-duty vehicles. In several older research studies these extenders were considered as additional add-on devices and were not included in the baseline model. However nowadays heavy-duty vehicles are standardly equipped with side and roof extenders, therefore they were included in the baseline model.

This study contains an experimental analysis performed in a wind tunnel. Due to practical limitations of the test section a 1:8 scaled model had to be built. A complete overview of the model and its dimensions can be seen in section A.1.

2.1.2 The baseline models

This study focuses on the effect of the tractor-trailer gap on the drag coefficient of modern heavy-duty vehicles. To properly analyze the effect of the gap on the drag coefficient, different configurations were developed in which the dimensions of the tractor-trailer gap were modified. These other configurations, called baseline configurations or baseline models, do not contain any additional add-on devices, but only have a different gap geometry.

The Large-Extenders (L-E) baseline model is exactly the same model as the S-E baseline model, but it has a larger gap length. In the S-E baseline model the tractor-trailer gap length is equal to 0.652 m, while the gap length equals 2.148 m for the L-E baseline model. The gap length of the L-E model is based on the study of Hjelm and Bergqvist (2009). According to this study the gap length of North-American heavy-duty vehicles can be 3.5 times larger than the gap length of European heavy-duty vehicles. Another baseline configuration is the Medium-Extenders (M-E) model, which is identical to the S-E and L-E baseline model, but with a gap length of 1.508 m. The fourth baseline model is the Small-No Extenders (S-NE) model, which is the same as the S-E baseline model but without the side and roof extenders. This baseline model was included in the analysis as it can show the effect of the side and roof extenders on the flow dynamics. Finally the last baseline configuration is the No Gap (NG) model, where there is no tractor-trailer gap. An overview of the L-E, M-E, S-NE and NG baseline models can be seen in Figure 2.2.

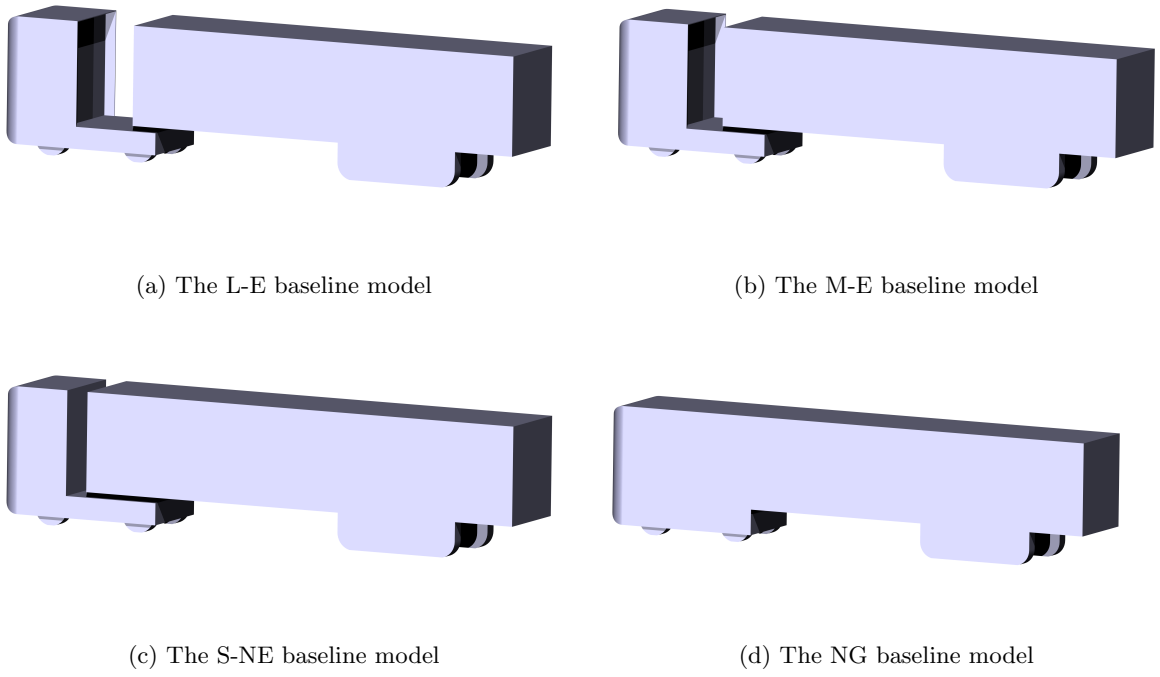

(a) The L-E baseline model

(b) The M-E baseline model

(c) The S-NE baseline model

(d) The NG baseline model

Figure 2.2: The different baseline models (excluding the S-E baseline model)

In the past several studies were performed where the gap length was increased by moving

the trailer downstream of the tractor, amongst others by Hammache and Browand (2004); Buijs (2010); Arcas et al. (2004)). In this way the length of the trailer and the length of the cabin remains the same, but the total length of the vehicle is increased when the gap length is increased. In this research study the length of the gap was varied by changing the length of the trailer. So the total length of all baseline models is the same, but the length of the trailer varies between the baseline models. For example the L-E baseline model has the same total length as the S-E baseline model, but the trailer length is significantly shorter compared to the S-E trailer. So in fact the L-E and M-E baseline models should be considered as heavy-duty vehicles with shorter trailers, an example is shown in Figure 2.3. There are two main reasons why increasing the gap length was done differently than in literature. As was explained before in Europe the maximum length of the total vehicle is limited by law. By keeping the total length of the baseline models constant, they are all within the legal limitations. Secondly keeping the total length of the complete vehicle the same was easier for the wind tunnel campaign, especially because moving the trailer can easily cause misalignments.

Figure 2.3: An example of a real M-E/L-E baseline model on the road (Klicktel (2016))

As was described before the gap length can be normalized with respect to the square root of the cross-sectional area. In this study the cross-sectional area is based on the cross-sectional area of the cabin. Table 2.1 gives an overview of the baseline models with their actual gap length in meters, their normalized gap length and whether or not they are equipped with side and roof extenders.

Table 2.1: Overview of the gap geometry of the baseline models

Geometrical parameter	**S-E**	**S-NE**	**M-E**	**L-E**	**NG**
Non-normalized gap length [m]	0.652	0.652	1.508	2.148	0
Normalized gap length [-]	0.209	0.209	0.483	0.688	0
Side and roof extenders	Yes	No	Yes	Yes	-

2.2 Design of the add-on devices

In this study multiple different conceptual add-on devices will be tested on the different baseline models. In previous studies a few add-on devices were developed, but they were not

tested together on one and the same model. Besides these already existing add-on devices, a few new conceptual add-on devices were created. The design and the idea behind these add-on devices will be described in this section.

All the tested add-on devices are conceptual ideas. This means that they have a very simple design and that the design is not optimized. No parametric study was performed on the exact geometry and dimensions of the add-ons, but this can be an interesting topic for future research. To keep all the add-on devices comparable to each other they all have the same length in the longitudinal axis, namely 0.050 m in the 1:8 scaled model, which is equal to 0.4 m in 1:1 scale.

The list of add-on devices can be split up in two groups: the practically feasible add-ons and the practically infeasible add-on devices. The first group contains all the add-on devices that are practically feasible and do not limit the maneuverability of the heavy-duty vehicle. The turning radius is not affected by the add-on devices. The second group includes add-on devices that are currently practically unfeasible or influence the maneuverability of the vehicle. Although these add-on devices are practically unfeasible, theoretically they can be interesting concepts. An overview of all the add-on devices attached to different baseline models is shown in Figure 2.5.

2.2.1 Practically feasible add-on devices

Splitter Plate (SP)

The splitter plate (SP) is a vertical flat plate attached to the trailer in the middle of the width of the trailer. The splitter plate has been frequently tested in the past on North-American heavy-duty vehicles, amongst others by Hyams et al. (2011); Leuschen and Cooper (2006). These studies observed high drag reductions with the splitter plate in crosswind conditions. The idea behind the concept is that it blocks the air flowing from the windward to the leeward side inside the tractor-trailer gap.

Cabin Splitter Plate (CSP)

One can also attach the splitter plate to the base surface of the cabin as was done by Storms et al. (2006) on a North-American heavy-duty vehicle. According to this study the cabin splitter plate (CSP) also reduces the drag coefficient, especially at larger yaw angles, by reducing the crossflow in the gap.

Cross Vortex Trap Device (CVTD)

The cross vortex trap device was already explained in section 1.5. In summary it is a combination of 6 splitter plates attached next to each other on the trailer frontal surface (Wood (2006)). When a CVTD is attached to the trailer small circulations should develop in between the splitter plates, which should decrease the pressure on the trailer frontal surface and

therefore reduce the drag coefficient (Wood and Bauer (2003)).

Rounded Edges (RE)

Buijs (2010) tested the rounded edges (RE) add-on device on a truck-trailer combination. The RE add-on device is an additional part which has smoothly rounded edges of a radius of 0.4 m and that it is as long as the other add-on devices in the longitudinal axis. The goal of this add-on device is to avoid separation at the sharp corners of the trailer by making them round. The add-on device also decreases the gap length as the tractor-trailer gap is partially filled with the add-on device. It is important to note that the RE add-on device applied in this study only has rounded edges on the vertical edges of the trailer and not on the horizontal edges, while in the work of Buijs (2010) all the four edges were rounded. According to the work of Buijs (2010) the wind averaged drag coefficient reduction for a truck-trailer combination is only 0.4%.

Vertical Cylinders (VC)

The vertical cylinders (VC) are two vertical half cylinders attached closely to the vertical edges of the trailer frontal surface. They have the same goal as the RE add-on device, namely avoiding separation at the edges of the trailers by making the edges round. The radius of the half cylinders is exactly the same as the radius of the rounded edges of the RE add-on device. This type of add-on device was also tested by Buijs (2010) for a truck-trailer combination and he determined a wind averaged drag coefficient reduction of 1.4%.

Cooling Unit (CO)

Often trailers are equipped with a cooling unit to keep the temperature inside the trailer at a low level. As these cooling units are mostly placed on the trailer frontal surface, i.e. in the tractor-trailer gap, the cooling unit is also included in this study as an add-on device. The cooling unit applied in this research is roughly based on the Carrier Transicold Vector series (Figure 2.4) and again the length of the add-on is equal to the length of the other add-on devices (Carrier Transicold).

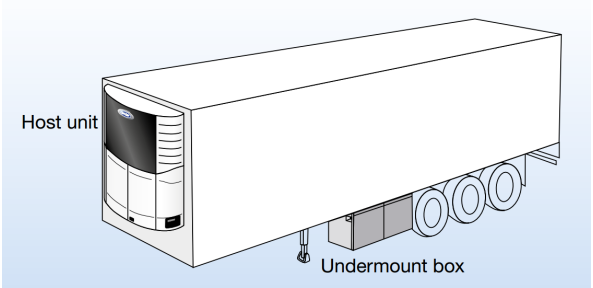

Figure 2.4: An example of a trailer equipped with a Carrier Transicold Vector cooling unit (Carrier Transicold)

Large Side Extenders (LSE)

As was explained in subsection 2.1.2 the S-NE baseline model was created in order to be able to analyze the effect of side and roof extenders on the drag coefficient. However now only two cases can be compared: with and without side and roof extenders. To be able to analyze the effect of solely the side extenders, the large side extenders (LSE) add-on device was developed. This add-on device will only be attached to the S-NE baseline model such that a new configuration can be created with only side extenders and no roof extenders. The add-on device is called large side extenders because the side extenders are equally long as the other add-on devices (0.4 m), which is a bit longer than the standard side extenders which were used on the S-E, M-E and L-E baseline models (0.328 m).

2.2.2 Practically infeasible add-on devices

Horizontal Cylinders (HC)

The horizontal cylinders (HC) add-on device is very similar to the vertical cylinders add-on device, the half cylinders are now placed horizontally instead of vertically. By placing the half cylinders horizontally, the maneuverability is very much affected. In fact when the HC add-on device is attached to the trailer frontal surface of the S-E or the S-NE baseline model, the heavy-duty vehicle cannot turn properly.

Sides Covered (SC)

Another practically unfeasible concept is extending the side surfaces of the trailer in upstream direction until the base of the cabin. This might sound like the NG baseline model, however with the SC concept the tractor-trailer gap is still open at the top and at the small horizontal gap between the tractor and the trailer.

Sides Bottom Covered (SBC)

This concept is a small adaption of the SC concept where also the small horizontal gap between the tractor and the trailer is closed. In other words it the same model as the NG baseline model but then without the top surface of the gap closed.

Sides and Top Covered (STC)

In this add-on device the side surfaces of the trailer are extended in upstream direction until the base of the cabin and also the top of the tractor-trailer gap is closed. So the complete gap is covered with exception of the small horizontal gap between the tractor and the trailer.

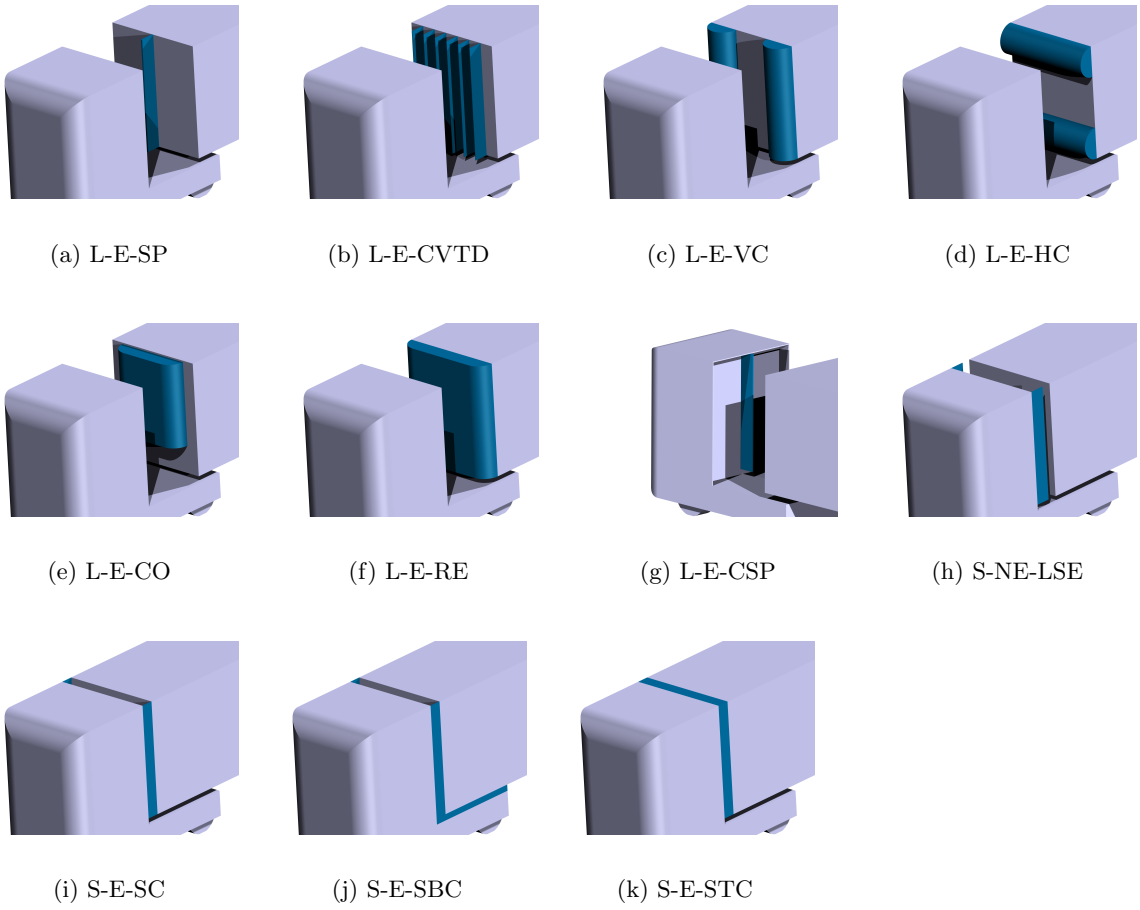

(a) L-E-SP (b) L-E-CVTD (c) L-E-VC (d) L-E-HC

(e) L-E-CO (f) L-E-RE (g) L-E-CSP (h) S-NE-LSE

(i) S-E-SC (j) S-E-SBC (k) S-E-STC

Figure 2.5: An overview of the tested add-on devices on different baseline models

2.3 Overview of the tested configurations

An overview of all the tested configurations, both numerically and experimentally, is shown in Table 2.2. As can be seen in the table, not every add-on device was tested on each baseline model. Due to time constraints during the wind tunnel campaign and during the numerical analysis, the maximum number of configurations was limited. Furthermore for some add-on devices it was not useful or not possible to test them on certain baseline models. For example the LSE add-on device was only tested on the S-NE baseline model, as the other baseline models already have side extenders. Adding the STC add-on device on the L-E, M-E or S-NE baseline model would be exactly the same as adding this add-on device to the S-E baseline model, therefore it was sufficient to only test it on the S-E baseline model.

Table 2.2: Overview test cases

Add-on device	Baseline model				
	NG	S-E	S-NE	M-E	L-E
No add-on	CFD/EXP	CFD/EXP	CFD/EXP	CFD/EXP	CFD/EXP
SP	-	CFD/EXP	CFD/EXP	EXP	CFD/EXP
CSP	-	-	EXP	-	-
CVTD	-	-	EXP	-	EXP
RE	-	CFD/EXP	EXP	EXP	CFD/EXP
VC	-	EXP	EXP	-	-
CO	-	EXP	EXP	-	EXP
LSE	-	-	EXP	-	-
HC	-	-	EXP	-	EXP
SC	-	EXP	-	-	-
SBC	-	EXP	-	-	-
STC	-	EXP	-	-	-

All these configurations were tested under various yaw angles in order to determine the effect of the yaw angle on the flow behavior. As it is advised by SAE (2012) to test at yaw angles with intervals of 3°, it was decided to test at 0°, 3°, 6°, 9° and 12°. The numerical simulations of the configurations equipped with add-on devices were only performed till a yaw angle of 9° due to time constraints.

2.4 Definition of parameters

In this study the aerodynamic drag coefficient will be used as the main parameter to analyze the aerodynamic performance of the different configurations of the tractor-trailer gap. In the case of road vehicles the drag force is often defined in the longitudinal direction of the vehicle. Therefore in this study the drag coefficient C_T is measured in the longitudinal direction, i.e. the driving direction of the vehicle. To analyze small differences in drag coefficient, the dimensionless parameter drag count is often used. The drag count equals 0.1% of the drag coefficient.

As was explained in subsection 2.1.2 the different configurations can be categorized according to their (normalized) tractor-trailer gap length. However as the S-NE baseline model does not have side and roof extenders in contrast to the other baseline configurations, another parameter was introduced to point out the difference when no side and roof extenders are present. This parameter is called the effective gap length and is defined as the length from the trailer frontal surface to most downstream end of the extenders or to the base of the cabin if there are no extenders present.

Chapter 3

Numerical Analysis

Two analysis methods are applied in this study to analyze the aerodynamics of drag reduction devices for the tractor-trailer gap: a numerical and an experimental analysis. The firstly mentioned method is a Computional Fluid Dynamics method, which will be discussed in this chapter. The goal of this analysis is to obtain a detailed analysis of the flow field inside the tractor-trailer gap for a various amount of cases and to study the effectiveness of a few add-on devices. First the complete set-up of the numerical analysis will be described in section 3.1, afterwards all the obtained results will be analyzed in section 3.2.

3.1 Set-up of the numerical analysis

3.1.1 Numerical method and turbulence modeling

One of the methods that is used in this study to analyze the flow field around heavy-duty vehicles is Computational Fluid Dynamics (CFD). CFD is a numerical method that makes use of mathematical equations and computational power to simulate the flow around objects. Most CFD methods are based on the Navier-Stokes equations which consist out of the continuity and momentum equations, respectively Equation 3.1 and Equation 3.2. However the CFD code can also make use of different equations than the Navier-Stokes equations, for example the Lattice Boltzmann Method (LBM).

Continuity equation (Anderson (2011)):

$$\frac{\partial \rho}{\partial t} + \nabla \cdot (\rho \boldsymbol{V}) = 0 \tag{3.1}$$

Momentum equation (Anderson (2011)):

$$\begin{aligned}
\frac{\partial(\rho u)}{\partial t} + \nabla \cdot (\rho u \boldsymbol{V}) &= -\frac{\partial p}{\partial x} + \rho f_x + (F_x)_{viscous} \\
\frac{\partial(\rho v)}{\partial t} + \nabla \cdot (\rho v \boldsymbol{V}) &= -\frac{\partial p}{\partial y} + \rho f_y + (F_y)_{viscous} \\
\frac{\partial(\rho w)}{\partial t} + \nabla \cdot (\rho w \boldsymbol{V}) &= -\frac{\partial p}{\partial z} + \rho f_z + (F_z)_{viscous}
\end{aligned} \tag{3.2}$$

Completely solving the entire Navier-Stokes equations is called Direct Numerical Simulation (DNS). DNS solves the equations on all turbulent length scales and therefore it needs an extremely small grid and very small time steps. For most flow problems, including the research on automotive vehicles, this leads to unfeasible computational requirements as was also stated by Elofsson (2014).

A way to reduce the computational requirements is by only solving the large scale eddies, which is called Large Eddy Simulation (LES). This method was already successfully applied on automotive vehicles by for example Das et al. (2013) and Krajnovic and Davidson (2002), but the computational requirements are too high for an extensive comparative study. Reynolds-Averaged Navier-Stokes (RANS) splits the velocity components into a time-averaged mean value and a fluctuating value leading to significantly lower computational requirements. Detached Eddy Simulation (DES) combines both LES and RANS, depending on the location in the domain it applies LES or RANS. In the past RANS was often applied with the software package Fluent in automotive studies at the TU Delft comparing multiple different configurations, amongst others, Gheyssens (2016); Van Raemdonck (2012); Buijs (2010); Van Ginderdeuren (2010); van Leeuwen (2009)).

Above discussed methods are all based on the Navier-Stokes equations, but CFD can also make use of other principles. Recently more and more studies apply the Lattice Boltzmann Method to analyze the aerodynamics of road vehicles. LBM is based on the Boltzmann equation and considers the aerodynamic flow as microscopic particles in order to determine the macroscopic characteristics. Many studies, amongst others Horrigan et al. (2007); Islam et al. (2008); Horrigan et al. (2008); Heinecke et al. (2010), applied LBM to analyze the aerodynamics of heavy-duty vehicles, the majority of them used the commercial software package PowerFLOW (Exa Corporation). However no license for PowerFLOW was available for this research and open-source software packages as OpenLB (Krause) and Palabos (Palabos) were considered as not reliable enough, since no studies were found that analyzed the aerodynamics of automotive vehicles with these open-source software packages.

To summarize RANS is the best suitable method for this study. In the past many studies about heavy-duty vehicle aerodynamics applied RANS to simulate the flow field. It is the simplest method that is expected to be able to predict the aerodynamic trends. Multiple CFD software package are capable of performing RANS simulations. For this study the software package Fluent was used due to the availability of licenses and the past experience with the package at the department.

To be able to solve the RANS equations, one needs to introduce a closure model. Several clo-

sure models are available that can be applied for simulating heavy-duty vehicle aerodynamics. The research of Malviya et al. (2009) and the study performed by Pointer et al. (2009) stated that the $\kappa - \omega$ SST closure model is the best closure model regarding simulations of heavy-duty vehicles. In the study of Pointer et al. (2009) the error in predicted drag coefficient with the $\kappa - \omega$ SST closure model was only 0.8%. Additionally Veluri et al. (2009) proved that RANS $\kappa - \omega$ SST can accurately predict the drag force on a simplified heavy-duty vehicle.

3.1.2 Computational domain and boundary conditions

Around the heavy-duty vehicle model one should design a complete computational domain in which the flow is simulated. In this computational domain the whole volume is discretized in smaller cells in which the flow parameters are calculated with the use of the Navier-Stokes equations. A proper design of the computational domain is of critical importance to obtain the correct flow dynamics. The computational domain is based on the recommendations of SAE (2013). The total length of the domain is 11 times the length of the heavy-duty vehicle: 3 times the length of the model in front of the model and 7 times downstream of the model. The width of the domain is 13 times the width of the model, which is placed in the middle of both sides. Finally the height of the domain is 6 times the height of the model. The relative dimensions of the domain are shown in Table 3.1 where L_m, W_m and H_m stand for respectively the length, the width and the height of the model. Furthermore to achieve a high similarity with the wind tunnel experiment, a ground plate was created in the domain. This ground plate has approximately the same dimensions as the ground plate that was used during the wind tunnel experiment. The dimensions of the ground plate used in the experimental campaign can be found in section A.3. An overview of the domain and the boundaries can be seen in Figure 3.1.

Table 3.1: Relative dimensions of the domain and the density boxes

Volume	Relative length	Relative width	Relative height
Domain	$11 \cdot L_m$	$13 \cdot W_m$	$6 \cdot H_m$
Inner Box	$3 \cdot L_m$	$3 \cdot W_m$	$1.5 \cdot H_m$
Wake Box	$1.8 \cdot L_m$	$2.5 \cdot W_m$	$1.35 \cdot H_m$
Truck Box	$1.1 \cdot L_m$	$1.5 \cdot W_m$	$1.2 \cdot H_m$

The domain contains 3 density boxes placed around the heavy-duty vehicle model. The goal of these density boxes is to refine the mesh at specific locations, while still keeping the mesh coarse in the far field. By refining the mesh around the model one improves the probability of simulating all the correct flow phenomena like separation and reattachment. The finest density box is placed closely to the model and has as main goal to refine the mesh in the tractor-trailer gap and the underbody of the model. The second density box, called "Wake Box", is created to ensure a fine mesh in the wake of the model. Finally the third density box, "Inner Box", contains the large surroundings around the model. The relative dimensions of the domain and the density boxes can be found in Table 3.1. The degree of refinement of the density boxes is studied in subsection 3.1.5.

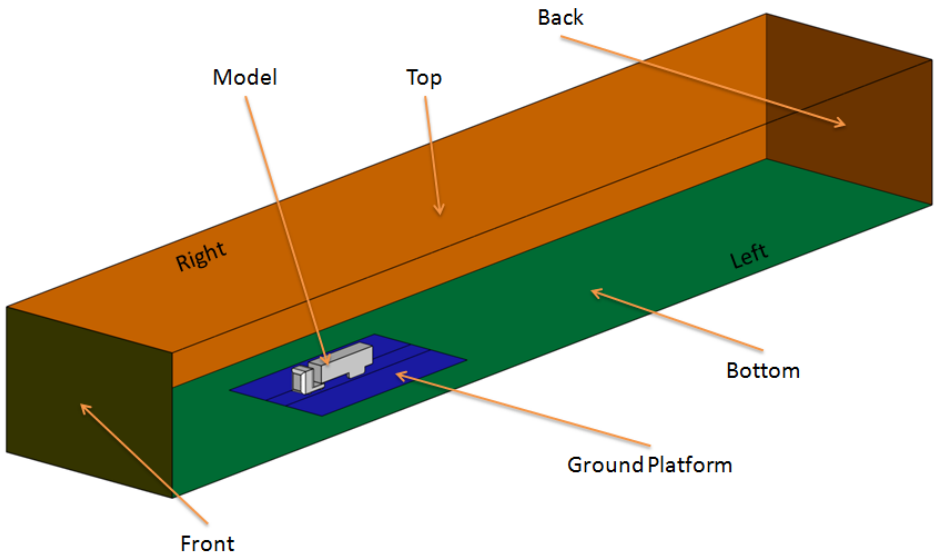

Figure 3.1: Overview of the domain and the boundaries

The domain is used for all configurations, including crosswinds. Depending on whether crosswind or 0° yaw angle was simulated, the inlet and outlet boundary conditions were changed. When 0° yaw angle was simulated, the left and right side surface of the domain were simulated as symmetry planes. To simulate crosswind conditions, the left surface of the domain was changed into an inlet and the right surface of the domain was defined as an outlet boundary. Regarding the boundary conditions themselves, the advise provided by SAE (2013) was followed. The inlet was defined as a velocity-inlet, while the outlet was defined as a zero-gradient pressure-outlet. The top of the domain and in case of 0° yaw angle the sides of the domain were assigned as symmetry boundary conditions. The bottom of the domain, except for the ground plate, was defined as moving wall. An overview is given in Table 3.2.

Table 3.2: Overview of the applied boundary conditions

Surface	**0° yaw angle Boundary Condition**	**Crosswind Boundary Condition**
Front	Velocity-inlet	Velocity-inlet
Back	Pressure-outlet	Pressure-outlet
Left	Symmetry	Velocity-inlet
Right	Symmetry	Pressure-outlet
Top	Symmetry	Symmetry
Bottom	Moving wall	Moving wall
Ground plate	Non-moving wall	Non-moving wall
Model	Non-moving wall	Non-moving wall

3.1.3 Wall treatment and boundary layer

When simulating flow around automotive vehicles, it is important to take a closer look at the flow conditions near the wall. The region perpendicular to a wall can be split up in three distinctive layers. The outer layer is the furthest away from the wall and here the flow properties are not influenced by viscous effects of the wall. The inner layer is the closest to the wall and is mainly dependent on the viscous effects and not on the free stream flow conditions. This layer consists out of the viscous sublayer and the buffer layer. Finally the overlap layer is an overlap region between the inner and outer layer. In this region one can apply the logarithmic law.

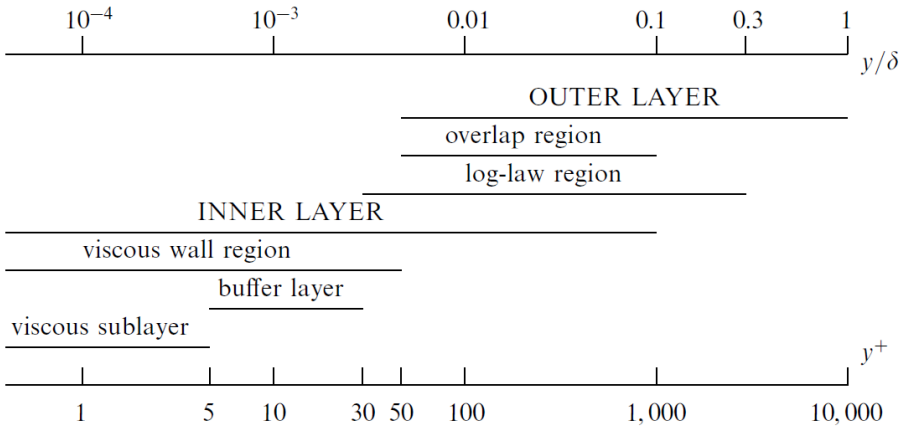

Figure 3.2: The various layers of the flow close to a wall categorized by y^+ (Pope (2000))

As can be seen in Figure 3.2 all the layers and sublayers can be categorized by their location which is done by means of the the non-dimensional wall distance y^+. The non-dimensional wall distance depends on the height y, the viscosity ν and the friction velocity u^*, as can be seen in Equation 3.3 (Pope (2000)). When meshing, the reference height y is taken as half the height of the first cell $y_{1/2}$.

$$y^+ = \frac{u^* \cdot y_{1/2}}{\nu} \tag{3.3}$$

There are two ways to handle the flow close to a wall, namely the near wall model and the wall functions. The first one solves the complete flow field close the wall, leading to high requirements regarding mesh size, because y^+ should then be between 1 and 5 (SAE (2013)). The wall function approach does not solve the complete boundary layer, but models the flow properties by means of semi-empirical functions (Fluent Inc. (2006)). When wall functions are used, the requirements on y^+ are not that strict: y^+ should be smaller than 300 and preferably between 30 and 100, according to SAE (2013). In Fluent the enhanced wall treatment option is automatically selected when one choses the $\kappa - \omega$ SST turbulence model. The enhanced wall treatment is a method using the wall function and combining it with the near wall model in case of low y^+ values (Fluent Inc. (2006)).

Now that the required y^+ value is defined, the height of the first cell can be determined. Equation 3.3 can be rewritten as follows.

$$\begin{aligned} y_{1/2} &= \frac{\cdot y^+ \cdot \nu}{u^*} \\ &= \frac{y^+ \cdot \mu}{\sqrt{\tau \rho}} \end{aligned} \tag{3.4}$$

For the wall shear stress τ and the friction coefficient C_f respectively Equation 3.5 and Equation 3.6 can be used. The latter one is an approximation of the friction coefficient for a turbulent boundary layer on a flat plate (White (2006)).

$$\tau = \frac{1}{2}\rho V^2 C_f \tag{3.5}$$

$$C_f \approx \frac{0.455}{ln^2(0.06Re_x)} \tag{3.6}$$

With these formulas the height of the first cell can be determined. The height of the first cell on the cabin has to be around 2 mm, with exception of the frontal curved surfaces where the cell height has to be around 0.9 mm. Around the trailer the height of the cell was set on 1.8 mm.

After the first simulations were performed, it was checked if the y^+ values on the surface of the S-E baseline model were indeed within the acceptable range. Figure 3.3 shows the y^+ values for the S-E baseline configuration at 0° yaw angle. All the y^+ values on the surface are below 300 and most parts of the surface are between 30 and 100 which is the ideal range according to SAE (2013).

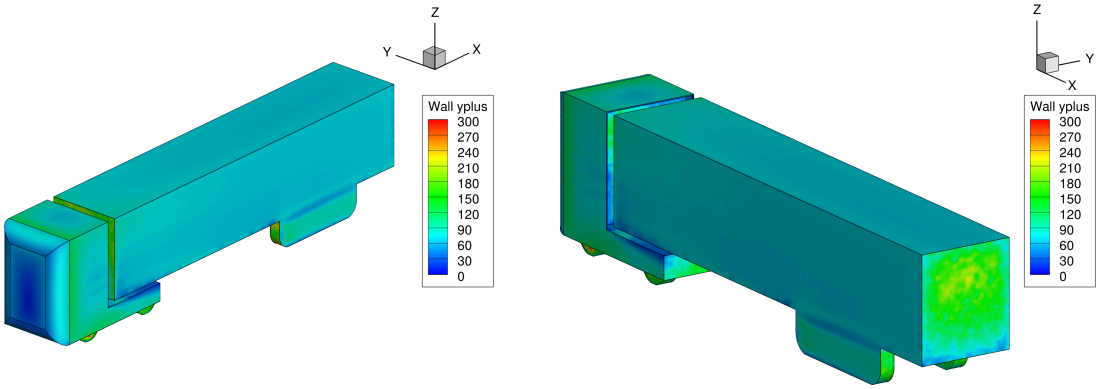

(a) Front side of the S-E model

(b) Back side of the S-E model

Figure 3.3: y^+ values on the surface of the S-E baseline model

It was decided to use a prism layer around the the frontal, side and top surfaces of the cabin and on the side and top surfaces of the trailer and also on most of the ground platform. On the other surfaces no prism layer was created as this decreased the quality of the mesh and lead to several errors. The prism layer helps to accurately capture the boundary layer, because when the cells are aligned with the flow direction one reduces the numerical diffusion. The prism layer height was set equal to the height of the boundary layer, which was approximated by the height of a turbulent boundary layer on a flat plate (see Equation 3.7 (White (2006))).

$$Re_\delta \approx 0.16 \cdot Re_x^{6/7} \tag{3.7}$$

Figure 3.4 shows a slice of the total pressure at the middle of the heavy-duty vehicle height. The figure contains a close-up of the boundary layer in which a slice of the mesh is also included. From the figure it is clearly visible that the boundary layer is captured with the prism layer.

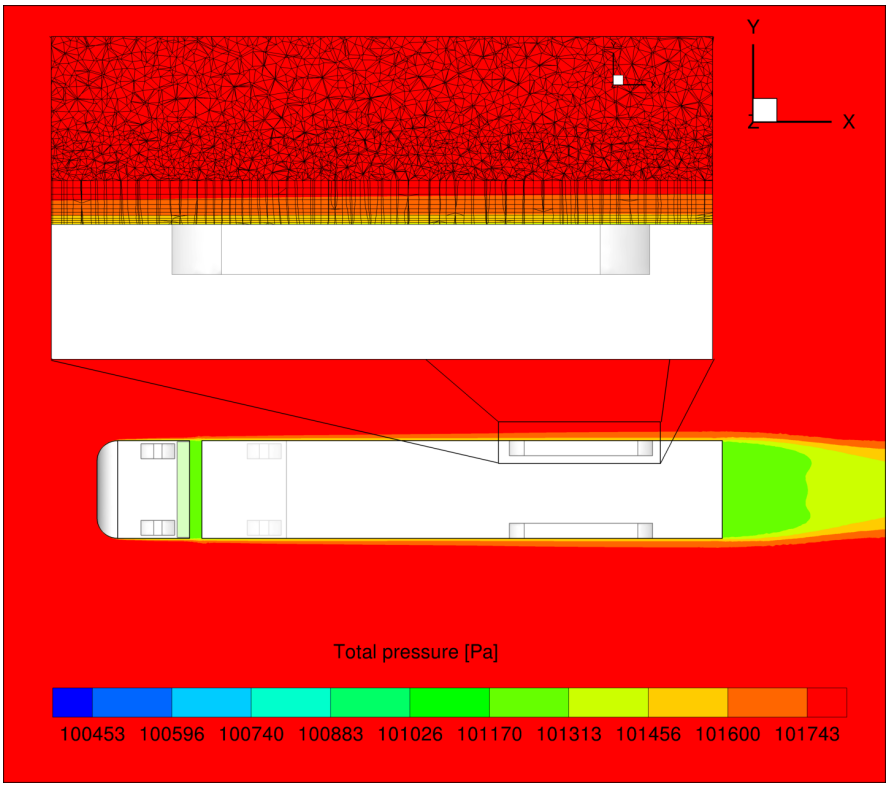

Figure 3.4: A close-up of the mesh at the boundary layer of the trailer

3.1.4 Solver settings

Once the complete mesh is defined and created in Ansys ICEM it can be imported in Ansys Fluent. Before the actual computations can start one has to select several solver settings. The first solver setting is the simulation method. As was mentioned before a RANS simulation with the $\kappa - \omega$ SST closure model is the most suitable numerical method to simulate the flow around heavy-duty vehicles. It was decided to apply a coupled solver for the pressure-velocity coupling as this results in faster convergence of the solution according to SAE (2013). The first 200 iterations are performed with the first order upwind spatial discretization of the momentum, turbulent kinetic energy and specific dissipation rate. For the pressure the standard discretization method is selected. After those 200 iterations the settings for the spatial discretization are changed to second order discretization and another 2,800 iterations are performed.

The goal was to perform the numerical analysis with similar flow properties as during the wind tunnel experiment. The turbulence intensity was set equal to the turbulence intensity of the Open Jet Facility (OJF), the wind tunnel used for the experimental part of this study (see subsection 4.1.2). The turbulence intensity of the OJF is around 0.3% at a free stream velocity of 27.2 m/s [1]. No data was available about the turbulent length scales of the flow

[1]The value of the turbulence intensity was determined during a discussion with the head of the wind tunnel laboratories, ir. Timmer

inside the test section of the OJF. The turbulent length scale was then based on half the width of the model (0.1625 m), as was also done by van Leeuwen (2009) in his RANS simulations. This is slightly lower than the values of McAuliffe et al. (2014), which are between 0.6 m and 4.7 m. However these values are measured outside on the road and not in a wind tunnel test section.

The number of iterations was determined by looking at the convergence history of the computed simulations. First of all it was observed that for not one case the drag coefficient converged to a specific value, instead it converged with low amplitude oscillations. The amplitude of the oscillations and the number of iterations needed to obtain convergence was highly dependent on the configuration, the yaw angle and the density of the mesh. This is clearly visible in Figure 3.5, which shows the convergence history of the drag coefficient for 4 different cases: the S-E and the M-E baseline model at a yaw angle of 0° and 3°. To make sure that for every case the solution was converged, it was decided to perform in total 3,000 iterations for each case. To average out the effect of the oscillations the drag coefficient was calculated by taking the average of the last 1,500 iterations. Note that all the contour plots, other graphical figures and pressure values on the surface of the model are based on the values of the last iteration.

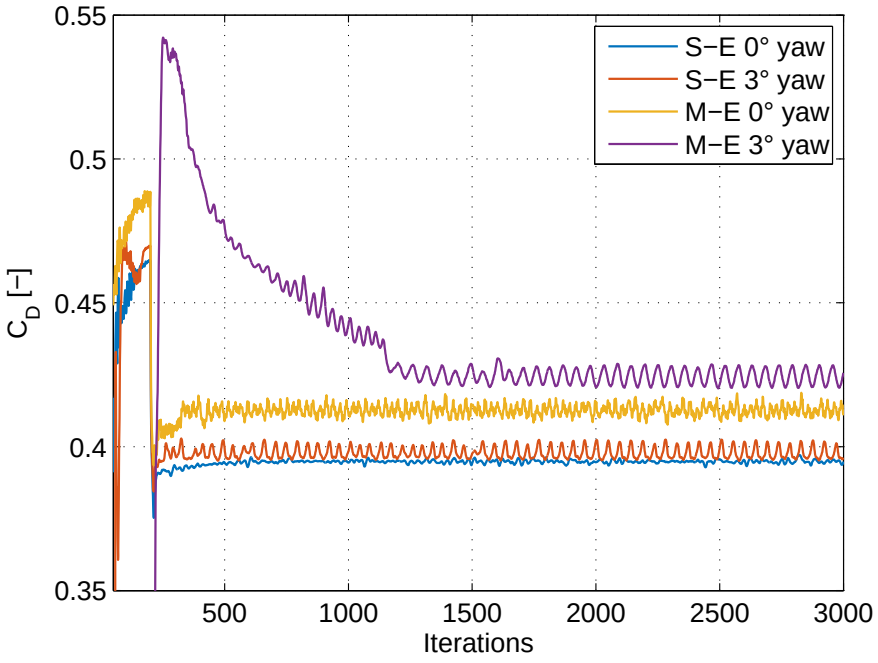

Figure 3.5: Convergence history of the drag coefficient for 4 different cases

3.1.5 Mesh sensitivity

As was explained in subsection 3.1.2 the computational domain contains 3 density boxes which refine the mesh around the heavy-duty vehicle model. The results of the numerical

simulations are dependent on the refinement of these density boxes and thus also on the mesh size. However the larger the mesh size, the more computational power is required to perform the computations. Therefore a mesh sensitivity analysis should be performed in order to determine the refinement of the density boxes and the mesh size.

In order to determine the most suitable mesh size 8 different meshes were developed for the S-E baseline configuration at 0° yaw angle. All the 8 meshes contain the 3 density boxes and also the ratio of refinement between the density boxes is kept the same. Figure 3.6 shows the results of the performed mesh sensitivity study. As can be seen in 3.6(a) the mesh size clearly influences the drag coefficient. In general the drag coefficient decreases with increasing mesh size, but a significant drop in drag coefficient can be observed between mesh 3 and mesh 4. Once the number of cells is larger than approximately $5 \cdot 10^6$ (mesh 4), the decay in drag coefficient is much smaller. As was explained ealier the drag coefficient does not converge to one specific value, but instead it slightly fluctuates around a certain value. As can be seen in 3.6(b) the amplitude of these oscillations depends from mesh to mesh. However no clear relation can be drawn between the mesh size and the amplitude of the oscillations. The error bars in 3.6(a) represent these fluctuations. After this mesh sensitivity analysis it was decided to use mesh 6 as the standard mesh size for all computations. Adding more cells increases the computational requirements much, while it does not significantly affect the drag coefficient.

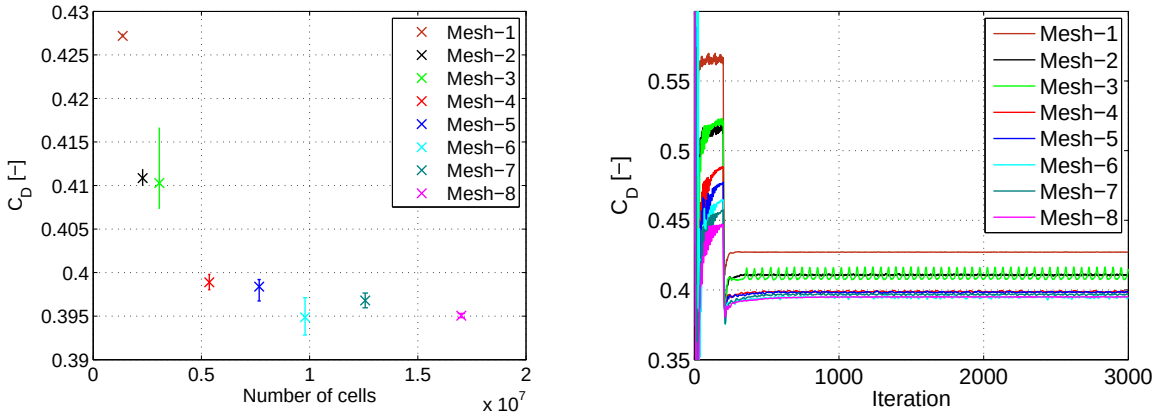

(a) Drag coefficient as a function of the mesh size

(b) Convergence history of the drag coefficient for the different mesh sizes

Figure 3.6: Mesh sensitivity

The standard mesh size that is used during this computational study is shown in Figure 3.7. In this figure the mesh refinements of the different density boxes is clearly visible.

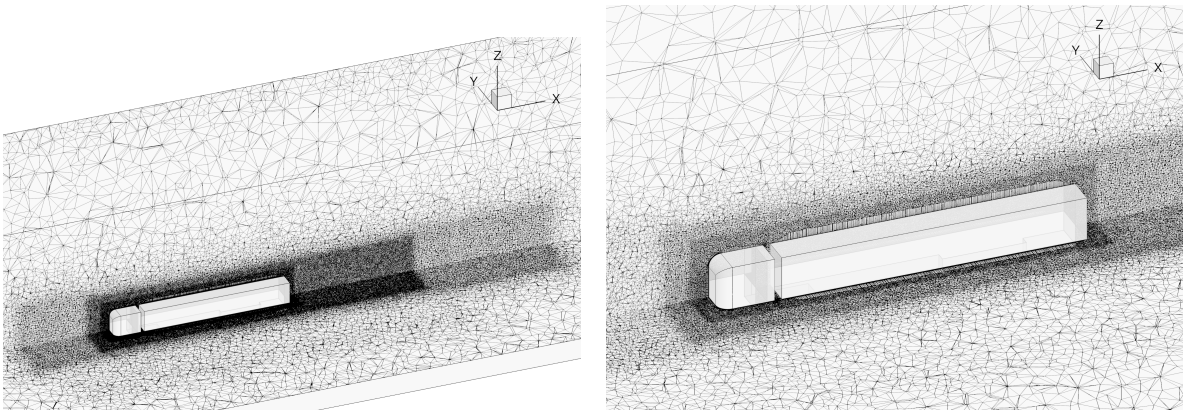

(a) Zoom-out view of the mesh

(b) Close-up of the mesh

Figure 3.7: Mesh

The same meshing strategy was applied for all the configurations, but it was slightly adjusted in the case of crosswind. In the case of crosswind one wants to have a fine mesh at the leeward side of the model such that all the relevant flow phenomena like separation can be accurately captured. So for simulations at 6°, 9° and 12° yaw angle the density boxes were moved to the leeward side of the model. This is shown in Figure 3.8, the left figure is the mesh for simulations at 0° and 3° yaw angle, while 3.8(b) shows the mesh for simulations at 6° and 9° yaw angle.

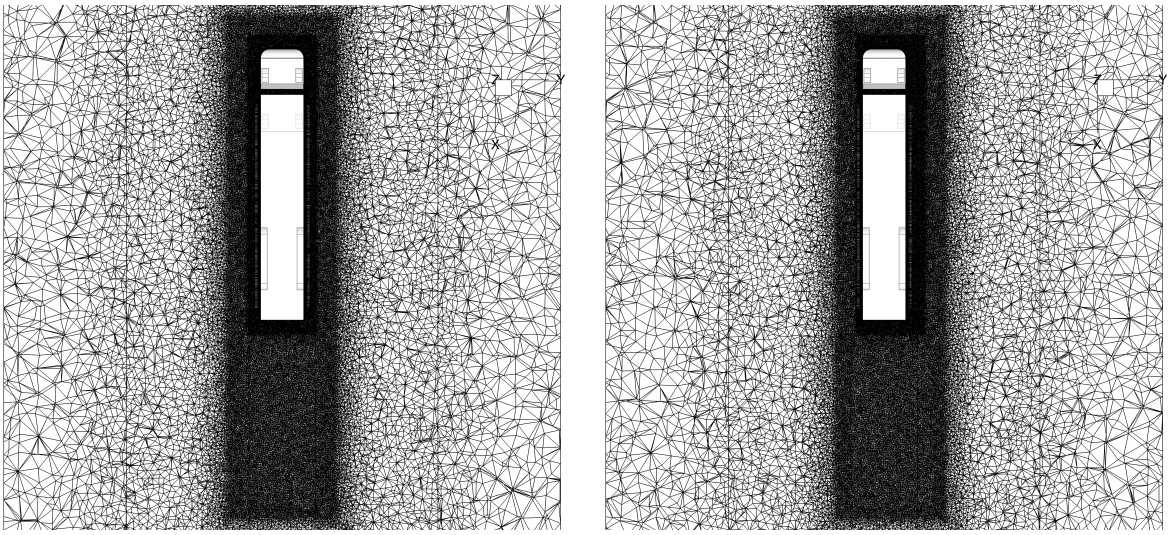

(a) Mesh for the S-E baseline configuration at 0°

(b) Mesh for the S-E baseline configuration at 6°

Figure 3.8: Mesh

3.2 Numerical results

3.2.1 The baseline configurations

Drag contribution of the vehicle parts

The advantages of CFD are that it can easily give more insight into the flow behavior and that it can deliver a detailed analysis of the flow field. CFD is able to show which parts of the heavy-duty vehicle contribute to the drag force and can split these contributions into a viscous and a pressure drag component. The results for the S-E baseline configuration at a yaw angle of 0° are shown in Table 3.3. Due to the limited post-processing capabilities of Fluent, the values in this table are from the last iteration and not an average value of the last 1,500 iterations. In this table the names of all the parts that form the cabin start with "C_", for the trailer with "T_". The parts that begin with "C_SE" are the surfaces at the inner side of the side and roof extenders. The outer surfaces of the extenders are included in "C_top", "C_left" and "C_right". An overview of all the parts and their names can be found in section A.1.

Several interesting facts can be observed from Table 3.3. Firstly it can be noted that the symmetric parts contribute equally to the drag. Both the left and the right side of the cabin (respectively C_left and C_right) are responsible for 0.9% of the drag of the entire vehicle. The same is valid for the left and right side of the trailer (T_left and T_right). This was expected as at 0° yaw angle the incoming flow is aligned with the model. Secondly 83.2% of the drag is pressure drag, which is almost 5 times more than the viscous drag. This agrees with what was found in literature, amongst others the truck-trailer combination analyzed by Buijs (2010) had 85.2% pressure drag of the total drag. When one takes a closer look at the distribution of the drag contributing parts, one can see that the largest drag contributing parts are the cabin base surface (C_back) and the trailer base surface (T_back). The flat part of the cabin frontal surface (C_front_front) also generates a great amount of drag (0.360) as it experiences full stagnation flow, but this is counteracted by the thrust generating curved surfaces of the cabin frontal surface (C_front_left, C_front_right and C_front_top). These surfaces generate thrust as the rounded shape creates suction. Furthermore the trailer frontal surface (T_front) creates thrust as it is in the low pressure region of the tractor-trailer gap. Because of this thrust generating trailer frontal surface, the total drag of the trailer is low, namely only 0.079, which is 19.9% of the drag of the total vehicle. Lastly it is interesting to note that the sum of the drag contribution of the trailer frontal surface (T_front) and the base of the cabin (C_back) is 3.9% or 15 drag counts. This implies that the tractor-trailer gap is responsible for 3.9% of the total drag of the S-E baseline configuration. If one also includes the lower back side of the cabin (C_back_back), the tractor-trailer gap is responsible for 13.1% or 52 drag counts of the total drag of the vehicle.

A similar analysis can be performed for the three other baseline configurations which contain a gap. In Table 3.4 the drag contributions of the different parts of the four baseline configurations are presented. In this way the effect of increasing the tractor-trailer gap or removing the side and roof extenders can be studied in more detail.

Table 3.3: Drag contribution of the different parts of the S-E baseline configuration at a yaw angle of 0°

Part	$C_{T_{pressure}}$	$C_{T_{viscous}}$	**Total** C_T	**Percentage [%]**
C_front_front	0.360	0	0.360	91.2
C_front_left	-0.123	0.003	-0.120	-30.4
C_front_right	-0.122	0.003	-0.120	-30.3
C_front_bottom	0.023	0.001	0.024	6.1
C_front_top	-0.079	0.002	-0.077	-19.5
C_left	0	0.004	0.004	0.9
C_right	0	0.004	0.004	0.9
C_bottom	0	0.004	0.004	1.0
C_top	0	0.002	0.002	0.5
C_back	0.161	0	0.161	40.9
C_back_back	0.036	0	0.036	9.2
C_mid	0	0.001	0.001	0.1
C_wheels	0.032	0.000	0.032	8.2
C_SE_left	0	0	0	0
C_SE_right	0	0	0	0
C_SE_top	0	0	0	0
C_SE_back	0.005	0	0.005	1.3
Total Cabin	0.293	0.022	0.316	80.1
T_front	-0.146	0	-0.146	-37.0
T_left	0	0.014	0.014	3.5
T_right	0	0.014	0.014	3.5
T_bottom	0	0.003	0.003	0.7
T_top	0	0.012	0.012	3.1
T_back	0.123	0	0.123	31.1
T_wheels	0.057	0.002	0.059	14.9
Total Trailer	0.034	0.044	0.079	19.9
Total Vehicle	0.329	0.066	0.395	100
Percentage [%]	83.2	16.8	100	

Table 3.4: Drag contribution of the different parts of the baseline configurations

Part	$C_{T_{S-E}}$	**S-E %**	$C_{T_{S-NE}}$	**S-NE %**	$C_{T_{M-E}}$	**M-E %**	$C_{T_{L-E}}$	**L-E %**
C_front_front	0.360	91.2	0.360	87.1	0.360	87.6	0.360	80.1
C_front_left	-0.120	-30.4	-0.120	-28.9	-0.119	-29.0	-0.118	-26.1
C_front_right	-0.120	-30.3	-0.118	-28.5	-0.119	-28.8	-0.116	-25.7
C_front_bottom	0.024	6.1	0.025	6.0	0.025	6.0	0.027	6.0
C_front_top	-0.077	-19.5	-0.077	-18.7	-0.077	-18.8	-0.077	-17.2
C_left	0.004	0.9	0.003	0.7	0.004	0.9	0.003	0.8
C_right	0.004	0.9	0.003	0.8	0.004	0.9	0.003	0.7
C_bottom	0.004	1.0	0.004	1.0	0.004	1.0	0.004	0.9
C_top	0.002	0.5	0.002	0.4	0.002	0.5	0.002	0.4
C_back	0.161	40.9	0.162	39.2	0.067	16.2	0.055	12.2
C_back_back	0.036	9.2	0.034	8.1	0.036	8.6	0.037	8.1
C_mid	0.001	0.1	0.001	0.1	0.001	0.2	0.0	0.0
C_wheels	0.032	8.2	0.030	7.3	0.031	7.5	0.031	6.8
C_SE_left	0.0	0.0	-	-	0.0	0.0	0.0	0.0
C_SE_right	0.0	0.0	-	-	0.0	0.0	0.0	0.0
C_SE_top	0.0	0.0	-	-	0.0	0.0	0.0	0.0
C_SE_back	0.005	1.3	-	-	0.005	1.2	0.0040	0.9
Total Cabin	0.316	80.1	0.309	74.6	0.222	54.0	0.216	47.9
T_front	-0.146	-37.0	-0.120	-29.1	-0.027	-6.5	0.032	7.2
T_left	0.014	3.5	0.014	3.3	0.013	3.1	0.011	2.4
T_right	0.014	3.5	0.014	3.3	0.013	3.1	0.011	2.3
T_bottom	0.003	0.7	0.002	0.5	0.002	0.5	0.002	0.3
T_top	0.012	3.1	0.012	2.9	0.011	2.7	0.011	2.4
T_back	0.123	31.1	0.134	32.5	0.130	31.5	0.135	29.9
T_wheels	0.059	14.9	0.049	11.9	0.048	11.6	0.034	7.6
Total Trailer	0.079	19.9	0.105	25.4	0.189	46.0	0.234	52.1
Total Vehicle	0.395	100.0	0.413	100.0	0.411	100.0	0.450	100.0

First let us have a look at the differences between the S-E and the S-NE baseline configuration, respectively the test model with and without side and roof extenders. From Table 3.4 it is clear that the total drag coefficient of the S-NE baseline configuration is appropriately 18 drag counts (4.6%) higher than the total drag coefficient of the S-E baseline configuration. Regarding the cabin there is not much difference between the two baseline configurations. The cabin of the S-NE baseline configuration generates only 7.5 drag counts less than the S-E configuration. This difference is mainly coming from the viscous drag created by the presence of the extenders (C_SE_back). Furthermore a small difference can be observed for C_left, C_right and C_top, which is also directly related to the presence of the side and roof extenders. Removing the side and roof extenders from the cabin, decreases the total length of the side and the top surfaces of the cabin, which results in a lower viscous drag. More interesting observations can be made when one looks at the contribution of the trailer parts. The trailer of the S-NE baseline configuration has a drag coefficient of 0.105, which is significantly higher than the drag coefficient of the S-E trailer, which is only 0.079. This is mainly caused by the fact that in the case of extenders (i.e. S-E configuration), the trailer frontal surface (T_front) has a more negative drag coefficient. Adding extenders to the cabin creates a lower pressure region in the tractor-trailer gap which generates extra suction on the trailer frontal surface. Furthermore the drag of the base of the trailer (T_back) is slightly increased from 0.123 to 0.134 when the extenders are removed from the vehicle. Finally by summing the drag coefficient of C_back and T_front one can determine the drag caused by the tractor-trailer gap. For the S-E case this equals 15 drag counts, while for the S-NE configuration it is equal to 42 drag counts. So clearly the extenders reduce the drag caused by the tractor-trailer gap.

The most striking effect that is noticed when the tractor-trailer gap length is increased, is that drag coefficient of the cabin decreases, while the drag coefficient of the trailer and of the total vehicle significantly increases. For the S-E configuration the cabin is responsible for 80.1% of the drag, while for the L-E configuration the cabin is only responsible for 47.9%. One can clearly see that the drag coefficient of C_back drastically decreases with increasing gap length. The drag coefficient of C_back equals 0.161 for the S-E case, while for the L-E model it is equal to 0.055. This is a decrease of 106 drag counts. When the tractor-trailer gap length is increased the low pressure in the gap region increases as well. Also both the pressure coefficient on the base surface of the cabin (C_back) and on the trailer frontal surface (T_front) increases when the gap length is increased (this will also be discussed in the following subsubsection). This means that in the case of the L-E baseline model the difference in pressure between the front and the back of the cabin is not that large as compared to the S-E baseline model. This results in a lower pressure drag of the cabin for the L-E baseline model.

Another interesting observation is that the trailer frontal surface (T_front) of the S-E baseline configuration has a drag coefficient of -0.146, but for the L-E baseline configuration it has a positive drag coefficient of 0.032. At small gap lengths the trailer frontal surface experiences suction caused by the low pressure region in the gap, while for large gap lengths this effect is almost completely disappeared as the trailer is placed further away from the cabin. The sum of the drag coefficient of T_front and C_back can be considered as the drag caused by the tractor-trailer gap. For the S-E baseline configuration this value is only 15 drag counts (3.9%), but for the M-E baseline configuration this value is already 40 drag counts (9.7%) and for the L-E baseline configuration it goes up to 87 drag counts (19.3%). Moreover the drag

coefficient of the top, bottom and sides of the trailer decreases with increasing gap length. This is because the length of the trailer is reduced when the tractor-trailer gap length is increased. This leads to lower viscous drag coefficients as the length of the top, bottom and sides of the trailer is reduced.

Finally it is interesting to note that the drag caused by tractor-trailer gap is 2 drag counts lower for the M-E baseline configuration compared to the S-NE baseline configuration, although the M-E configuration has a much larger tractor-trailer gap. In this way the beneficial effect of the extenders is clearly visible, as the S-NE configuration has no extenders.

Flow behavior in the tractor-trailer gap

Now that the drag coefficient has been discussed in more detail, the flow field inside the tractor-trailer gap of the heavy-duty vehicle will be analyzed in more detail. Figure 3.9 shows the streamlines with the velocity magnitude around the frontal part of the L-E baseline configuration at 0° yaw angle. From the figure it is obvious that the free stream flow at a velocity of 27.2 m/s stagnates at the frontal surface of the cabin, then the flow accelerates due to the curved shape of the rounded edges of the cabin. At this point the flow accelerates to a velocity of more than 40 m/s. Subsequently the air flows along the top and the sides of the cabin and then a significant amount of the flow enters the tractor-trailer gap, which is clearly visible from Figure 3.9. The flow enters the tractor-trailer gap as there is a low pressure region in the gap. The flow from the top is bended downwards into the gap while the flow coming from the sides is deflected horizontally into the gap. Subsequently the flow impinges on the trailer frontal surface and then vortices develop in the tractor-trailer gap. As can be seen in Figure 3.9 at the bottom of the tractor-trailer gap air exits the gap underneath the trailer at a low velocity of maximum 15 m/s. Also from the sides, at the bottom of the gap, flow exits the gap. Furthermore no flow separation was observed at the top and side leading edges of the trailer.

The description of the blow behavior given in the previous paragraph is in general valid for the three different gap length cases (S-E & S-NE, M-E and L-E) as can be seen in Figure 3.10, which shows the streamlines with the velocity magnitude for the M-E configuration at a yaw angle of 0°. The flow accelerates over the rounded edges of the cabin, flows along the sides and the top of the cabin and then enters the tractor-trailer gap where the air hits the trailer frontal surface. Although the flow behavior is in general similar when the gap length is reduced, there are some differences, which will be discussed in the following paragraphs.

In Figure 3.11 the pressure coefficient on the trailer frontal surface of the S-E, M-E and L-E baseline configurations at 0° yaw angle is presented. Here one can clearly see the impact of the gap length on the pressure on the trailer frontal surface. For the S-E baseline configuration the pressure coefficient lies in general around -0.25 and -0.1. However on the upper edges of the surface, both the complete horizontal edge as the upper part of the left and right edge, the pressure coefficient is significantly higher, namely around 0.15. This is caused by the air coming from on top of the cabin and from the sides of the cabin entering the tractor-trailer gap. The flow is slightly bended inwards into the tractor-trailer gap and impinges on the upper outer regions of the trailer frontal surface, creating the higher pressure region around

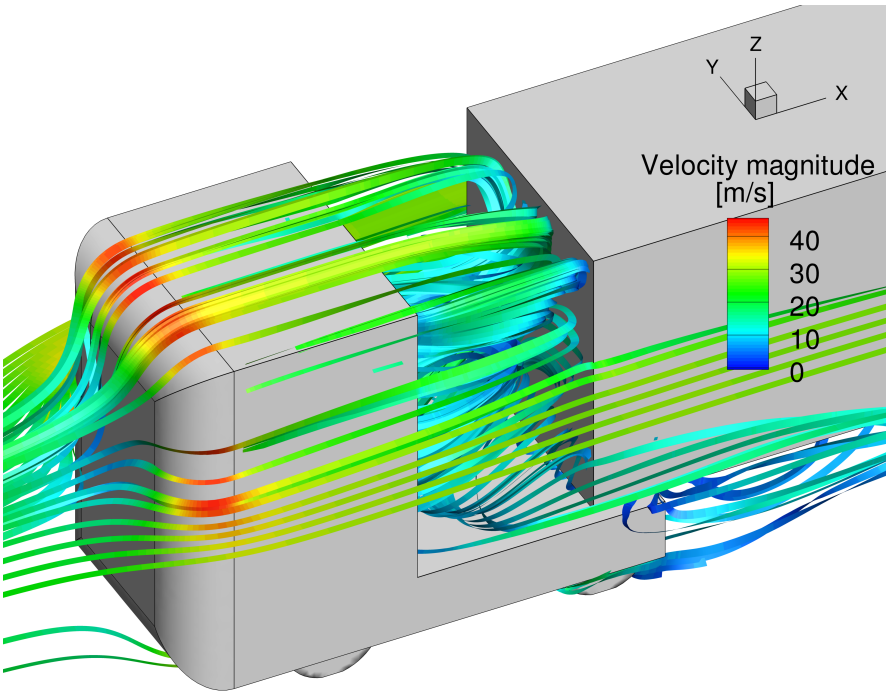

Figure 3.9: Streamlines with the velocity magnitude for the L-E baseline configuration at 0° yaw angle

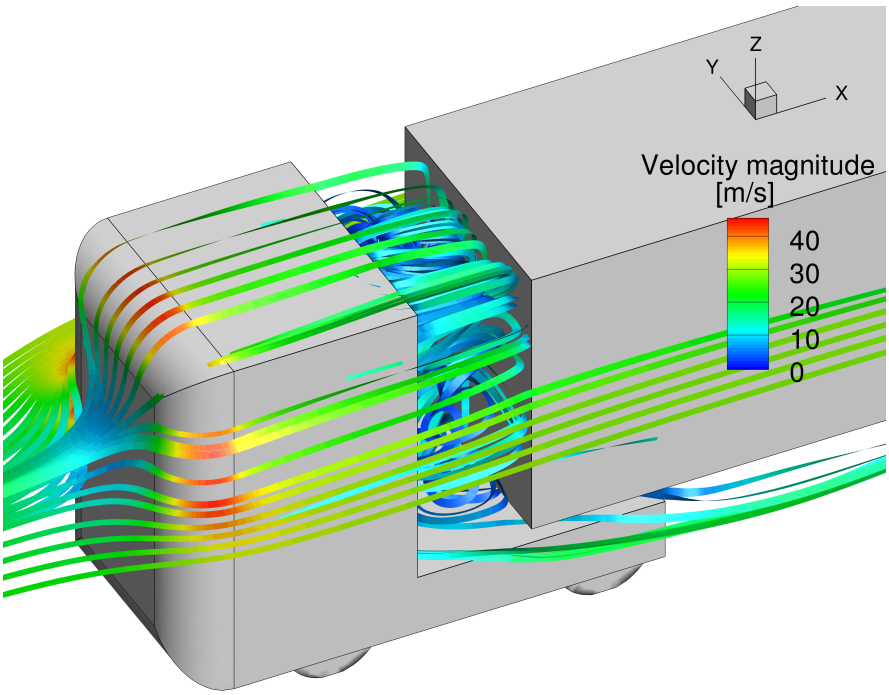

Figure 3.10: Streamlines with the velocity magnitude for the M-E baseline configuration at 0° yaw angle

the edges. This inward movement of the flow into the tractor-trailer gap is clearly visible in the contour plots with streamlines shown later on in this section (see Figure 3.14 and Figure 3.15).

A similar pattern can be observed for the M-E baseline configuration (3.11(c)), although the pattern is in this case a bit more extreme. The pressure coefficient on the outer regions of the surface goes up to 0.7 as more air can easily enter the gap. Furthermore two diagonal higher pressure regions can be observed in the inner region where the pressure coefficient is around 0.15. These two diagonal higher pressure regions can also be seen in a lesser extent on the S-E and the L-E case. These diagonal high pressure regions were also observed by Buijs (2010) on the trailer frontal surface of a truck-trailer combination. According to Buijs (2010) these diagonal high pressure regions can be explained by the fact that the flow stream coming from above the cabin and the flow stream coming from the side of the cabin merge and impinge on the diagonals of the trailer frontal surface. Furthermore the pressure distribution is approximately symmetric for all the three cases, which was expected as the yaw angle is 0°.

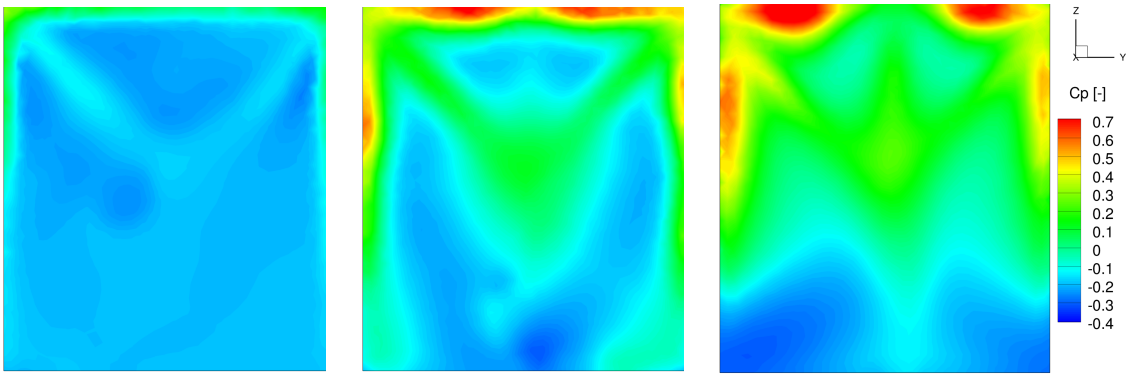

(a) S-E (b) M-E (c) L-E

Figure 3.11: Pressure coefficient on the trailer frontal surface at 0° yaw angle

Now that it is clear how the gap length affects the pressure distribution on the trailer frontal surface, the effect of the extenders on the trailer frontal surface will be discussed. Figure 3.12 shows the pressure coefficient distribution on the trailer frontal surface for the S-NE baseline configuration. When one compares this with 3.11(a) the influence of the extenders on the surface can be clearly observed. The general shape of the pressure distribution is similar between the two cases, but the value of the pressure coefficient is higher when there are no extenders attached to the cabin. This is highlighted by the upper outer region of the surface where the pressure coefficient can reach values of up to 0.6 when the cabin is not equipped with extenders. For the S-E baseline configuration, where the cabin is equipped with extenders, the maximum pressure coefficient was only around 0.15.

To make the analysis of the pressure distribution on the trailer frontal surface complete, the average pressure coefficient of the whole surface was computed for each baseline design. As can be seen from Table 3.5 the average pressure coefficient on the trailer frontal surface of

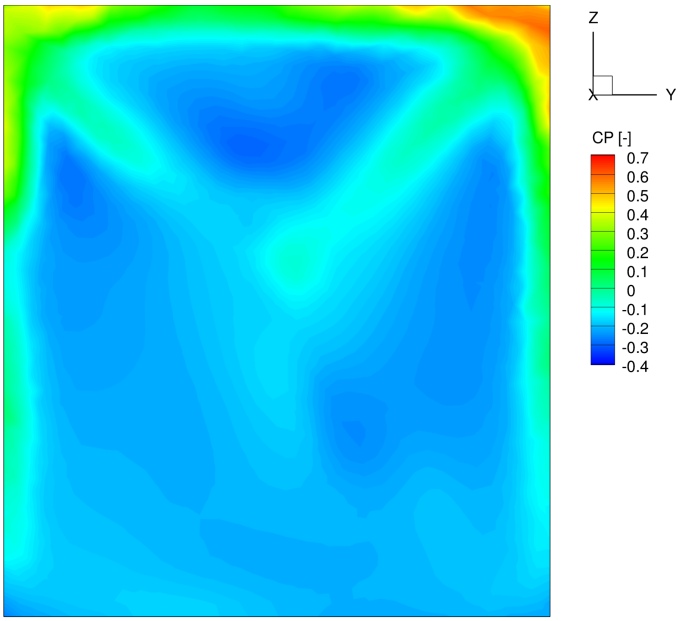

Figure 3.12: Pressure coefficient on the trailer frontal surface of the S-NE baseline configuration at 0° yaw angle

the S-E, S-NE and M-E configuration is negative, which means that the trailer is sucked forwards in the direction of the free stream flow. The average pressure coefficient on the surface increases with increasing gap length. For the L-E case it increases up to a positive value of 0.041. Omitting the extenders from the cabin also leads to a higher average pressure coefficient. This agrees with the findings of the detailed analysis of the pressure distribution on the trailer frontal surface. In addition it also agrees with the detailed analysis of the drag contributing parts (Table 3.4). There it was seen that thrust is created by the trailer frontal surface for the S-E, S-NE and M-E configuration, but drag for the L-E case.

Table 3.5: The average pressure coefficient on the trailer frontal surface of the baseline configurations at 0° yaw angle

	S-E	**S-NE**	**M-E**	**L-E**
Average C_P [-]	-0.186	-0.153	-0.035	0.041

Besides the pressure distribution on the trailer frontal surface also the pressure distribution on the lower base surface of the cabin will be analyzed. In Table 3.4 this surface is referenced as C_back_back. Figure 3.13 shows the pressure coefficient on the lower base surface for the S-E and the L-E baseline model. Only these two baseline models are shown as they represent the extrema of the gap geometry, namely respectively the smallest and the largest gap length. As can be seen in the figure the difference between the pressure distributions of the two models is very small. In both pressure distributions a less negative pressure region is visible in the middle of the surface. Also the difference in average pressure coefficient of the surface of the two models is very small. For the L-E baseline model the average pressure coefficient is -0.211, while it is equal to -0.209 for the S-E baseline model. This agrees with the detailed analysis

of the drag contributing parts (Table 3.4) where the difference between the two surfaces was only 1 drag count.

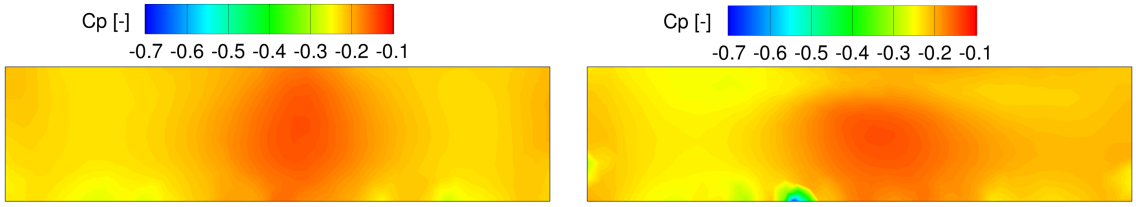

(a) S-E (b) L-E

Figure 3.13: Pressure coefficient on the lower base surface of the cabin at 0° yaw angle

To obtain a better understanding of the flow behavior inside the tractor-trailer gap contour plots of the z-velocity including X-Y streamlines were created. The results for the S-E, S-NE, M-E and L-E baseline configuration are shown in Figure 3.14. The four configurations show a similar flow behavior inside the tractor-trailer gap, namely two large counter-rotating vortices. As was described in section 1.3 these two symmetric vortices were also observed by Hammache and Browand (2004) in the gap of a very simplified tractor-trailer model. As can be seen in Figure 3.14 the shape of the vortices depends on the gap length. For the S-E and the S-NE case the two vortices are stretched along the width of the vehicle, while for the L-E configuration the vortices are rather stretched in the longitudinal direction. In the former case the vortices are not as symmetric and uniform as compared to the M-E and L-E configuration. In the latter case the flow inside the tractor-trailer gap is more similar as the flow in the wake of a heavy-duty vehicle. Furthermore the location of the vortex cores is dependent on the configuration. Regarding the S-E, S-NE and the M-E baseline model the longitudinal position of the vortex core moves downstream when the effective gap length is increased. However, this is not valid for the L-E baseline model, since the vortex cores inside the gap of the L-E model are located closely to the base of the cabin. A similar pattern can be observed for the lateral location of the vortex core. The vortex cores are located further away from the symmetry plane when the effective gap length is increased, but this is only valid from the S-E model until the M-E model. The vortex cores of the L-E configuration are again located closer to the symmetry axis.

The streamlines in Figure 3.14 show that flow is entering the tractor-trailer gap from the sides and subsequently impinges on the trailer frontal surface as was mentioned before. This is especially clearly visible for the M-E and L-E configuration. Furthermore a large amount of downwards flow can be observed close to the trailer frontal surface in the middle of the width of the model. This downwards stream is increasing in strength and size when the gap length is increased. Vertical cut-outs were made in the symmetry plane to give more insight on this downwards stream. The results are shown in Figure 3.15. As can be seen from the figure a large amount of air flows downwards from the top of the trailer frontal surface diagonally to the bottom of the cabin base. This is caused by a lower pressure region in the tractor-trailer gap. From the bottom of the base two distinctive flow patterns are observed. On the one hand air flows from the bottom of the cabin base through the horizontal gap between the

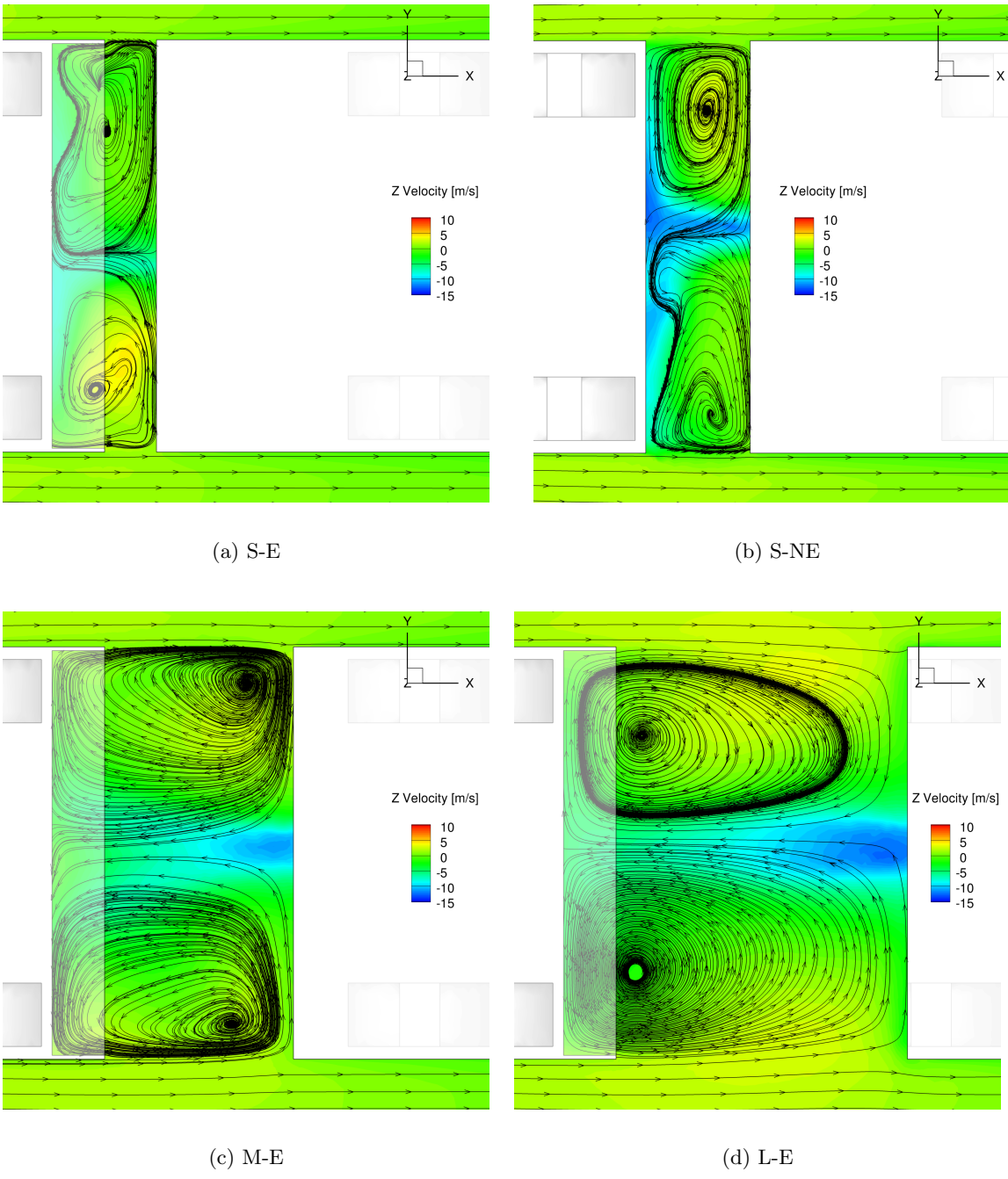

(a) S-E

(b) S-NE

(c) M-E

(d) L-E

Figure 3.14: Contour plot of the Z-velocity (positive direction is towards the reader) with arrows indicating the X-Y velocity streamlines at the middle of the gap height

trailer and the tractor to the underbody of the trailer. On the other hand air flows from the bottom of the cabin base sideways and leaves the tractor-trailer gap via the left or right side of the gap. For the L-E case a small amount of air flows vertically from the top to the bottom of the trailer frontal surface and leaves directly the tractor-trailer gap via the bottom of the

trailer. Regarding the S-E and the S-NE baseline model this does not happen, but instead a vortex can develop at the bottom of the gap. Above the large diagonal movement of the flow a large recirculation develops. This large recirculation is clearly visible for all the baseline configurations. Finally a large region of separated flow can be observed behind the lower base surface of the cabin (C_back_back).

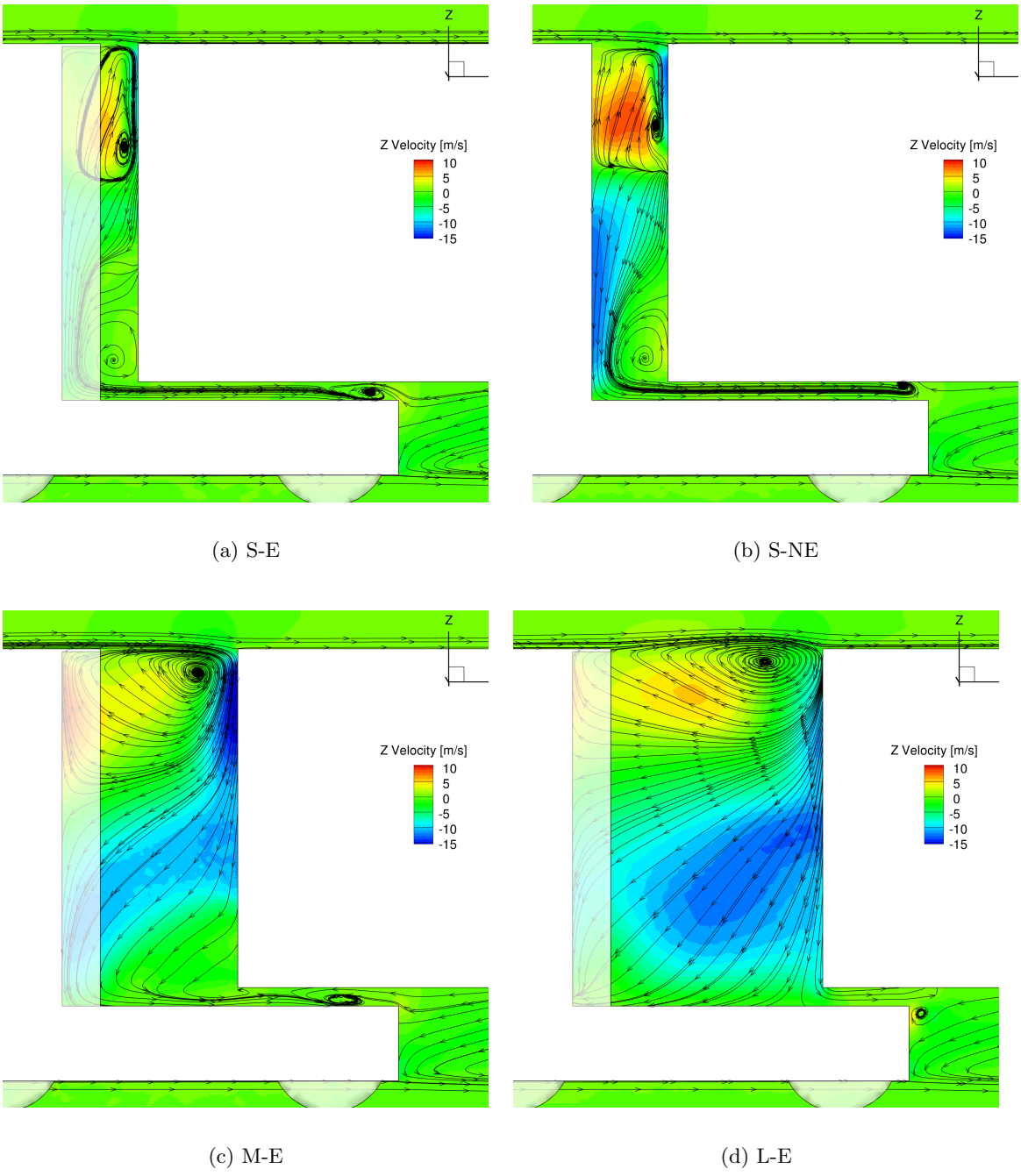

(a) S-E

(b) S-NE

(c) M-E

(d) L-E

Figure 3.15: Contour plot of the Z-velocity with arrows indicating the X-Z velocity at the middle of the model's width

Flow behavior in the wake of the heavy-duty vehicle

As was discussed in section 3.2.1 the length of the tractor-trailer gap influences the drag generated by the trailer base surface (T_back). For example as was shown in Table 3.4 the base surface of the S-E trailer has a drag coefficient of 0.123, while for the L-E configuration the base of the trailer has a drag coefficient of 0.135. As the base of the trailer is responsible for around 30% of the drag, a closer look has to be taken into this part of the heavy-duty vehicle.

The pressure coefficient distribution on the trailer base surface for the S-E and the L-E baseline configuration is shown in Figure 3.16. The pressure coefficient distribution on the base surface is very similar to what was found by Buijs (2010) for a truck-trailer combination and to what was determined by van Leeuwen (2009) for the GETS model. It is clear from Figure 3.16 that the length of the tractor-trailer gap influences the pressure distribution on the trailer base surface. For the S-E baseline configuration the average pressure coefficient on the trailer base surface is -0.1568, while for the L-E baseline configuration the average pressure coefficient equals -0.1716. Furthermore the typical circular high negative pressure coefficient region is also located higher on the trailer base surface for the L-E baseline configuration.

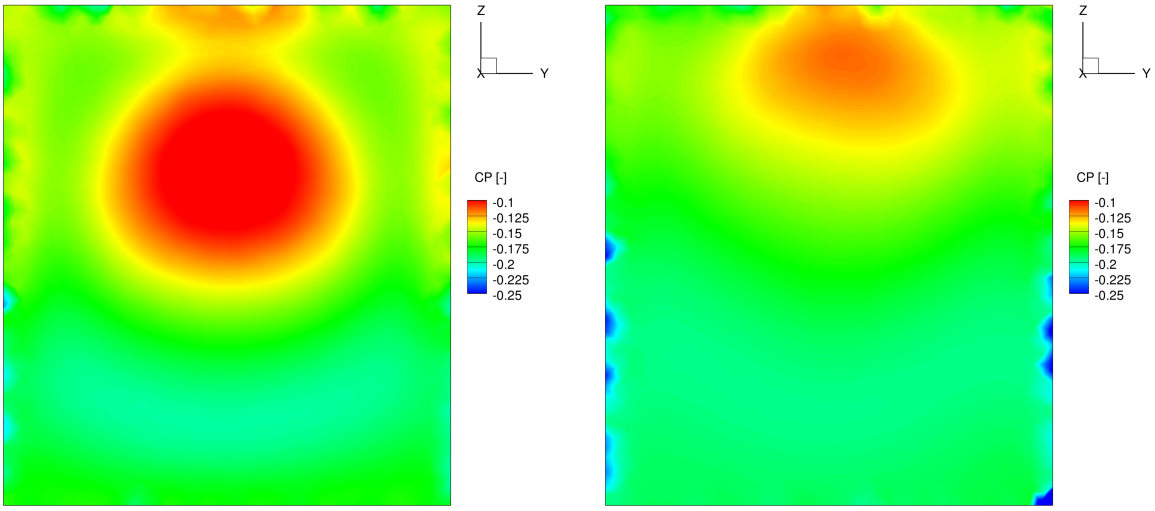

(a) S-E (b) L-E

Figure 3.16: Pressure coefficient distribution on the trailer base surface

Figure 3.17 shows the velocity magnitude in the wake of the heavy-duty vehicle for the S-E and the L-E baseline configuration. As expected the velocity in the wake is much lower than the free stream velocity of 27.2 m/s. The shape of the wake is slightly different for the L-E configuration than for the S-E configuration, however both contain two large counter-rotating vortices. These counter-rotating vortices are also observed in other research studies, amongst others by Gheyssens (2016) for the GETS model. Although both the wake of the L-E and the S-E model contain two large counter-rotating vortices, some differences can be observed between the two wakes. The vortex cores in the wake of the L-E baseline model are located

significantly closer to the trailer base surface (i.e. more upstream in longitudinal direction). Also the saddle point is positioned closer to the trailer base surface in the case of the L-E baseline model. The width of the wake downstream of the saddle point is smaller for the L-E model compared to the S-E model. Furthermore the boundary layer is approximately twice as thick for the L-E baseline model than for the S-E baseline model.

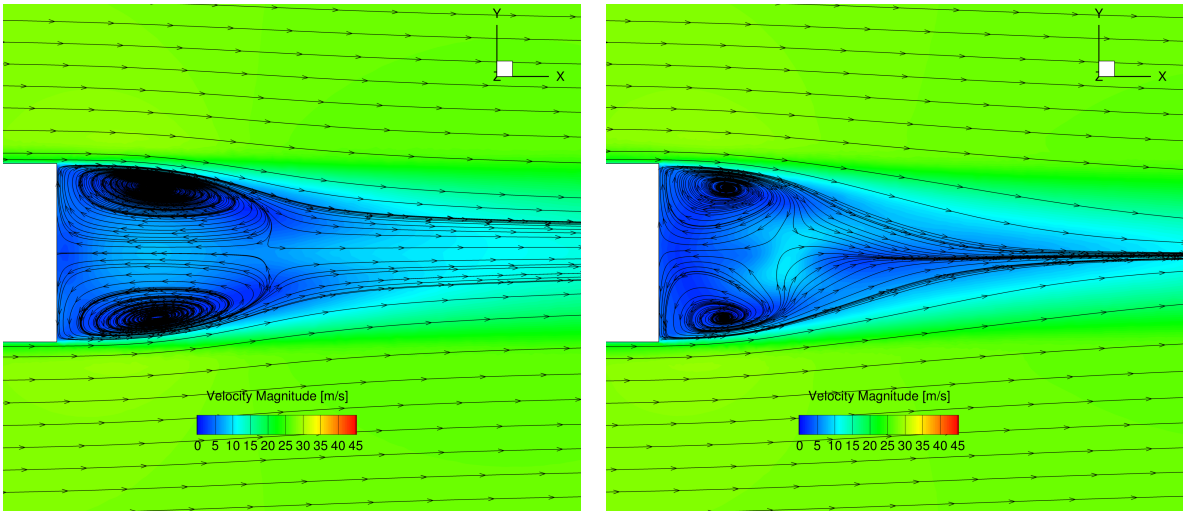

(a) S-E model

(b) L-E model

Figure 3.17: Velocity magnitude contour plot with the X-Y velocity streamlines at half the height of the trailer in the wake of the heavy-duty vehicle

3.18(a) shows the flow field of the wake of the S-E baseline model in the symmetry plane. The flow field of the wake is very comparable with the flow field of the wake of the North-American GCM model numerically (RANS) analyzed by Pointer (2004) at a Reynolds number of $1.15 \cdot 10^6$ based on the width of the vehicle. The most striking from the figure is the distinct stream of air coming from under the trailer flowing upwards in the wake of the vehicle. The velocity of this stream is around $20 - 25\ m/s$, which is significantly higher than the velocity of the flow inside the wake, which is around $0 - 10\ m/s$. This distinct stream coming from under the trailer is also present on the wakes of the other baseline models. If one looks at the flow field underneath the trailer (see 3.18(b)), one can see that there is large amount of air that enters the underbody of the vehicle from the sides and then flows underneath the trailer between the aft wheels. This large amount of air that enters the the underbody at a high velocity is causing the upwards stream in the wake which is visible in 3.18(a).

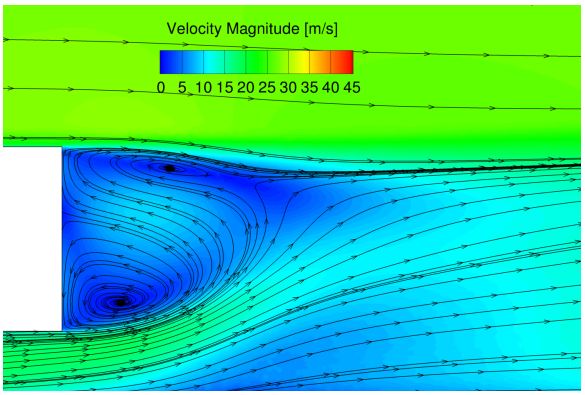

(a) Velocity magnitude contour plot with the X-Z velocity streamlines at the symmetry plane in the wake of the S-E baseline model

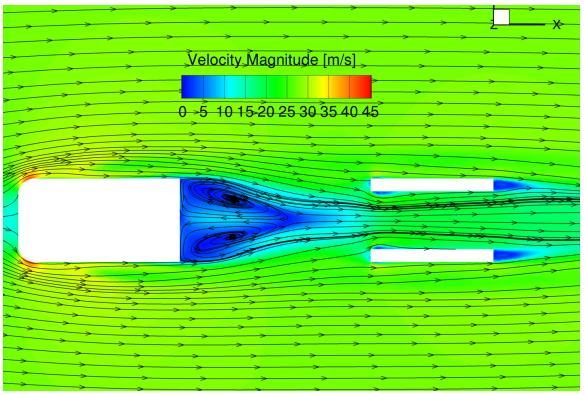

(b) Velocity magnitude contour plot with the X-Y velocity streamlines at the underbody of the S-E baseline model

Figure 3.18: Wake analysis of the S-E baseline model

3.2.2 Crosswind conditions

Crosswind significantly affects the flow field around a driving heavy-duty vehicle and inside the tractor-trailer gap, therefore it is of crucial importance to include crosswind effects into this analysis. To simulate crosswind conditions the boundary conditions of the computation and the applied mesh were adjusted as was described in subsection 3.1.2 and subsection 3.1.5.

When the numerical results for the crosswind conditions were analyzed it was found out that the numerical model had difficulties to solve the problem. For some baseline configurations the convergence history diagram showed very large oscillations when a yaw angle was applied. It was concluded that the RANS model did not find a good solution and therefore the solutions for the crosswind cases are not always fully trustworthy. A more detailed explanation is given in subsection 5.2.2.

Table 3.6 shows the drag contributions for all surfaces of the L-E baseline model for a yaw angle of 0° and 3°. The L-E baseline model was selected for this comparison as the differences between the 0° and 3° yaw angle case are clearly visible for this baseline model. As can be seen in the table, applying crosswind certainly has an effect on the drag coefficient of the entire vehicle. The total drag coefficient increases with 116 drag counts. This is mainly caused by an increase in the drag coefficient of the trailer frontal surface (T_front) of 85 drag counts. As the yaw angle is increased from 0° to 3°, more flow enters the tractor-trailer gap and a larger amount of air impinges on the trailer frontal surface at a higher velocity, which results in a higher drag contribution of the trailer frontal surface. Furthermore the left frontal curved surface of the cabin (C_front_left) generates less suction as this surface is now more orientated in the free stream flow direction. Vice versa, the right frontal curved surface (C_front_right) generates more suction at a yaw angle of 3°.

Table 3.6: Effect of crosswind on the drag contribution of the different parts of the L-E baseline model

Part	$C_{T_{0°yaw}}$	$C_{T_{3°yaw}}$	**Difference**
C_front_front	0.361	0.358	-0.003
C_front_left	-0.118	-0.077	0.041
C_front_right	-0.116	-0.137	-0.021
C_front_bottom	0.027	0.031	0.004
C_front_top	-0.077	-0.077	0
C_left	0.003	0.004	0.001
C_right	0.003	0.002	-0.001
C_bottom	0.004	0.004	0
C_top	0.002	0.002	0
C_back	0.055	0.056	0.001
C_back_back	0.037	0.050	0.013
C_M-E	0	0.001	0.001
C_wheels	0.031	0.031	0
C_SE_left	0	0	0
C_SE_right	0	0	0
C_SE_top	0	0	0
C_SE_back	0.004	0.004	0
Total Cabin	0.216	0.252	0.036
T_front	0.032	0.117	0.085
T_left	0.011	0.014	0.003
T_right	0.011	0.012	0.001
T_bottom	0.002	0.004	0.002
T_top	0.011	0.008	-0.003
T_back	0.135	0.128	-0.007
T_wheels	0.034	0.031	-0.003
Total Trailer	0.234	0.314	0.080
Total Vehicle	0.450	0.566	0.116

Figure 3.19 illustrates the effect of the yaw angle on the drag coefficient of the different baseline models. As can be seen from the figure the drag coefficient increases with increasing yaw angle for all the baseline configurations. However the magnitude of the yaw effect on the drag coefficient greatly depends on the configuration. For the L-E baseline configuration the drag coefficient roughly doubles from 0.45 at 0° yaw angle to 1.00 at 12° yaw angle, while for the S-E configuration the drag coefficient increases from 0.39 to only 0.47. In general the longer the tractor-trailer gap, the larger the drag coefficient increases with increasing yaw angle. The drag coefficient of the ideal NG configuration, which has no gap, is only slightly

influenced by the yaw angle. Furthermore the results of the S-E configuration lie close to the results of this ideal NG configuration.

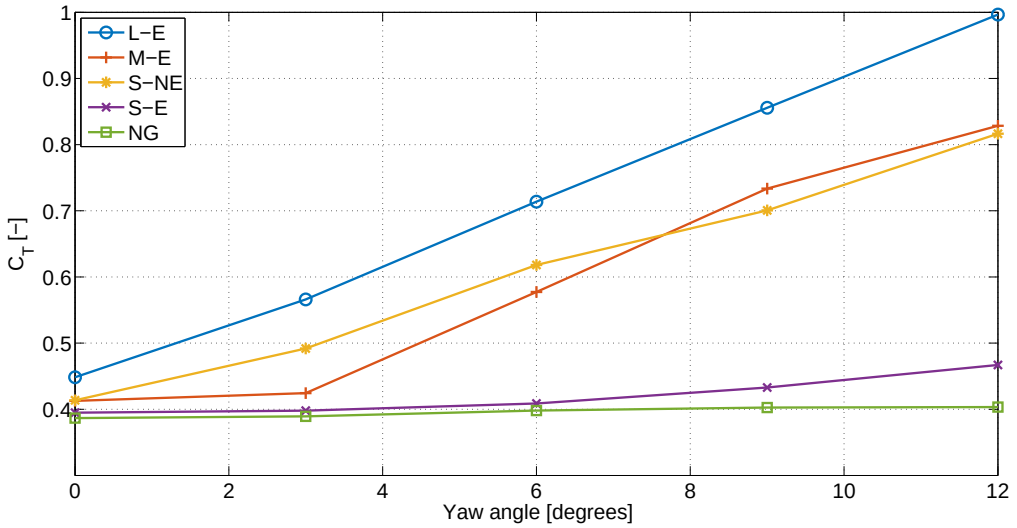

Figure 3.19: Influence of the yaw angle on the drag coefficient for the 5 baseline configurations

Figure 3.20 shows the streamlines including the velocity magnitude around the L-E baseline configuration at a yaw angle of 9°. When one compares this with Figure 3.9 one can clearly see the effect of the crosswind on the flow field. The flow field around the model and inside the gap is not longer quasi-symmetric as was the case in the 0° yaw angle condition. Firstly when the yaw angle was 0° the flow was accelerated at both sides of the cabin up to a velocity of around 45 m/s, but at a yaw angle of 9° the flow is not equally accelerated at both sides of the cabin. At the windward side the flow accelerates to a velocity of only 37 m/s. Secondly a larger amount of air enters the tractor-trailer gap via the windward side compared to the no-crosswind case as can be clearly seen in 3.20(a). There is also still flow coming from the top side of cabin into the gap, but almost no air enters the gap via the leeward side. Thirdly in 3.20(b) a large stream is visible that is going from the windward side of top of the trailer frontal surface to bottom leeward side of the gap and there it exits the tractor-trailer gap.

A contour plot of the Y-velocity at the middle of the gap height is shown in Figure 3.21 to give a better understanding of the flow behavior inside the gap. A large vortex inside the gap is located at the base of the cabin at the windward side. It is interesting to note that there is only one large vortex inside the gap, while there were two quasi-symmetric vortices inside the gap for the no-crosswind case (see 3.14(d)). In Figure 3.21 the strong stream of air flowing from the windward to the leeward side is clearly visible. A large amount of air flows along the windward side of the cabin, bends inwards into the tractor-trailer gap along the large vortex and impinges on the trailer frontal surface. Subsequently some part of the air flows along the trailer frontal surface to the leeward side of the vehicle and then exits the gap, while the other part follows the contours of the vortex and flows diagonally to the base of the cabin (i.e. in the opposite direction of the free stream) and then exits the gap. This general flow structure is present inside the gap of both the L-E and the S-E model, although it is more distinct for the L-E case. The flow structure resembles very well the flow structure that

was experimentally observed by Storms et al. (2006) for the North-American GCM model without extenders (see Figure 1.11). As was described in section 1.4 this PIV experiment was performed at a Reynolds number of $4.8 \cdot 10^6$ based on the width of the vehicle.

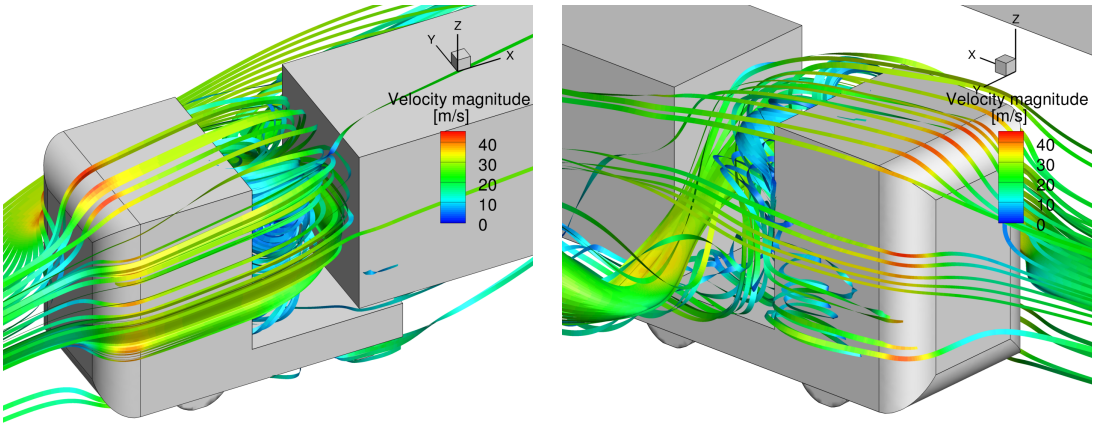

(a) Windward side

(b) Leeward side

Figure 3.20: Streamlines with the velocity magnitude for the L-E baseline configuration at 9° yaw angle

Lastly both in 3.20(b) and in 3.21(a) a region of separated flow is visible at the leeward side of the cabin and a small region of separated flow at the leeward side of the trailer of the L-E baseline model. This is mainly caused due to the large amount of flow coming out of leeward side of the tractor-trailer gap, which pushes the air flowing along the leeward side of the cabin away from the vehicle. Regarding the S-E baseline model no region of separated flow is present at the leeward side of the cabin, there is only a very small region of separated flow on the leeward side of the trailer. Compared with the L-E configuration the amount of air and the velocity of the air in the stream flowing from the windward to the leeward side inside the gap is significantly smaller. This is because less flow enters the tractor-trailer gap. As a consequence there is only a very small region of separated flow at the leeward side of the trailer. This explains why the drag coefficient of the S-E baseline configuration does not increase that much with increasing yaw angle compared to the L-E baseline configuration.

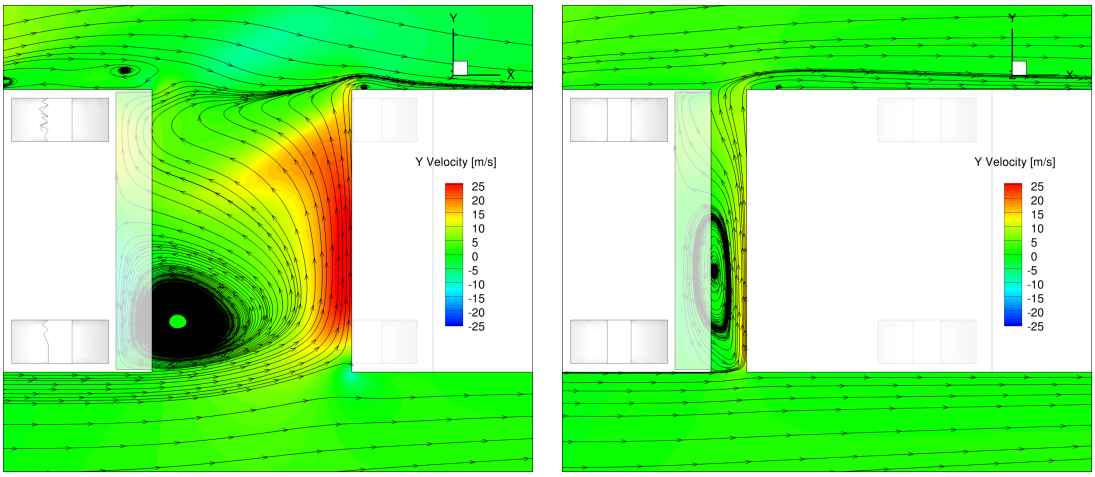

(a) L-E (b) S-E

Figure 3.21: Contour plot of the Y-velocity with arrows indicating the X-Y streamlines at the middle of the gap height at 9° yaw angle

3.2.3 Effect of add-on devices

In order to see the effect of add-on devices on the flow dynamics simulations were executed where baseline configurations were equipped with add-on devices. As was mentioned before in section 2.2 the effect of the add-on devices depends on the yaw angle and is expected to be larger at higher yaw angles. Many of the add-on devices have as goal to reduce the crossflow in the gap which significantly increases with increasing yaw angle. Therefore it is of crucial importance to perform simulation for various yaw angles.

Two different add-on devices were tested during the numerical analysis, namely a splitter plate attached to the trailer frontal surface (SP) and rounded vertical edges of the trailer frontal surface (RE). Only these two add-on devices were tested because they were the only ones which were tested on all the baseline configurations during the wind tunnel experiment. In the numerical analysis these two add-on devices were separately tested on two baseline configurations, namely the S-E and the L-E baseline configuration. Only these two baseline configurations were selected, because performing the simulations was a very time-consuming task and these two baseline configurations represent the extrema of the gap design, namely the smallest and the largest gap length. The results of the simulations can be seen in Figure 3.22 where also the ideal NG case is included.

As can be seen from Figure 3.22 the add-on devices significantly reduce the drag coefficient. However, the drag coefficient reductions obtained by the add-on devices are much bigger for the L-E case than for the S-E case. For example adding a splitter plate to the L-E model reduces the drag coefficient by 339 drag counts (39.6%) at a yaw angle of 9°, but for the S-E model the obtained reduction at this yaw angle is only 1 drag counts (0.2%). This is due to the fact that in the case of the L-E configuration much more crosswind goes through the

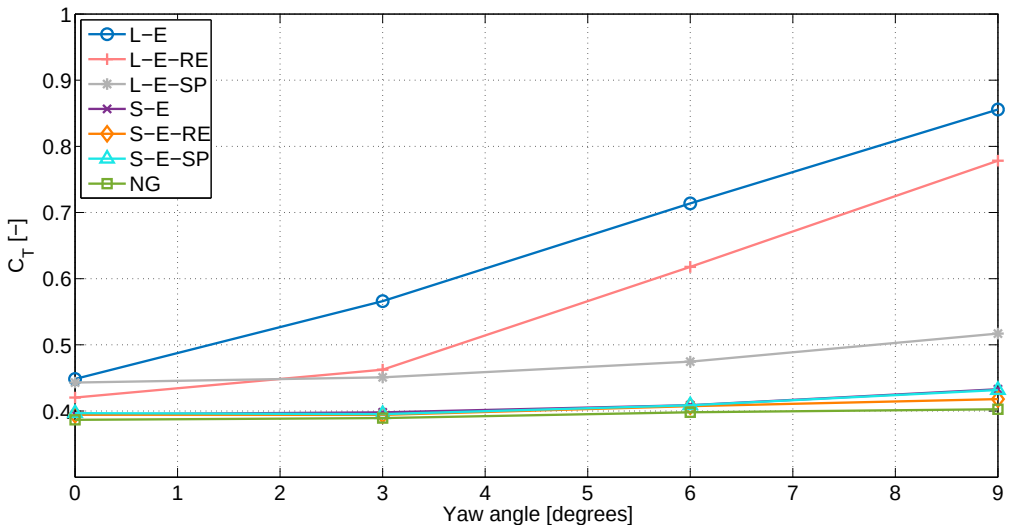

Figure 3.22: Influence of the yaw angle on the drag coefficient for the S-E and the L-E baseline models with add-on devices

tractor-trailer gap compared with the S-E configuration. This large amount of air crossing the gap results in a high drag coefficient, but when a splitter plate is attached the crossflow through the gap is greatly reduced, leading to a reduction in the drag coefficient. However for the S-E configuration a splitter plate does not significantly reduce the crossflow in the gap as there is already not much crossflow. This is clearly visualized in Figure 3.23 where the horizontal streamlines are shown inside the tractor-trailer gap. Furthermore there is a region of separated flow along the leeward side of the cabin and a small region of separated flow along the leeward side of the trailer when the L-E baseline configuration is tested under a yaw angle of 9°. However when a splitter plate is attached to the configuration, these regions of separated flow completely disappear. This is the second reason why adding a splitter plate greatly reduces the drag coefficient of the L-E baseline configuration.

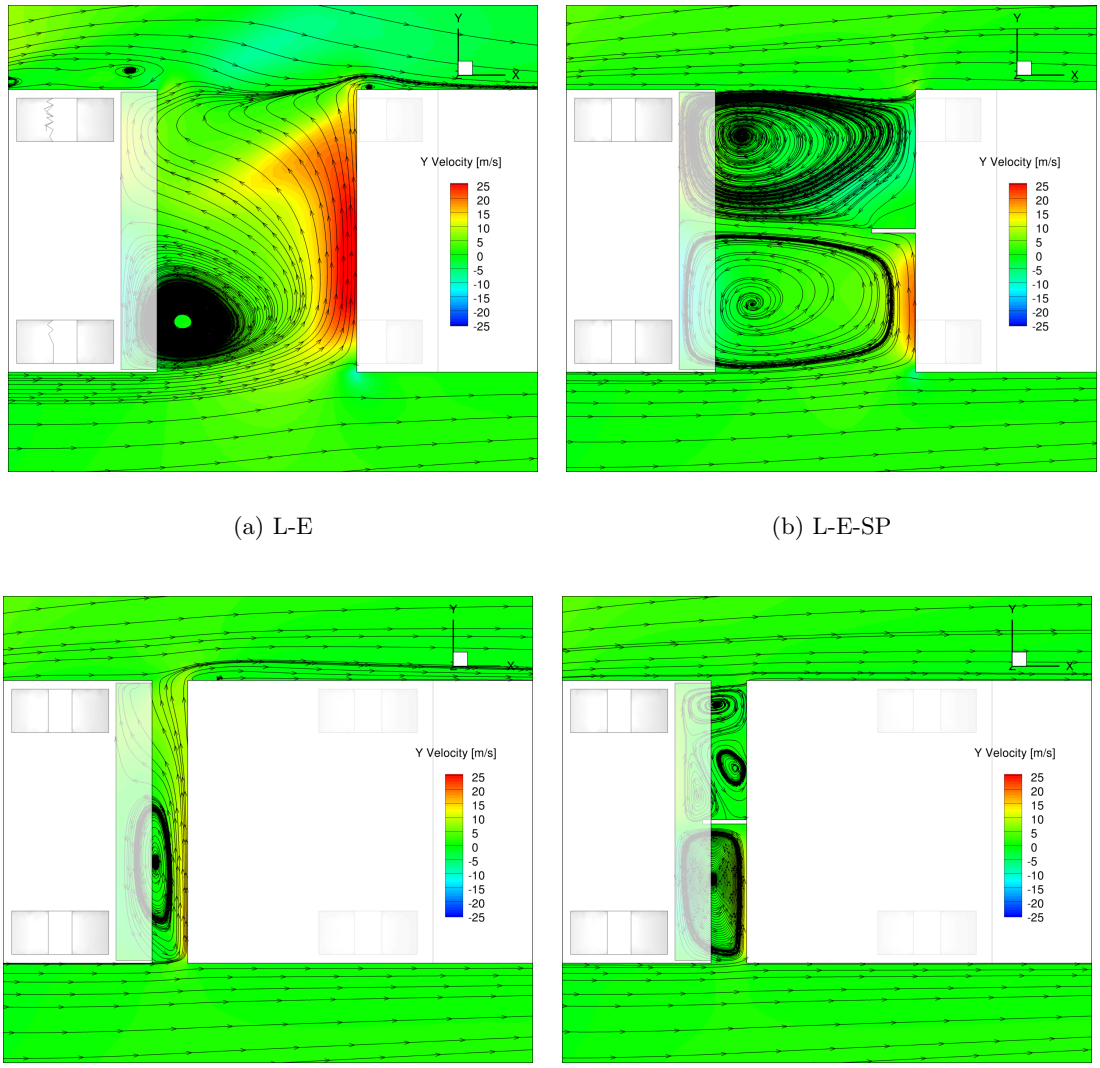

(a) L-E

(b) L-E-SP

(c) S-E

(d) S-E-SP

Figure 3.23: Contour plot of the Y-velocity with arrows indicating the X-Y streamlines at the middle of the gap height at 9° yaw angle

3.2.4 Conclusions regarding the numerical results

The results of the numerical analysis can be summarized as follows.

- At a yaw angle of 0° the tractor-trailer gap is responsible for 15, 42, 40 and 87 drag counts for respectively the S-E, S-NE, M-E and L-E baseline configuration. This means that increasing the gap length leads to a higher drag contribution of the gap.
- When the gap length is increased at a yaw angle of 0°, the drag coefficient of the cabin decreases, while the drag coefficient of the trailer increases significantly, resulting in an

increase for the total vehicle. The cabin drag decreases as the base pressure increases with an increasing gap length. However when the gap length is increased, more air enters the gap and the pressure coefficient on the trailer frontal surface increases. This leads to a higher drag for the trailer.

- It was observed that at a yaw angle of 0° a significant amount of air flowing along the top and sides of the cabin, enter the tractor-trailer gap and subsequently hit the trailer frontal surface. Then two large counter-rotating vortices start to develop inside the gap. The size and the structure of these vortices are very dependent on the geometry of the gap. For the L-E baseline model the two vortices are stretched along the longitudinal axis of the vehicle, while the vortices of the S-E and the S-NE baseline model are stretched along the width of the vehicle. Furthermore in general the flow inside the gap flows from the top to the bottom of the gap.

- The length of the gap and the presence of side and roof extenders clearly influence the pressure coefficient on the trailer frontal surface. For the S-E baseline model the average pressure coefficient on the trailer frontal surface at a yaw angle of 0° equals -0.186, while for the L-E baseline model this value is equal to 0.041. When the side and roof extenders are detached from the cabin the average pressure coefficient increases to -0.153.

- The length and the presence of side and roof extenders also slightly affects the wake of the heavy-duty vehicle and the drag contribution of the trailer base surface. The larger the gap length, the larger the drag coefficient of the trailer base surface.

- When a yaw angle is applied a larger amount of air enters the tractor-trailer gap and impinges on the trailer frontal surface, hereby increasing the pressure coefficient on this surface and increasing the drag coefficient of the entire vehicle. The increase of the drag coefficient due to an increase in yaw angle is very dependent on the length of the gap and the presence of extenders. When the gap length is large or when no extenders are present, the increase in drag coefficient is much bigger.

- When a yaw angle is applied the flow field inside the gap can show one large vortex instead of two large counter-rotating vortices for the 0° yaw angle case. Furthermore when the yaw angle is large enough (the threshold depends on the baseline model), flow separation occurs at the leeward side of the vehicle.

- Adding a splitter plate or a rounded edges add-on device greatly reduces the drag coefficient of the L-E model, especially for large yaw angles. At a yaw angle of 9° the drag reduction obtained by adding the splitter plate add-on device goes up to 339 drag counts (39.6%). The effect of these add-on devices on the drag coefficient of the S-E model is significantly less, even negligibly small. For example the maximum obtained drag reduction with the splitter plate add-on device is smaller than 1%.

Chapter 4

Experimental Analysis

The second analysis method is a wind tunnel experiment performed in the Open Jet Facility (OJF) of the TU Delft. The main goal of the experimental analysis is to validate the numerical results. As the applied numerical method contains several assumptions it is important to check if the simulations are correctly simulating the flow dynamics. The second goal of the experimental campaign is to analyze a larger amount of add-on devices.

First the set-up of the experimental analysis will be explained in section 4.1, subsequently the results will be discussed in section 4.2. Finally in chapter 5 the experimental results will be compared with the numerical results in order to validate the numerical analysis.

4.1 Set-up of the experimental analysis

The wind tunnels at the TU Delft are in high demand and therefore the time in the wind tunnel is limited and one has to reserve the tunnel months in advance. For this study two weeks were available in the OJF to perform all the measurements. A good preparation is of crucial importance since one wants to use the time in the tunnel as useful as possible. This preparation can easily take multiple weeks. After the wind tunnel experiment all the obtained data have to be post-processed and analyzed, which also requires an additional period of several weeks. This section will describe the steps which were taken needed to conduct the wind tunnel experiment including the preparations and the post-processing.

4.1.1 Design and production of the wind tunnel model

Design of the model

The geometry of the model that had to be built for the wind tunnel experiment is described in section 2.1, a technical drawing can be seen in Figure A.1. The surface model was based on real heavy-duty vehicles driving on the road in Europe and also based on the GETS model. It was made sure that the surface model used in the numerical simulations matched as much as possible the surface model that was used in the wind tunnel experiment.

Production of the model

The production of the wind tunnel model was a very time-consuming process since the complete model had to be built from scratch. The production process started in the beginning of February 2016 with the structural design of the model and ended just before the wind tunnel experiment in the beginning of April 2016.

In an early stage of the production process it was decided that the model should be reusable for future experiments in the field of heavy-duty vehicle aerodynamics. Making the model reusable is a more sustainable option than making a new wind tunnel model for every new experiment. However this lead to the criteria that the model should be easily adaptable to slightly different configurations. Another criteria was that the model should be lightweight, more specifically lighter than 35 kg. This is because the balance system can withstand a maximum load of 500 N in the vertical direction. Subtracting the weight of the turning disk ($\approx 12\ kg$), potential aerodynamic downforce ($\approx 1.5\ kg$) and some margin ($\approx 2.5\ kg$), you get a maximum weight of the model of 35 kg. The potential downforce was roughly estimated with some preliminary CFD simulations in Fluent. The last criteria was that the model should be strong and stiff enough to withstand the aerodynamic forces without vibrating or bending. The maximum deflection of the turning disk was roughly calculated with the use of the basic beam deflection formulas and determined to be less than 4 mm.

The answer to all these criteria was a design which consisted out of an aluminum frame covered by thin wooden plates. The aluminum frame provided enough structural stiffness, while the wooden plates gave the model the desired shape. 4.1(a) and 4.1(b) show how respectively the tractor and the trailer of the wind tunnel model were built out of an aluminum frame and wooden plates as cover.

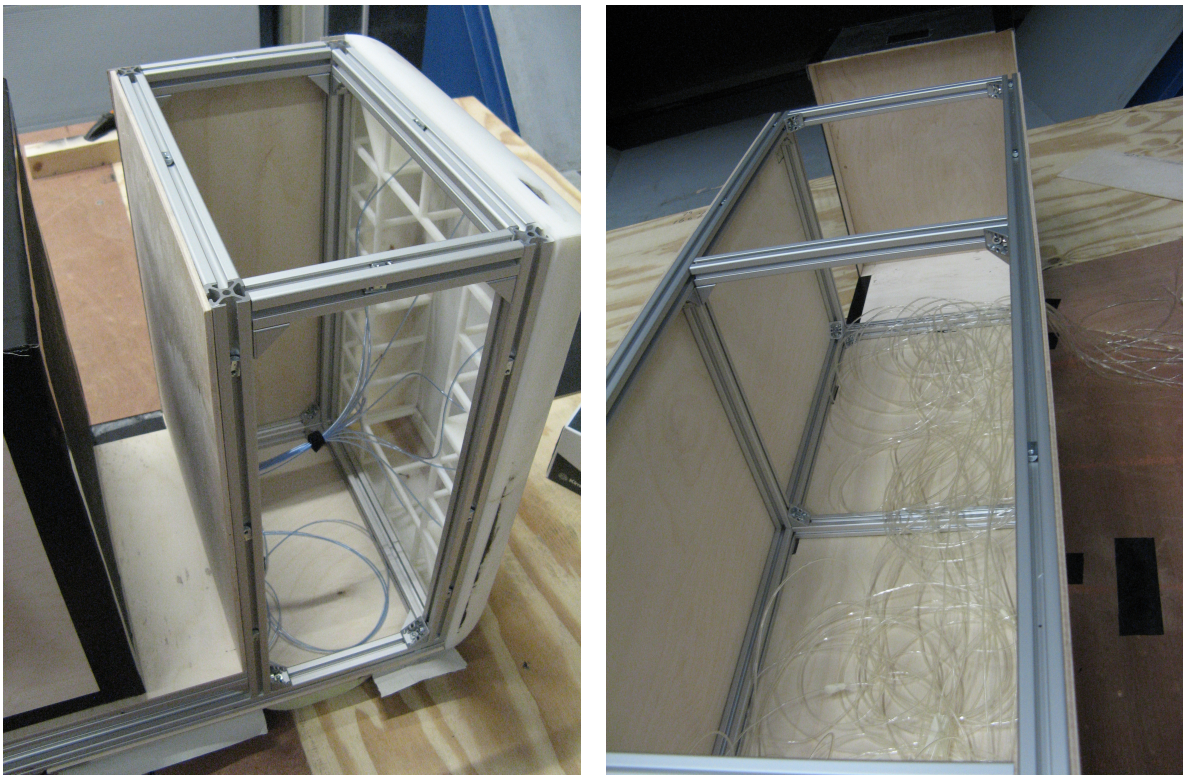

(a) The tractor of the wind tunnel model

(b) The trailer of the wind tunnel model

Figure 4.1: Structure of the wind tunnel model

The aluminum frame consists out of several construction profile beams of 20 by 20 mm in cross section. These beams were connected to each other by specific corner brackets and to the wooden plates by T-slot nuts. The frame can be dissembled and new configurations of the heavy-duty vehicle can be easily made with this system. The wooden plates can be interchanged during the wind tunnel experiment to test multiple different configurations. For example two different types of side panels for the tractor were made: one type with side extenders and the other one without side extenders. By detaching the wooden side panels with screws from the frame and replacing them with the other type of side panels, one can easily test the impact of extenders on the drag coefficient of the vehicle.

The wheels, the front part of the tractor and some of the add-on devices have large curved surfaces and therefore it was opted to produce them differently. The wheels and most of the add-on devices were made out of polystyrene foam (Styrodur). The foam is very light and easy to shape in the desired dimensions. The hot-wire cutter, located at the fluid mechanics department of mechanical engineering, was used to cut the parts after which they were sandpapered by hand to obtain smooth surfaces. Some other add-on devices were made out of off-the-shelf PVC products. Lastly the front part of the tractor was 3D-printed and then sandpapered. All these parts were fixed to the model by means of double sided tape.

At the end all the edges and junctions of the model were covered with tape to get smooth rounded edges and surfaces. Small gaps in between the wooden panels and all the screws were covered with tape to prevent that they would cause flow separation. Due to imperfections during the production of the model there was a small jump in height between the 3D-printed front part of the tractor and the rest of the tractor. This was solved by applying some clay at this jump resulting in a smooth transition between the 3D-printed part and the wooden panels.

During the wind tunnel experiment one wants to have attached turbulent flow along the test model in the no-crosswind condition, because this matches the real-life road conditions. In the beginning of the wind tunnel campaign a microphone was used to determine if the boundary layer was indeed turbulent and attached. Small separation bubbles were observed with the use of the microphone just behind the front curvatures of the cabin. To eliminate these separation bubbles zigzag tape was glued to the frontal surface of the cabin. At the end 3 layers of 0.65 mm thick zigzag tape were needed to make sure that the boundary layer was tripped.

4.1.2 The Open Jet Facility

The wind tunnel experiment was carried out in the Open Jet Facility (OJF) of the TU Delft. A schematic overview of the wind tunnel is shown in Figure 4.2. The octagonal open test section is 2.85 m wide and 2.85 m high (TU Delft (2015)). The maximum test velocity of the wind tunnel is around 30 m/s and at this velocity the turbulence intensity is approximately 0.3 %. However in the beginning of the experimental campaign it was found out that in practice the maximum velocity of the wind tunnel is limited to a value of around 27.2 m/s due to vibrations in the rotor beyond this velocity. Therefore it was opted to perform all tests at a velocity of approximately 27.2 m/s, which leads to a Reynolds number of $849,000$ based on the square root of the cross-sectional area of the test model. The value of the Reynolds number is comparable to a Reynolds number of $826,400$ at which Van Raemdonck and Van Tooren (2008) tested the GETS model. The sensitivity of results with respect to the Reynolds number will be discussed in more detail in subsection 4.2.1.

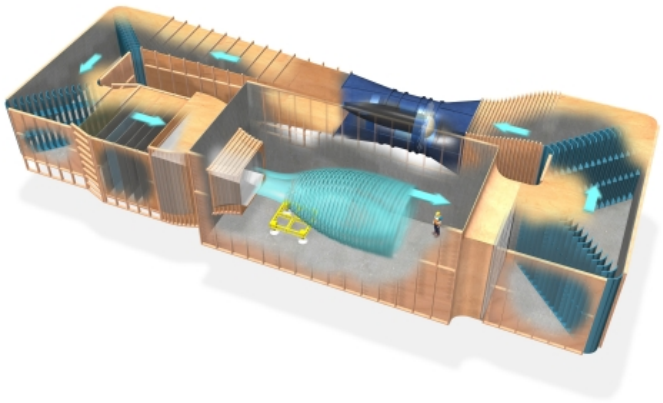

Figure 4.2: A schematic overview of the OJF with the test section in the middle of the bottom of the figure (TU Delft (2015))

4.1.3 Measurement techniques

Force and moment measurements

There is no integrated balance system in the OJF to measure the forces and the moments acting on the model, however NLR developed an external 6-component balance system which can be used in the OJF (Alons (2008)). The maximal load the balance can withstand when all components are loaded simultaneously can be seen in Table 4.1. During the preparations of the test campaign it was checked with the use of the numerical simulations that the loads on the balance would not exceed these limits.

Table 4.1: Maximum allowable loads of the balance system (Alons (2008))

Force component		Moment component	
Axial force	± 250 N	Rolling moment	± 500 Nm
Side force	± 500 N	Pitching moment	± 250 Nm
Vertical force	± 500 N	Yawing moment	± 50 Nm

The maximum error of the balance is for all the components less than 0.25% and for the force component in x-direction only 0.06% (Alons (2008)). The balance has a measurement frequency of 2000 Hz. It was decided to average the measured data over a measuring time of 60 s for each measurement. Figure 4.3 shows the drag force averaged over the measuring time versus the measuring time. As can be seen from the figure it takes at least 45 s before the mean value converged to a certain steady value. A margin of 15 s was added to be sure that the mean value was converged for all tested configurations.

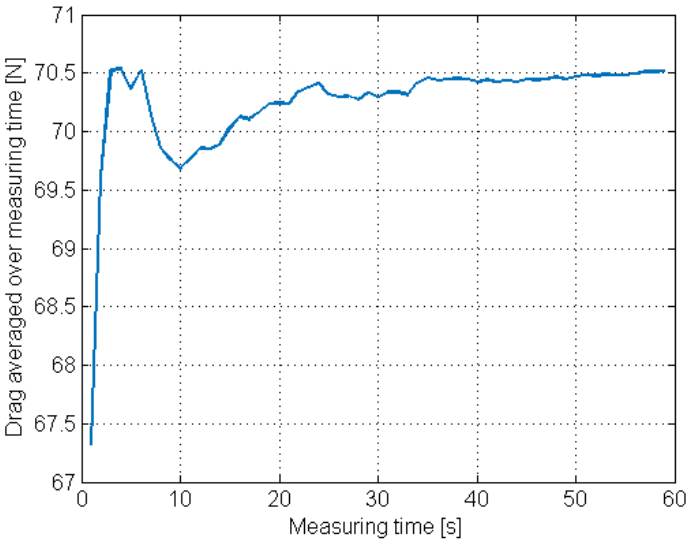

Figure 4.3: The average measured drag force (in the driving direction of the vehicle) versus the measuring time for the L-E baseline model at a yaw angle of 12°

Varying the yaw angle

As the yaw angle significantly affects the drag coefficient, one wants to test the different configurations under varying yaw angles. A turning device was developed which is compatible with the balance system, however the combination of the two devices has never been tested on this scale. The turning device has an accuracy of 1°, which lead to a small misalignment of the model of less than 1°. The turning device can be attached to the OJF table and rotates the balance system, a part of the wooden ground platform (called the turning disk) and the model itself. A rendering of the complete test set-up is shown in Figure 4.4. Around this set-up the rest of the ground platform was constructed. The platform itself was already available, but the supporting structure carrying the platform still had to be made. This supporting structure consisted out of wooden beams and metal corner brackets. During the wind tunnel campaign it was found out that the supporting structure was not very stable and had to be repaired multiple times. This reduced the time for testing and limited the amount of add-on devices that could be tested. An overview of the complete test set-up, including the dimensions of the ground platform, is shown in section A.3.

Pressure measurements

Besides the balance measurements also static pressure measurements were performed during the wind tunnel experiment. The main goal of these pressure measurements was validation for the CFD results. Next to that they can also give more insight into the flow field around the heavy-duty vehicle model. To acquire the pressure data the Barocell pressure measurement device was used in combination with a scanivalve. This system automatically switches from one pressure tab to the next one, but it can only measure one pressure tab at a time. As this leads to a long total measurement time, it was decided to only measure the pressure at 18

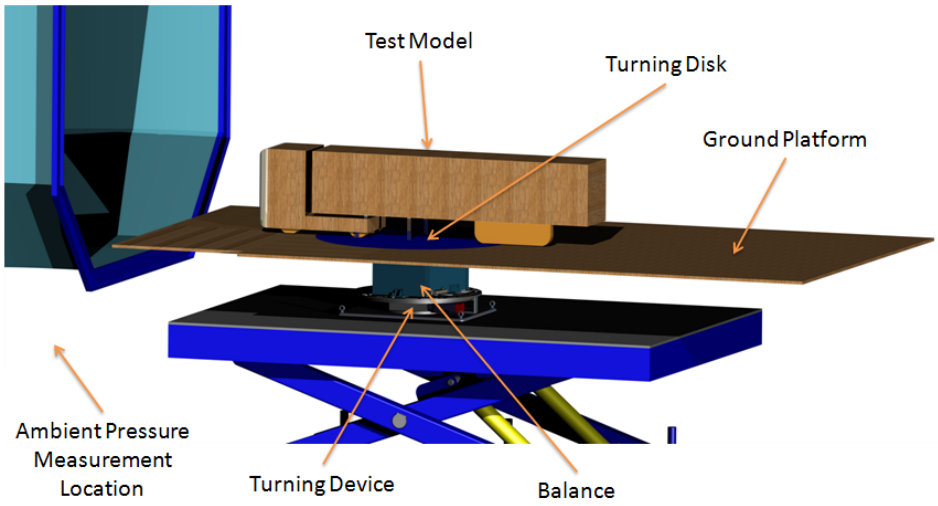

Figure 4.4: The test set-up with from the bottom to the top: the turning device, the balance system, the turning disk & the ground platform and the model

pressure tabs. These pressure tabs were distributed over two parts, namely the front surface of the trailer and the curved front surface of the cabin (Figure 4.5). The exact locations of the pressure tabs can be found in section A.2.

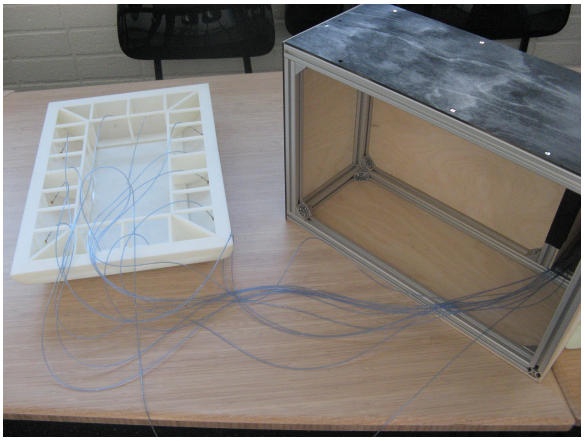

(a) The 3D-printed front part of the tractor with the pressure tabs

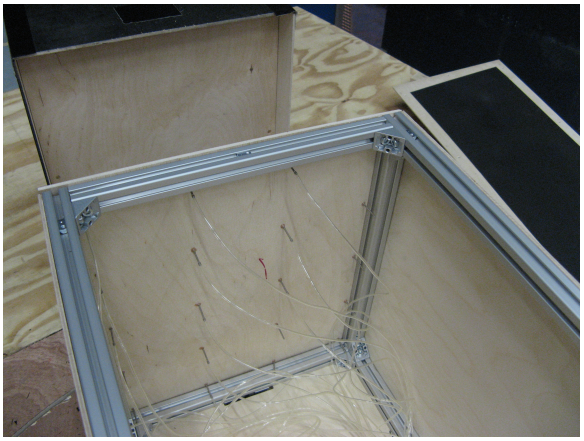

(b) The front part of the trailer with the pressure tabs

Figure 4.5: Location of the pressure tabs on the model

The pressure tabs were connected via thin silicone tubes to the scanivalve and the Barocell. However as the scanivalve and the Barocell had to be placed outside of the wind, they were placed underneath the ground platform. Therefore the pressure tubes were more than 4 m long as they had to go through the test model and through the turning disk (see 4.5(a)). Since the pressure holes were very thin and the tubes very long, it took approximately 6 s for the pressure to settle to a converged value. Therefore it was opted to apply a delay time

of 6 s before starting measuring at each pressure tab. It was also investigated how long the measurement should take for each pressure tab, after a short sensitivity analysis it was opted to select a measurement time of 30 s.

The Barocell pressure measurement device measures the difference between the pressure at the pressure tab and the ambient pressure. The ambient pressure was measured inside the wind tunnel test section underneath the nozzle of the OJF. It was assumed that this pressure is equal to the free stream pressure. With Equation 4.1 the pressure coefficient can be computed.

$$C_p = \frac{p - p_\infty}{0.5\rho V^2} \tag{4.1}$$

Flow visualization

It was decided to not only measure the pressure and the forces, but also to perform some flow visualization. Two different methods of flow visualization were applied, namely smoke and tuft. Flow visualization gives the researcher some qualitative information about the flow dynamics. A plume of smoke or a tuft can quickly tell if the flow is separated or still attached. Besides smoke and tuft, use was also made of a microphone to investigate if the flow is laminar, turbulent or separated.

4.1.4 Post-processing the wind tunnel data

Correcting for the turning disk

As was pointed out in section 4.1.3 the test model with the turning disk is attached to the balance. This means that the balance is not only measuring the aerodynamic forces and moments acting on the test model, but also the aerodynamic forces and moments acting on the turning disk. At the end of the test campaign the test model was removed from the turning disk and measurements were performed with just the turning disk. In this way the aerodynamic forces and moments acting on the turning disk could be determined. Afterwards these forces and moments could be subtracted from the measured data to obtain solely the aerodynamic forces and moments acting on the test model. A small drawback of this method is that the interference effects between the model and the turning disk are neglected. However as was explained by SAE (2012) no simple correction methods can be derived to account for these interference effects.

Wind tunnel corrections

The presence of the test model and the wind tunnel itself affects the flow dynamics, so the obtained data have to be corrected for this. There are specific correction factors for automotive test models in open-jet wind tunnels, which are extensively discussed in AGARDograph 336 Wind Tunnel Wall Correction (Ewald (1998)). Although the ground plate was placed slightly

higher than the jet exit of the OJF, for this correction method it was assumed that the ground plate was placed at the same height as the jet exit. The first correction factor that has to be applied is due to the interference effect of the test model on the the wind tunnel nozzle. When the test model is placed closely to the nozzle of the OJF, the velocity of the flow leaving the nozzle of the wind tunnel will increase (Ewald (1998)). The measured data have to be corrected for this by applying the following formulas.

First the nozzle blockage correction factor at nozzle itself has to be calculated with the following equation (Ewald (1998)).

$$\epsilon_{qn} = \frac{\left(\frac{S}{2C}\right)\left(1 + \frac{x_s}{\sqrt{x_s^2+R_n^2}}\right)}{1 - \left(\frac{S}{2C}\right)\left(1 + \frac{x_s}{\sqrt{x_s^2+R_n^2}}\right)} \tag{4.2}$$

When the effect of the test model on the nozzle is know, one can compute the nozzle blockage correction factor at the location of the test model with Equation 4.3 (Ewald (1998)).

$$\epsilon_n = \epsilon_{qn}\left(\frac{R_n^3}{(x_m^2 + R_n^2)^{3/2}}\right) \tag{4.3}$$

Another perturbation occurring during wind tunnel experiments in open-jet test sections is solid blockage. Due to the presence of the test model the flow exiting the nozzle has to go around the model, increasing the exiting flow angle of the flow coming from the nozzle and causing over-expansion of the flow (Ewald (1998)). A simple formula was developed to account for this solid blockage (see Equation 4.4 (Ewald (1998))).

$$\epsilon_s = \tau\left(\frac{V}{L}\right)^{1/2}\left(\frac{S}{C_e^{3/2}}\right) \tag{4.4}$$

To determine the effective nozzle area C_e one can use Equation 4.5.

$$C_e = \frac{C}{1 + \epsilon_{qn}} \tag{4.5}$$

Finally one can also determine the collector blockage effect, but it was assumed that this collector blockage effect would be negligibly small as the collector of the OJF was located significantly behind the test model.

Now that all the correction factors are known, they can be summed to determine the correction to the measured velocity. Equation 4.6 shows how the measured velocity has to be adjusted to account for all the blockage effects. For this wind tunnel experiment the measured velocity had to be multiplied with 1.0055 to account for all the blockage effects.

$$\begin{aligned} \frac{U_c}{U_m} &= 1 + \epsilon_s + \epsilon_n \\ &= 1.0055 \end{aligned} \tag{4.6}$$

Wind averaged drag coefficient

As was mentioned earlier the yaw angle of the heavy-duty vehicle will be varied to see what the effect is of the yaw angle on the drag coefficient. SAE came up with the concept of a wind averaged drag coefficient such that the drag coefficient for multiple yaw angles of a certain automotive model can be put into one number. The wind averaged drag coefficient acts thus as a mean value for the drag coefficient. It is a very useful parameter for a comparative study like this thesis.

The wind averaged drag coefficient depends on the vehicle speed, the wind speed and the wind direction distribution. The speed of the heavy-duty vehicle was assumed to be 85 km/h which is the normal operating velocity of European heavy-duty vehicles on the highway. For the wind speed the same value of 14 km/h was applied as in the research of Buijs (2010), which was based on the averaged wind speed of locations in Northwestern Europe. Finally it was assumed that the wind direction distribution is uniform.

The complete derivation of the wind averaged drag coefficient can be found in SAE Wind Tunnel Test Procedure for Trucks and Buses (J1252) (SAE (2012)), for this research the formula used by Van Raemdonck (2012) is applied (see Equation 4.7).

$$\bar{C}_T(V_T) = \frac{1}{n \cdot \bar{M}} \sum_{j=1}^{n} M(j) C_T(j) \tag{4.7}$$

The formulas to determine M can be found in literature, more specifically in SAE (2012) and Van Raemdonck (2012).

4.2 Experimenal results

4.2.1 Reynolds number effects

The test velocity in the OJF is limited to a maximum of 27.2 m/s and due to practical constraints a test model of scale 1:8 was used. This results in a Reynolds number based on the square root of the cross-sectional area of $8.5 \cdot 10^5$. In real-life road conditions the Reynolds number of a European heavy-duty vehicle driving on the highway is around $5 \cdot 10^6$. To check if this difference in Reynolds number has a large effect on the obtained data, a Reynolds sweep was performed. The results of this Reynolds sweep can be seen in Figure 4.6.

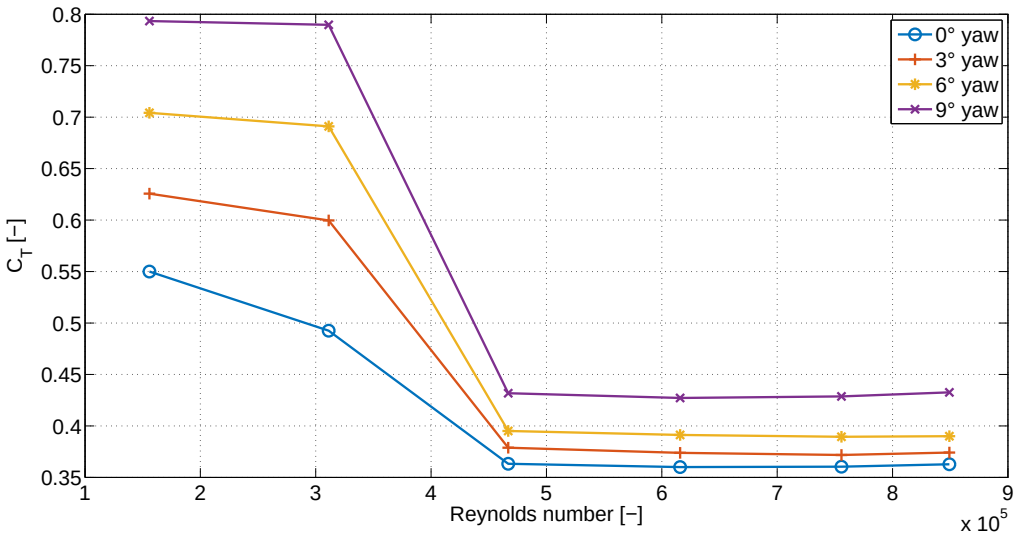

Figure 4.6: Reynolds sweep, the effect of the Reynolds number on the drag coefficient

Figure 4.6 shows that the drag coefficient stays relatively constant for Reynolds numbers larger than $4.7 \cdot 10^5$. So the Reynolds number effects are minimal for all the performed tests. A similar pattern for the Reynolds sweep was found by Van Raemdonck (2012) for the GETS model. As the test model used in this study is based on the GETS model, it is logical that the Reynolds number behavior is also similar.

4.2.2 The baseline configurations

As was explained before there are five different baseline configurations in this study, namely L-E, M-E, NG, S-E and S-NE. The first four have the same geometry except that the gap length is different. These configurations have a cabin equipped with side and roof extenders. The fifth baseline configuration, S-NE, is exactly the same as the S-E configuration except that S-NE model is not equipped with side and roof extenders. To analyze the impact of the gap length and the presence of the extenders on the drag coefficient, the five baseline configurations were plotted together in one graph (see Figure 4.7).

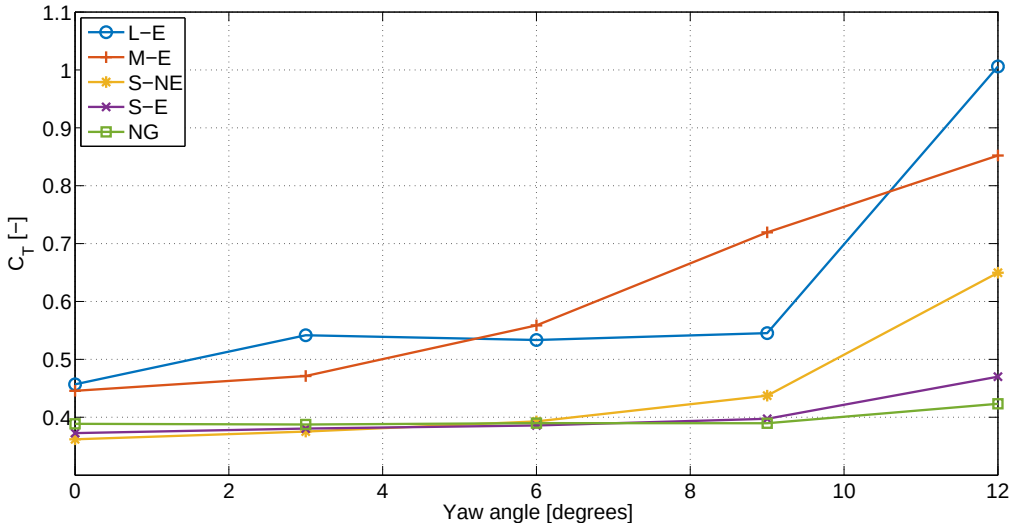

Figure 4.7: Influence of the yaw angle on the drag coefficient of the five baseline models

As can be seen in Figure 4.7 the gap length significantly influences the drag coefficient. If there is no tractor-trailer gap (NG model), the drag coefficient only increases slightly with increasing yaw angle. The configurations with a gap experience a large drag force increase when the yaw angle is increased. From Figure 4.7 one can also notice that in general the bigger the tractor-trailer gap length, the higher the drag coefficient. However this is not always true, as the M-E configuration has a larger drag coefficient compared to the L-E configuration at a yaw angle of 6° and 9°. The hypothesis is that it is because for the L-E baseline configuration a significant part of the wake of the cabin fits in the tractor-trailer gap and several streamlines hit the trailer frontal surface closer to the symmetry plane of the vehicle compared to the M-E baseline model. When crosswind is applied the streamlines, hitting the trailer frontal surface, move more to the leeward side of the gap. For the L-E baseline model the streamlines hit the trailer frontal surface closer to the symmetry plane of the vehicle compared to the M-E baseline model. As a result the L-E baseline model can cope more easily with the leeward movement of the streamlines without having separation at the leeward side of the vehicle. Hammache and Browand (2004) also observed that in a range of specific gap lengths a configuration with a smaller gap length can have a higher drag coefficient than a configuration with a larger gap length, especially at yaw angles above 6°.

Furthermore it is interesting to note that the values of the S-E configuration lie close to the values of the NG configuration, only at yaw angle of 12° there is a noticeable difference of 47 drag counts. This means that the S-E configuration performs almost as good as the ideal case where there is no gap. Finally it can be observed that the side and roof extenders significantly reduce the drag coefficient when the yaw angle is large (9° and 12°). The drag reduction obtained by adding the side and roof extenders is even 179 drag counts at a yaw angle of 12° and 40 drag counts at a yaw angle of 9°.

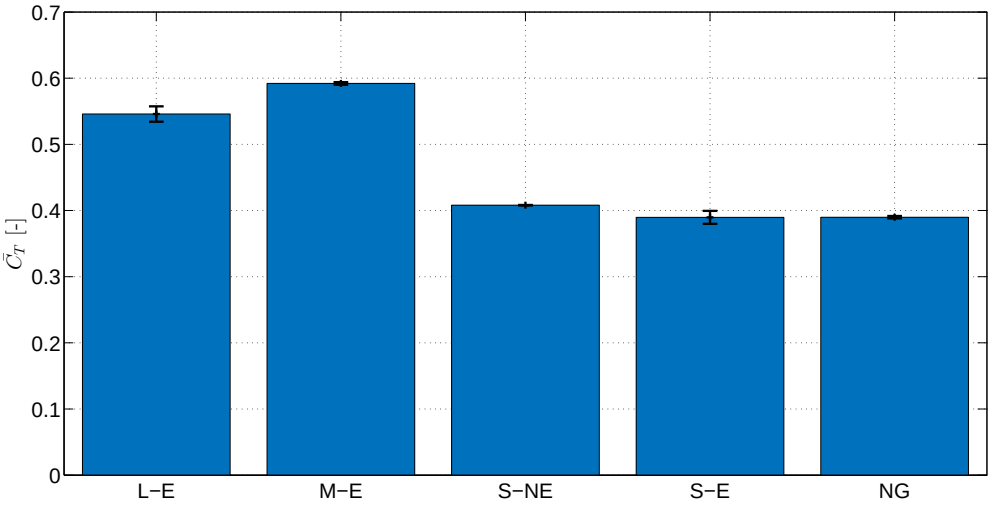

Figure 4.8: Wind averaged drag coefficient of the different baseline models

An overview of the wind averaged drag coefficient of the different baseline models can be seen in Figure 4.8. The graph also contains error bars which indicate the 68% confidence intervals. Also the other bar charts in this chapter contain the 68% confidence intervals. More information about these confidence intervals and the sensitivity of the results can be found in subsection 4.2.6. The wind averaged drag coefficients of the S-NE, S-E and NG baseline model, respectively 0.408, 0.390 and again 0.390, are significantly lower than the wind averaged drag coefficients of the L-E and the M-E baseline model, respectively 0.546 and 0.592. The difference in wind averaged drag coefficient between the S-NE, S-E and NG baseline model is very small, because the wind averaged drag coefficient is mainly dependent on the drag coefficients at a yaw angle between 3° and 9° and the biggest difference between these three baseline models is only visible at a yaw angle of 12°. For the same reason the wind averaged drag coefficient of the M-E baseline model is larger than the wind averaged drag coefficient of the L-E model. As was explained in the previous paragraph the M-E model has a larger drag coefficient than the L-E model at a yaw angle of 6° and 9°. This is the cause of the higher wind averaged drag coefficient of the M-E model.

4.2.3 Effect of add-on devices

Effectiveness versus gap length

Multiple different add-on devices were on the L-E, M-E, S-E and the S-NE baseline configuration to see their influence on the drag coefficient. No add-on device was attached to the NG baseline model as this model has no tractor-trailer gap. Three different add-on devices were applied on all the mentioned baseline configurations, namely the splitter plate (SP), rounded edges (RE) and cooling unit (CO), except for the cooling unit add-on device which was not tested on the M-E model. So the effectiveness of these add-on devices can be evaluated for three different tractor-trailer gap lengths. In Figure 4.9 the wind averaged drag coefficient

is plotted as a function of the normalized gap length for the SP, RE, CO and no add-on device case. In general the wind averaged drag coefficient increases with the normalized gap length. The only exception is the L-E baseline model, which has lower drag coefficient values compared to the M-E baseline model at 6° and 9° yaw angle, as was explained in the previous section. The wind averaged drag coefficient also increases with the gap length if the heavy-duty vehicle is equipped with add-on devices, but then the increase is significantly lower compared to the no-add-on device case. Figure 4.9 shows that for a small normalized gap length of 0.209 the effect of an add-on device on the wind averaged drag coefficient is negligibly small. Furthermore the drag coefficient of the heavy-duty vehicle equipped with the RE add-on device increases significantly when the normalized gap length is increased between 0.483 and 0.688. At a normalized gap length of 0.688 (L-E model), the drag coefficient of the RE configuration is even higher than the configuration without any add-on device. The reason of this large drag coefficient will be explained in the following subsection. Finally it can be seen from the same graph that the splitter plate configuration has the smallest wind averaged drag coefficient for all the tested gap lengths.

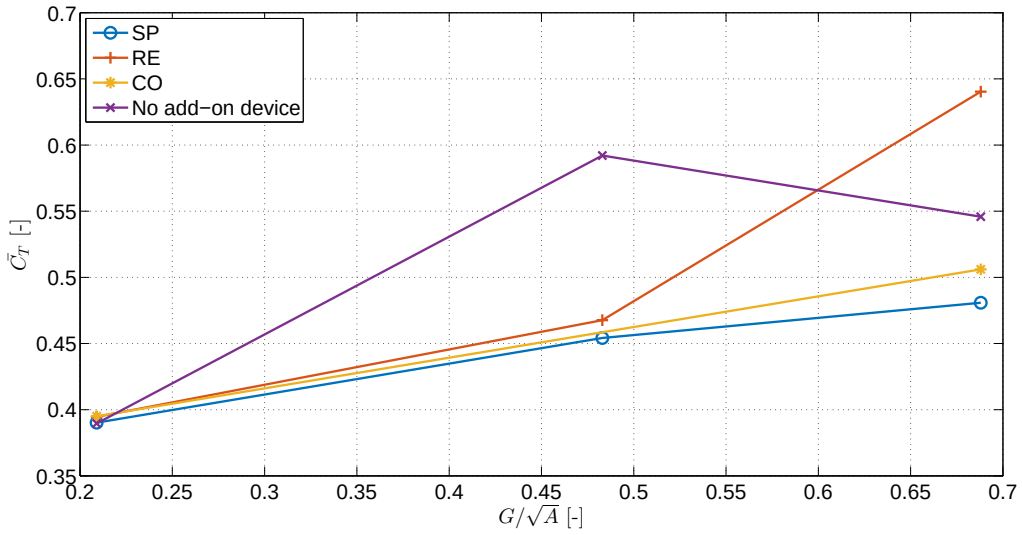

Figure 4.9: Influence of the normalized gap length on the wind averaged drag coefficient for multiple add-on devices

As the effectiveness of add-on devices as a function of the normalized gap length is analyzed, the different baseline configurations equipped with multiple different add-on devices will be discussed in more detail.

L-E baseline configuration

Figure 4.10 shows the drag coefficient as a function of the yaw angle for the L-E baseline configuration equipped with different add-on devices. The add-on devices clearly affect the drag coefficient of the vehicle, especially if the yaw angle is 12°. The splitter plate for example reduces the drag coefficient with 20 drag counts (4.4%) when the yaw angle is 0°, but the obtained drag reduction increases up to 235 drag counts (23.3%) when the yaw angle equals 12°. Regarding the cooling unit add-on device, the drag reduction at a yaw angle of 0° is in

the same order of magnitude as the splitter plate, namely 26 drag counts (5.6%). At a yaw angle of 12° the cooling unit is significantly less effective than the splitter plate, as it only reduces the drag coefficient with 108 drag counts (10.8%).

All add-on devices reduce the drag coefficient for every yaw angle, with the exception of the rounded edges add-on device (6° and 9° yaw angle) and the horizontal cylinders (0° yaw angle). The latter one is probably due to a slight misalignment of the add-on device during the experiment. The L-E configuration equipped with the RE add-on device has a significantly higher drag coefficient at 6° yaw angle (105 drag counts) and at 9° yaw angle (223 drag counts) than the baseline L-E configuration. The hypothesis is that this is probably because of the same reason why the M-E baseline configuration had a larger drag coefficient than the L-E baseline configuration at a yaw angle of 6° and 9°. The RE add-on device significantly decreases the gap length and hereby the streamlines hitting the trailer frontal surface move more outward. When a yaw angle of 6° or 9° is applied the streamlines on the leeward side of the cabin do not enter the gap anymore and the flow separates along the leeward side of the vehicle. This leads to a higher drag coefficient for the L-E-RE configuration compared to the L-E baseline configuration at a yaw angle of 6° and 9°.

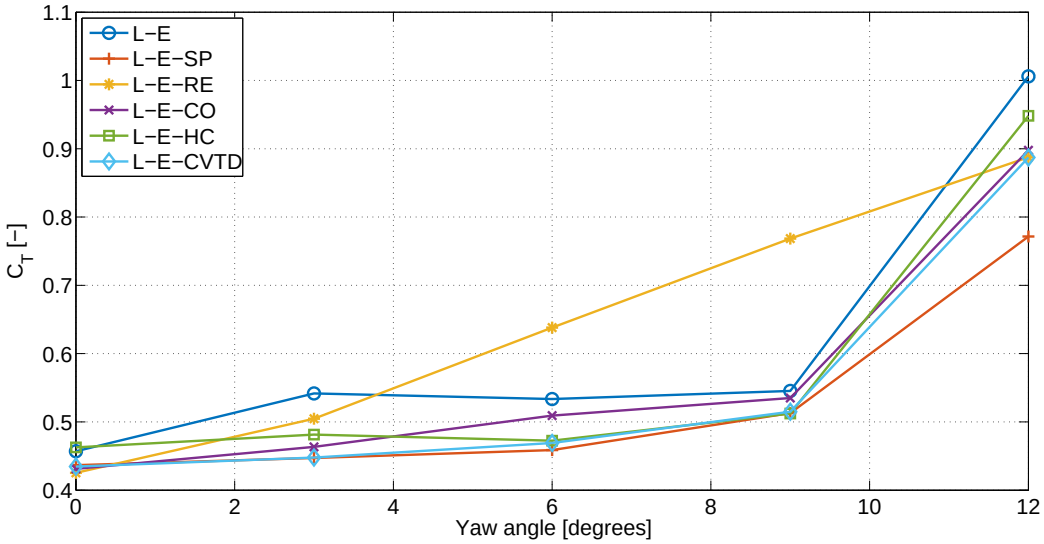

Figure 4.10: Influence of the yaw angle on the drag coefficient for the L-E baseline configuration with add-on devices

In Figure 4.11 the differences between the wind averaged drag coefficient of all the add-on device configurations compared to the L-E baseline configuration are displayed. As can be seen from the graph, the splitter plate is the most effective add-on device with a wind averaged drag coefficient reduction of 65 drag counts (11.9%), closely followed by the cross vortex trap device (CVTD) with a drag reduction of 59 drag counts (10.8%). The cooling unit and the horizontal cylinders cause a reduction in wind averaged drag coefficient of respectively 40 drag counts (7.3%) and 46 drag counts (8.4%). As was explained in the previous paragraph the L-E-RE configuration has a higher drag coefficient than the baseline L-E model at a yaw angle of 6° and 9°, which obviously also affects the wind averaged drag coefficient. The wind averaged drag coefficient of the L-E-RE configuration is therefore 95 drag counts (17.4%)

higher than the wind averaged drag coefficient of the baseline L-E model.

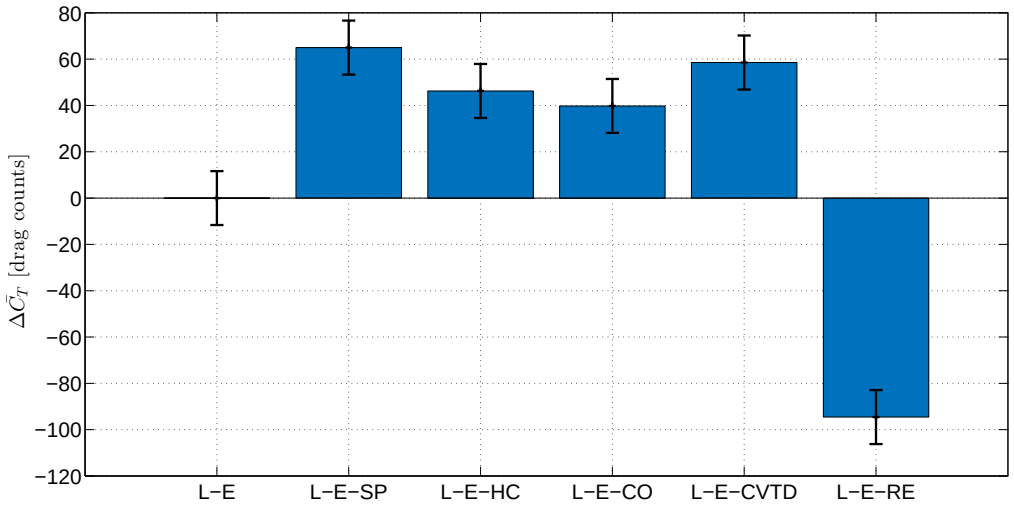

Figure 4.11: Wind averaged drag coefficient for the L-E baseline configuration with add-on devices

M-E baseline configuration

In a similar manner as for the L-E baseline configuration, two graphs were made to analyze the effectiveness of add-on devices for the M-E baseline configuration. Figure 4.12 shows the drag coefficient in function of the yaw angle for multiple cases of the M-E configuration. Due to time constraints only the baseline M-E configuration, the M-E configuration with a splitter plate (M-E-SP) and the M-E configuration with rounded edges (M-E-RE) were tested during the wind tunnel experiment. From Figure 4.12 it can be seen that the drag coefficient of the M-E baseline model drastically increases with increasing yaw angle. At a yaw angle of 0° the drag coefficient of the M-E baseline model equals 0.446, while at a yaw angle of 12° the drag coefficient is equal to 0.852. The two tested add-on devices significantly reduce the drag coefficient from a yaw angle of 3° onwards. At a yaw angle of 3° the drag reduction obtained by adding the splitter plate is 29 drag counts (6.2%), with the rounded edges add-on device the drag reduction equals 22 drag counts (4.7%). At a yaw angle of 12° the obtained drag reductions are significantly higher, namely 263 drag counts (30.8%) for the splitter plate and 201 drag counts (23.6%) for the rounded edges add-on device.

Figure 4.13 shows that the two add-on devices significantly reduce the wind averaged drag coefficient. Besides that it can also be noted that the splitter plate is more effective than the rounded edges add-on device, because the splitter plate delivers a wind averaged drag coefficient reduction of 138 drag counts (23.3%), while the rounded edges add-on device only reduces it by 124 drag counts (20.9%).

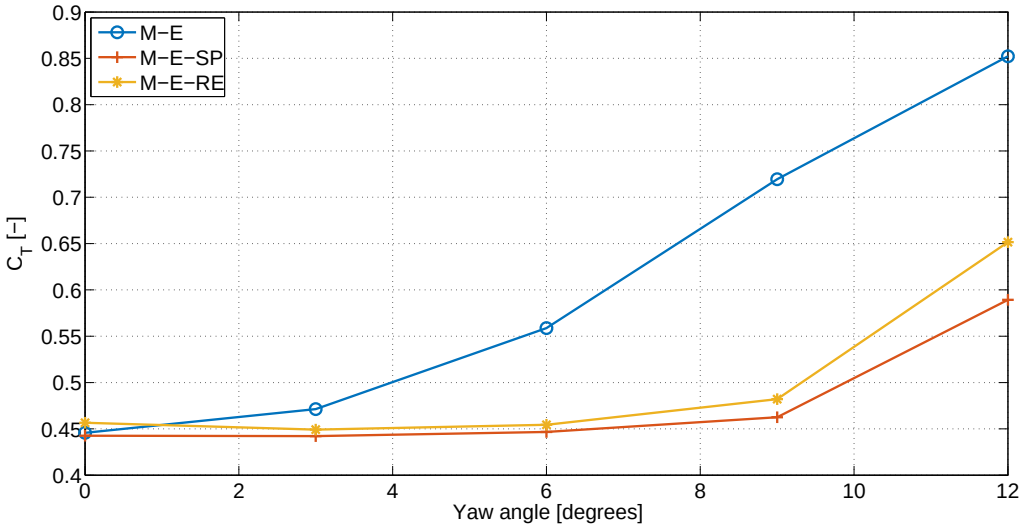

Figure 4.12: Influence of the yaw angle on the drag coefficient for the M-E baseline configuration with add-on devices

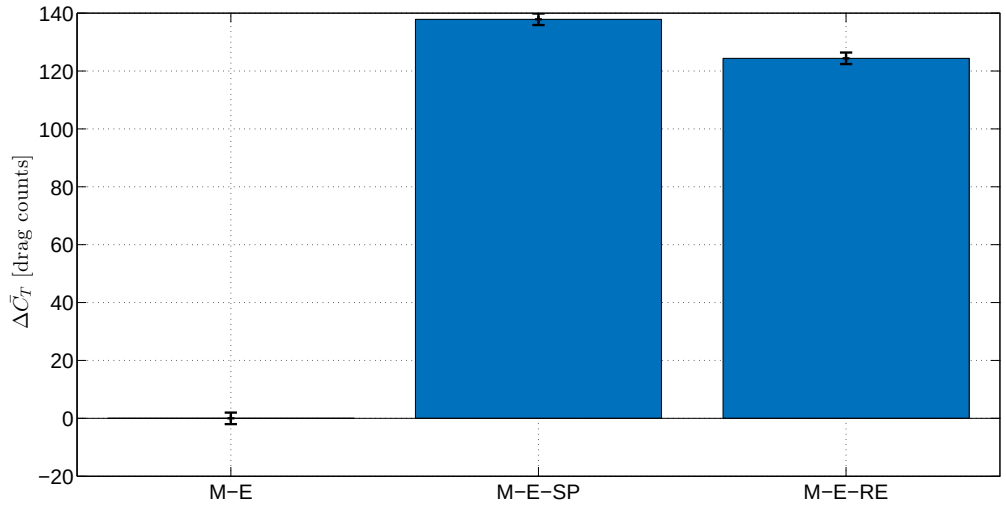

Figure 4.13: Wind averaged drag coefficient for the M-E baseline configuration with add-on devices

S-NE baseline configuration

From Figure 4.14 it is clear that the drag coefficient of the S-NE model increases with increasing yaw angle, no matter which add-on device is applied. The drag coefficient at 0° yaw angle is approximately 0.36 for all S-NE cases and goes up to 0.650 at 12° yaw angle for the S-NE case without any add-on device. Besides that it can be observed that for the S-NE baseline configuration the add-ons are most effective at higher yaw angles. At a yaw angle of 12° a drag reduction of 192 drag counts (29.6%) is achieved when the large side extenders (LSE) add-on device is attached to the baseline model. The LSE is the most effective add-on

device of all tested add-on devices at this yaw angle. The least effective add-on device at a yaw angle of 12° is the cabin splitter plate (CSP) with a drag reduction of 58 drag counts (8.9%).

The observation that the add-on devices are the most effective at a yaw angle of 12° is similar as what has been found for the L-E and the M-E configuration where the add-ons also resulted in the highest drag reduction at this yaw angle. One can also see from Figure 4.14 that all tested add-on devices result in a drag reduction for almost all yaw angles. For a yaw angle of 0° the differences between the measured results are so small (less than 10 drag counts), that it is hard to state that also at this yaw angle the add-on devices reduce the drag coefficient.

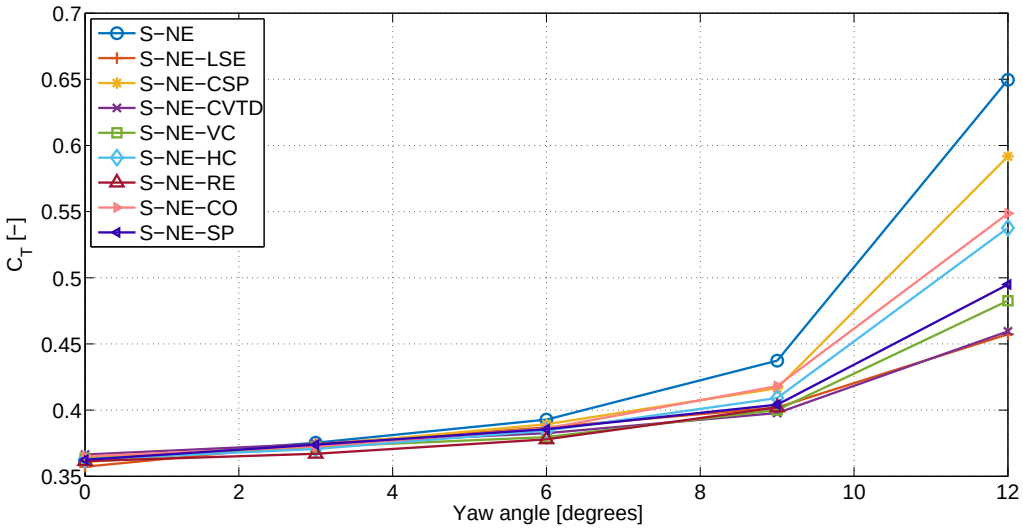

Figure 4.14: Influence of the yaw angle on the drag coefficient for the S-NE baseline configuration with add-on devices

Similar as for the L-E baseline configuration, the CVTD is one of the most effective add-on devices with a wind averaged drag coefficient reduction of 21 drag counts (5.1%). The CVTD is almost as effective as the vertical cylinders (VC) add-on device, which delivers a drag reduction of 22 drag counts (5.4%). This add-on device was not tested on the L-E configuration. After the VC and the CVTD, the LSE, the SP and the HC cause the largest wind averaged drag coefficient reduction with respectively 20 (4.9%), 18 (4.4%) and 16 (3.9%) drag counts (see Figure 4.15). Finally the CO and CSP are the least effective add-on devices for the S-NE configuration, with respectively a drag reduction of 12 (2.9%) and 10 (2.5%) drag counts. Note that all the obtained wind averaged drag coefficient reductions for the S-NE baseline case are in the range of 10-22 drag counts, while for the L-E case the wind averaged drag coefficient reductions were around 40-65 drag counts.

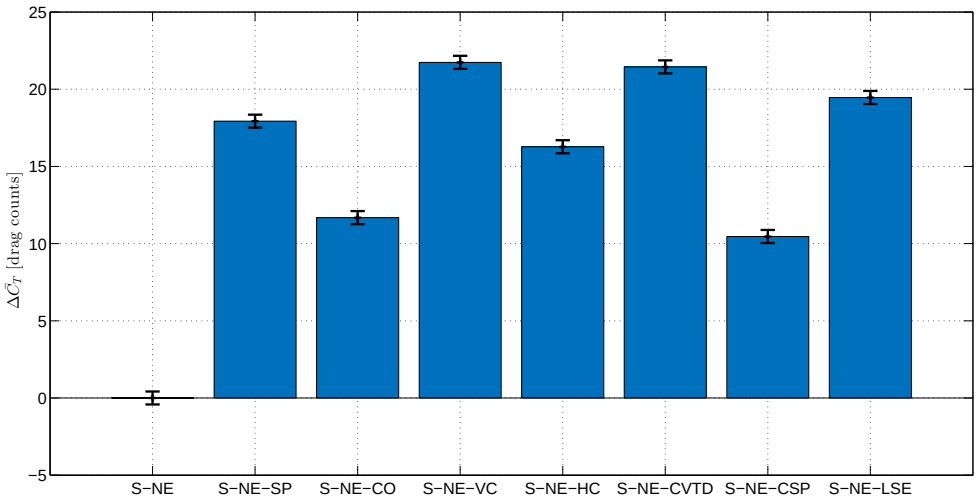

Figure 4.15: Wind averaged drag coefficient for the S-NE baseline configuration with add-on devices

S-E baseline configuration

The last baseline configuration that was tested with multiple add-on devices is the S-E configuration, which has a small tractor-trailer gap and extenders on the tractor. As can be seen in Figure 4.16, again in general the drag coefficient increases with the yaw angle no matter which add-on device is applied. However now the drag coefficient only increases from around 0.37 (0° yaw angle) to a maximum of 0.48 (12° yaw angle). The drag increase due to the yaw angle increase is significantly smaller than with the previous baseline cases. Figure 4.16 also shows the ideal impossible case of a fully closed tractor-trailer gap and as can be seen in the figure, the NG case lies closely to the other test cases. Only at a yaw angle of 12° the NG baseline model is significantly better than the S-E baseline model as the drag coefficient is reduced by 47 drag counts (10.0%).

The differences between all the applied add-on device are rather small. This is clearly visible in Figure 4.16 and Figure 4.17. It is remarkable that most add-on devices slightly increase the wind averaged drag coefficient as can be seen in Figure 4.17. This can be caused by an increase in viscous drag as more surface is added by the add-on device or also due to a slight misalignment of the add-on device during the wind tunnel experiment. The difference in wind averaged drag coefficient is for most add-on devices in the range 5 drag counts, which is within the uncertainty region of the measurements. As the differences are within the uncertainty region it is hard to draw any conclusions.

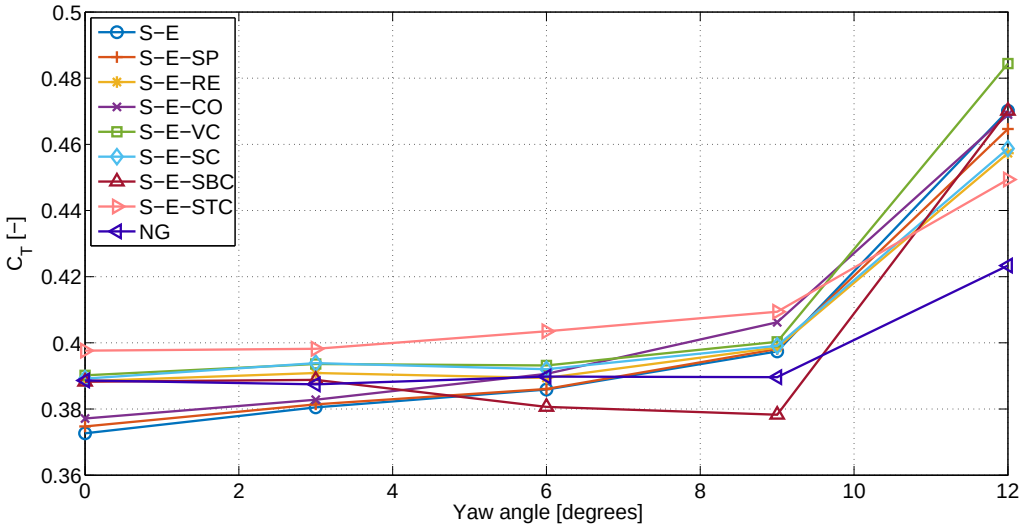

Figure 4.16: Influence of the yaw angle on the drag coefficient for the S-E baseline configuration with add-on devices

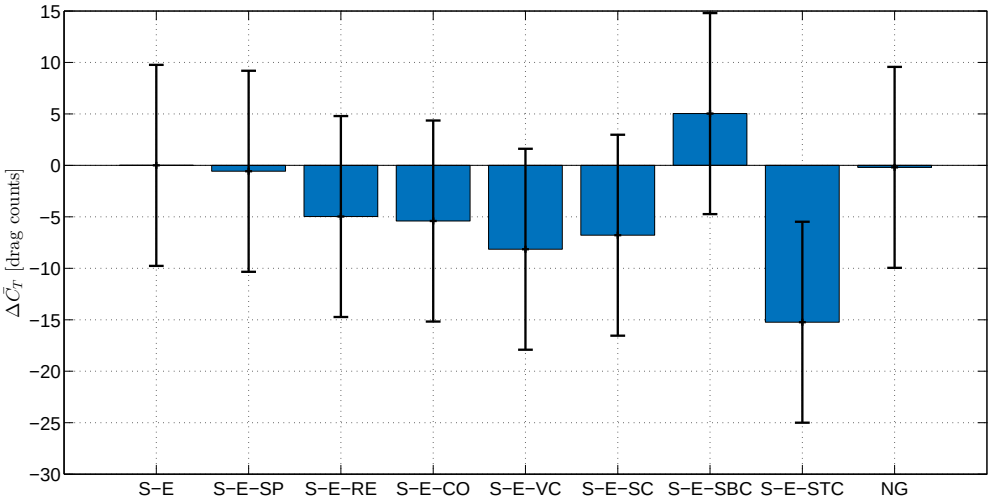

Figure 4.17: Wind averaged drag coefficient for the S-E baseline configuration with add-on devices

4.2.4 Pressure measurement results

As was explained in subsection 4.1.3 also pressure measurements were performed during the wind tunnel experiment. The main goal of measuring the pressure at certain locations on the wind tunnel model is that these measurement data can be used to validate the CFD simulations. As was mentioned before measuring the pressure was a very time-consuming task as the pressure measurement device could only read one pressure tab at a time. Therefore it was decided to only use 8 pressure tabs at the front of the cabin and 10 at the front of the trailer. Furthermore the pressure measurements were only performed on the L-E baseline

configuration with no add-on devices.

Pressure measurement at the front of the cabin

The location and the numbering of the 8 pressure tabs on the front of the cabin can be seen in 4.18(a). 4.18(b) shows the pressure coefficient as a function of the yaw angle for these 8 pressure tabs. The graph also includes small dotted lines which represent the 68% confidence intervals of the pressure measurements. The confidence intervals are determined by calculating the standard deviation of the measured data. The calculation of the standard deviation and the sensitivity of the results are discussed in subsection 4.2.6.

At a yaw angle of 0° the pressure coefficient is negative for all 8 pressure tabs as it varies between -0.07 (L3) and -1.53 (R3). These negative values for the pressure coefficient can be explained since the pressure tabs are located on the rounded edge of the front of the cabin. The incoming flow accelerates over this rounded edge. There is a low pressure region at the position of the pressure tabs, resulting in a negative pressure coefficient.

The pressure coefficient is significantly more negative at the right side of the vehicle. This is probably because the model was not perfectly symmetric and not perfectly aligned during the wind tunnel test. The left side of the wind tunnel model is slightly turned in the direction of the free stream flow, while the right side is turned away from the flow. This causes a higher pressure at the left side and a lower pressure at the right side. This is also clearly visible for the two pressure tabs located at the top of the cabin (L1 and R1).

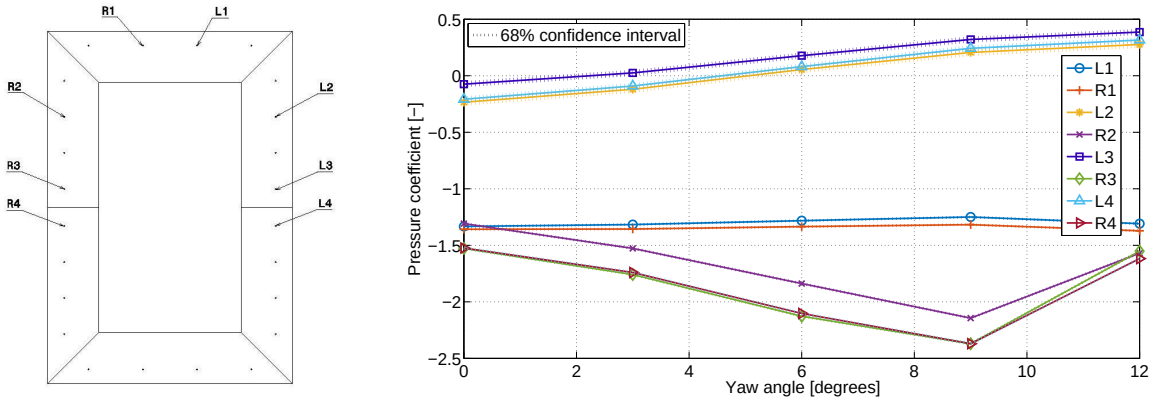

(a) Position of the pressure tabs on the front of the cabin

(b) Pressure coefficient as a function of the yaw angle

Figure 4.18: Pressure measurement on the front of the cabin

When the yaw angle is increased from 0° to 12° the pressure coefficient at the left side significantly increases, because the left side of the heavy-duty vehicle is turned more into the direction of the free stream flow, i.e. closer to the stagnation point. At the right side of the model the pressure tabs experience a more negative pressure coefficient (i.e. more suction) when the yaw angle is increased until a yaw angle of 9°. However after 9°, the pressure

coefficient becomes drastically less negative. If one looks at Figure 4.10, one can see that drag coefficient significantly increases when the yaw angle is increased from 9° to 12°. So the drastic loss in suction at the front of the cabin goes together with a drastic increase in drag coefficient.

Pressure measurement at the front of the trailer

10 pressure tabs were placed at the frontal surface of the trailer, the location of these pressure tabs can be seen in 4.19(a). As can be seen in the drawing, 6 pressure tabs were located more in the middle of the trailer frontal surface, while the other 4 pressure tabs were placed close to the left and right side of the frontal surface. The pressure coefficient of the latter mentioned ones is plotted in 4.19(b). The pressure coefficient of the pressure tabs located on the left side increases with the yaw angle. The pressure coefficient of L4 and L5 raises up to respectively 0.84 and 0.63 at a yaw angle of 12°. So at a yaw angle of 12° the left side of the trailer frontal surface experiences almost full stagnation flow. As the yaw angle is so large, the air flows along the left side of the cabin, enters the tractor-trailer gap and impinges on the frontal surface of the trailer.

Regarding the right side of the trailer frontal surface, it is harder to see a clear pattern. The pressure coefficient of R4 varies between -0.34 (3°) and 0.01 (9°) and for R5 the pressure coefficient is minimal -0.24 (3°) and maximal -0.05 (9°). One can note that the pressure coefficient of both R4 and R5 increase slightly from 3° till 9° and after 9° the pressure coefficient gets more negative.

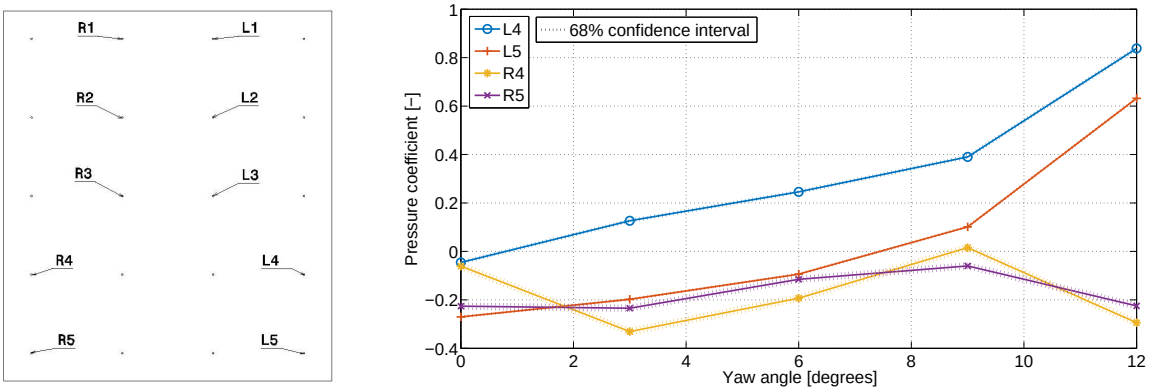

(a) Position of the pressure tabs on the front of the trailer

(b) Pressure coefficient as a function of the yaw angle

Figure 4.19: Pressure measurement on the front of the trailer

Figure 4.20 shows the pressure coefficient of the other 6 pressure tabs, which are located centrally on the trailer frontal surface. The pressure coefficient of L1 and R1 vary respectively between 0.33 and 0.56; and 0.35 and 0.75. The pressure at these locations (L1 and R1) on the top of the frontal surface is significantly higher than at the other measurement locations (L2, L3, R2 and R3). This is probably because a large amount of air flows above the cabin,

enters the tractor-trailer gap and impinges on the upper part of the trailer frontal surface.

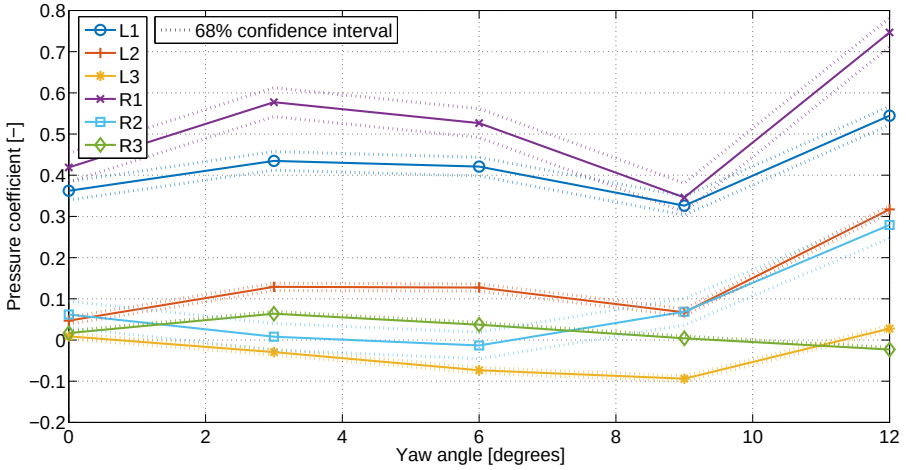

Figure 4.20: Pressure coefficient as a function of the yaw angle on the middle of the frontal trailer surface

At a yaw angle of 0° the pressure coefficients at L2, R2, L3 and R3 lie very close to each other, namely all between 0.06 and 0.01. Furthermore one can observe that for most pressure tabs there is a kink in the pressure coefficient at a yaw angle of 9°. For L1, R1 and L3 the pressure coefficient is the lowest at a yaw angle of 9°. And for L2 the pressure coefficient is then also significantly lower than at a yaw angle of 3°, 6° or 12°.

4.2.5 Flow visualization results

Not only quantitative measurements methods were applied, but also qualitative measurements methods, more particularly flow visualization by means of smoke and tufts. By analyzing a plume of smoke, one can understand more of the flow dynamics around the heavy-duty vehicle. Besides this the flow visualization can also be used to give more insight in the validation process of the CFD simulations.

The most important observation was that for the L-E configuration at a yaw angle of 12° the smoke plum entered the tractor-trailer gap and hit the frontal surface of the trailer (see 4.21(a)). During the wind tunnel campaign it was clearly visible that at that yaw angle there was a large region of separated flow at the leeward side of the trailer. When a splitter plate was attached to the frontal surface of the trailer the flow got enclosed in the corner between the windward side of the splitter plate and the frontal surface of the trailer (see 4.21(b)).

During the wind tunnel campaign also movable tufts were applied as flow visualization method. By observing the tufts, it was clear that the flow at the base of the trailer, so in the wake of the vehicle, was very unsteady and separated. Afterwards tufts were also placed in the tractor-trailer gap and also there separated flow was observed.

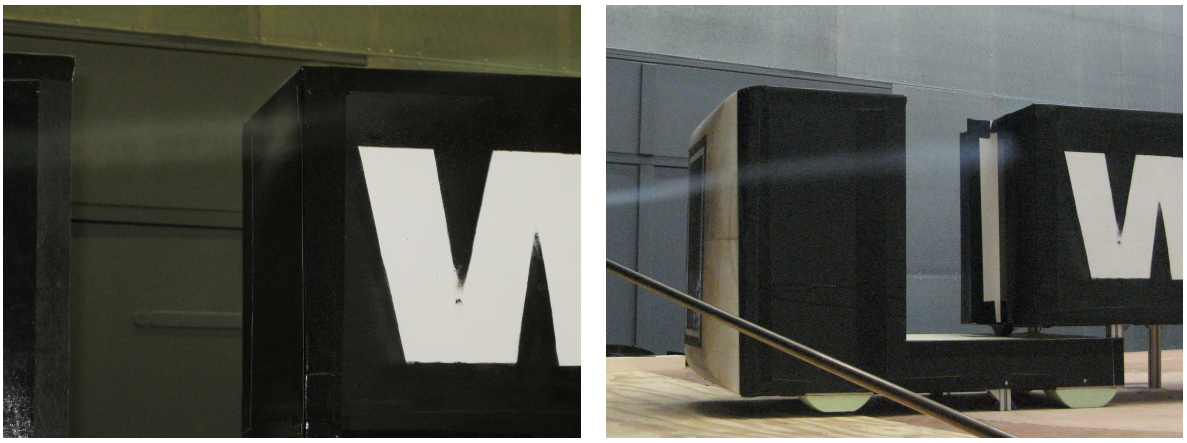

(a) L-E configuration without add-on device

(b) L-E configuration with splitter plate

Figure 4.21: Smoke plume entering the tractor-trailer gap of the L-E configuration

4.2.6 Measurement sensitivity and reliability

When performing experiments it is of crucial importance to check that the measured data are consistent and reliable. Ideally one has to test all the configurations multiple times to make sure that every time the same data are measured, but due to time constraints it was decided that for this experiment only the baseline configurations would be tested multiple times (two to five times, depending on the baseline configuration). From the measurement series one can compute the mean value and the standard deviation. Table 4.2 shows the measured drag coefficient for the five iterations performed on the L-E baseline configuration, which had the largest deviation of all the baseline configurations. The table below also includes the mean value and the standard deviation of the measurements.

Table 4.2: Sensitivity of the measured drag coefficient for the L-E baseline configuration

Iteration	**0°**	**3°**	**6°**	**9°**	**12°**	$\bar{C}_T$
1	0.498	0.564	0.551	0.558	1.026	0.564
2	0.478	0.547	0.536	0.547	1.016	0.550
3	0.416	0.527	0.539	0.543	0.997	0.540
4	0.428	0.540	0.517	0.540	0.994	0.537
5	0.464	0.530	0.525	0.539	0.998	0.538
Average	0.457	0.542	0.533	0.545	1.006	0.546
Standard deviation	0.034	0.015	0.013	0.008	0.014	0.012

With the mean value and the standard deviation a confidence interval can be determined. When a normal distribution is assumed, the following formula can be applied to compute the 68% confidence interval of the measured data. In this formula μ stands for the mean value

and σ stands for the standard deviation.

$$P\left(\mu - \sigma \leqslant x \leqslant \mu + \sigma\right) = 0.68 \tag{4.8}$$

With Equation 4.8 the confidence intervals for all the baseline configurations could be determined. Figure 4.22 shows the drag coefficient as a function of the yaw angle for the five baseline configurations, the dotted lines represent the 68% confidence intervals. As can be seen from the graph, at low yaw angles (from 0° till 6°) the NG, S-E and the S-NE lie close to or within each other confidence intervals, but at higher yaw angles the differences between the baseline configurations are clearly distinguishable.

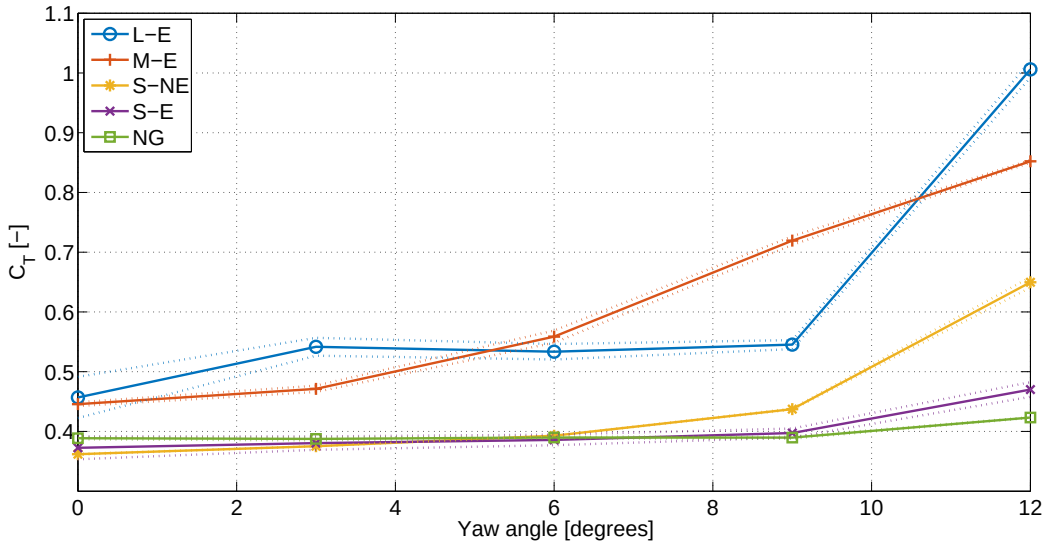

Figure 4.22: 68% confidence intervals (dotted lines) for the drag coefficient of the baseline configurations

The same method was applied to compute the uncertainty of the wind averaged drag coefficient. The wind averaged drag coefficient reduction graphs showed in subsection 4.2.3 contain error bars. These error bars also show the 68% confidence intervals. The confidence bars on the plots are very important additions to understand the effectiveness of the add-on devices. If one looks specifically at the wind averaged drag coefficient reductions for the S-NE baseline configuration (Figure 4.15) one can observe that the effect of the add-on devices on the wind averaged drag coefficient is clearly distinguishable. However for the S-E case (Figure 4.17), the drag reduction caused by the add-on devices is within the uncertainty interval of the measurements. So in this case no hard statement can be made whether the add-on devices reduce the wind averaged drag coefficient.

There are several reasons why measuring the same configuration at a different moment can lead to slightly different measured coefficients. Firstly the edges of the model and the screws in the model were covered with tape to obtain smooth surfaces, but sometimes the tape got a

bit loose which can affect the measurements. Some parts had to be taped a few times, which also affects the geometry of the test model, as it is impossible to tape them exactly the same. Secondly although the engine of the turning device was always switched off when performing a measurement, it was observed that the turning device and the whole test model vibrated slightly. Thirdly the accuracy of the balance system is limited. The maximum deviation in the direction of the drag is 0.06% which can lead to errors of up to half a drag count (Alons (2008)). Fourthly as was discussed in section 1.3 the drag force can oscillate significantly when the normalized gap length is large. Although that the drag force is averaged out over a measurement time of 60 s, these large fluctuations can cause some small discrepancies between the different iterations.

4.2.7 Conclusions regarding the experimental results

The experimental results can be summarized in a few bullet points.

- It was observed that the drag coefficient can be regarded as independent from the Reynolds number, if the Reynolds number based on the square root of the cross-sectional area is larger than approximately $5 \cdot 10^5$. All tests in the OJF were performed at a Reynolds number of $8.5 \cdot 10^5$, so behind the critical Reynolds number.
- The gap length significantly influences the drag coefficient of the heavy-duty vehicle, especially at larger yaw angles. In most cases the wind averaged drag coefficient increases with increasing gap length, but this is not always true. The wind averaged drag coefficient of the M-E baseline model is 46 drag counts larger than the wind averaged drag coefficient of the L-E baseline model.
- Attaching add-on devices to the baseline configurations greatly reduces the drag coefficient. The highest drag reductions by adding add-on devices were achieved for the L-E and M-E configuration. For both cases the splitter plate was the most effective add-on device. When attaching a splitter plate to the trailer frontal surface, the wind averaged drag coefficient was reduced by 138 drag counts (23.3%) for the M-E configuration and by 65 drag counts (11.9%) for the L-E configuration.
- The cross vortex trap device and the vertical cylinders were the most effective add-on devices for the S-NE configuration, with wind averaged drag coefficient reductions of respectively 21 drag counts (5.1%) and 22 drag counts (5.4%). They were closely followed by the large side extenders, the splitter plate and the horizontal cylinders with wind averaged drag coefficient reductions of respectively 20 (4.9%), 18 (4.4%) and 16 drag counts (3.9%).
- Regarding the S-E configuration the effect of the add-on devices can be regarded as negligibly small as the effect was smaller than the sensitivity of the performed tests. It was observed that the wind averaged drag coefficient of the S-E model lies very close to the ideal NG case. So the possible gain of add-on devices cannot be large.
- The yaw angle clearly affects the pressure coefficients at the frontal surface of the cabin and the trailer of the L-E configuration. The left side of both surfaces experiences

higher pressure when the yaw angle is increased, because then the surfaces are more orientated towards the incoming flow. After 9° yaw angle the right side of the cabin abruptly experiences a drop in the pressure coefficient. This drops goes together with a large increase in drag coefficient.

- The flow visualization showed that at a yaw angle of 12° a large amount of air enters the L-E tractor-trailer gap and impinges on the trailer frontal surface. This is the cause of the high pressure coefficients at large yaw angles.
- A sensitivity analysis was performed on the baseline configurations. The standard deviation of the wind averaged drag coefficient of the L-E configuration is 12 drag counts, which was the largest off all baseline configurations.

Chapter 5

Discussion of the Results

As was pointed out earlier one of the main goals of the experimental campaign was to act as validation for the numerical analysis. In this chapter the results of the two methods will be compared and the differences in results will be analyzed in detail. Although that the two methods are performed as similar as possible, it was impossible to avoid some differences due to practical limitations. These differences in set-up will be discussed in section 5.2.

5.1 Comparison between the numerical and experimental results

In this section the results of the numerical analysis will be compared with the results of the experimental analysis. First the drag coefficients of the baseline models will be compared with each other, afterwards the drag coefficients of the models equipped with add-on devices and finally the experimental and numerical results of the pressure on the surface of the L-E baseline model will be compared with each other. All the graphs in this section contain solid and dashed lines. The solid lines represent the experimental results, while the dashed lines indicate the numerical results.

This section only compares the numerical with the experimental results and describes the observed facts. The following section, section 5.2, will provide explanations and reasons why there are discrepancies between the numerical and experimental results.

5.1.1 Baseline configurations

In this section the results of the numerical and experimental analysis of the baseline configurations will be compared with each other. Figure 5.1 shows both the numerical and experimental

results for the drag coefficient of the baseline configurations for various yaw angles. Table 5.1 shows the difference in drag coefficient (in drag counts and in percentages) of the L-E, M-E, S-NE and the NG baseline model compared to the S-E baseline model. The drag values are compared with the S-E baseline model as this is the model which represents the average heavy-duty vehicle driving on the road in Europe. In the table both the numerical and the experimental results are included. Several interesting observations can be drawn from this graph and table.

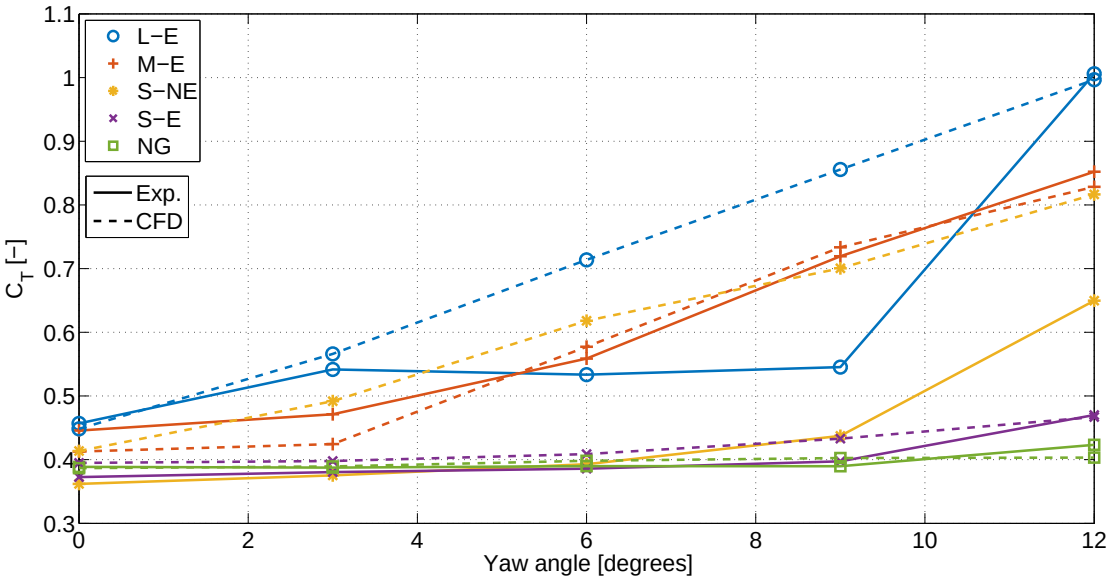

Figure 5.1: Comparison between the numerical and experimental results of the drag coefficient of the baseline configurations for various yaw angles

Table 5.1: Drag difference of the baseline models compared to the S-E baseline model, both in drag counts and percentages, a positive value means a higher drag coefficient than the S-E baseline model

Model	0°	3°	6°	9°	12°
L-E (Exp.)	84 (22.6%)	161 (42.4%)	148 (38.2%)	148 (37.2%)	536 (114.0%)
L-E (CFD)	54 (13.5%)	168 (42.2%)	305 (74.7%)	423 (97.6%)	530 (113.4%)
M-E (Exp.)	73 (19.6%)	91 (23.9%)	173 (44.8%)	322 (81.1%)	382 (81.2%)
M-E (CFD)	18 (4.5%)	27 (6.7%)	169 (41.3%)	301 (69.4%)	361 (77.4%)
S-NE (Exp.)	-11 (-2.9%)	-5 (-1.4%)	7 (1.8%)	40 (10.1%)	179 (38.2%)
S-NE (CFD)	19 (4.7%)	94 (23.6)	209 (51.2%)	268 (61.8%)	350 (74.8%)
NG (Exp.)	16 (4.3%)	7 (1.8%)	4 (1.0%)	-8 (-2.0%)	-47 (-10.0%)
NG (CFD)	-8 (-2.1%)	-9 (-2.2%)	-11 (-2.7%)	-30 (-7.0%)	-64 (-13.6%)

Firstly, the agreement between the numerical and experimental results is very dependent on the yaw angle. At a yaw angle of 0° the numerical and experimental results lie very close to each other. For example for the NG configuration the drag coefficient according to the

simulations is 0.387, while the experimental analysis gives a drag coefficient of 0.389. This is a difference of only 2 drag counts or 0.5%. At higher yaw angles, the differences between the experimental and numerical results can be rather large. For example for the same NG configuration but now at a yaw angle of 12°, the difference between the two methods is 20 drag counts (4.7%).

Secondly, the agreement of the results is very dependent on the configuration. From Figure 5.1 it is clear that the numerical results follow the trends of the experimental results well for the NG, S-E and M-E configuration, but for the S-NE and L-E configuration the trends are predicted incorrectly by the numerical simulations. Where the experimental results show a small increase of 31 drag counts (8.5%) in drag coefficient of the S-NE configuration between 0° and 6° yaw angle, the numerical results predict a steep increase of 205 drag counts (49.4%) for the drag coefficient. At a yaw angle of 3° and 6° the numerical simulations show large regions of separated flow along the leeward side of the cabin and the trailer of the S-NE baseline model, while there is no indication that there was a large region of separated flow along the leeward side of the vehicle during the experiment. The reason why the numerical simulation predicts a different flow field compared to the experimental analysis is explained in more detail in subsection 5.2.2.

Thirdly, both the experimental and the numerical results show that the NG and the S-E configuration are only slightly affected by the yaw angle, especially when the yaw angle is small. For example between a yaw angle of 0° and 9° the drag coefficient of the S-E baseline model obtained by the experimental method only increases with 25 drag counts (6.7%). As can be seen in Table 5.1 the results of the S-E configuration lie close to the results of the NG configuration. Between 0° and 9° the largest difference between the NG and the S-E baseline model according to the numerical simulations is only 30 drag counts, according to the experimental results the largest difference between the two baseline models is only 16 drag counts. That the differences between the two baseline models are small can be explained by the fact that in the S-E configuration the tractor-trailer gap is small and the extenders on the sides and on the roof make the effective gap length even smaller. So by having a small gap length and adding extenders to the cabin, the S-E configuration achieves almost the same results as the ideal NG configuration, which has no tractor-trailer gap. Furthermore according to both the numerical and the experimental results the drag coefficient of the S-E and the NG configuration is significantly lower compared to the L-E and M-E configuration for all the tested yaw angles. This shows that having a small gap length or no gap at all is much more efficient than having a rather large tractor-trailer gap.

Fourthly, Figure 5.1 shows that the drag coefficient of the M-E and L-E configuration is clearly more dependent on the yaw angle compared with the other three baseline models. In other words in general when the yaw angle is increased, the drag coefficient significantly increases for both the M-E and the L-E configuration. Although, the numerical results do not always exactly follow the experimental results, especially for the L-E configuration, the overall gradient of the increase in drag coefficient is predicted rather well. If one analyses specifically the L-E configuration, one can see that CFD is able to approximately capture the correct gradient between 0° and 3° yaw angle. The numerical results for 6° and 9° yaw angle are completely different than the experimental results (discrepancies of up to 310 drag counts), but for a yaw angle of 12° the results match again very well, the difference is even

less than 1%. The simulations predict flow separation along the leeward side of the vehicle starting from a yaw angle of 6°, while in the experimental campaign leeward separation most probably only occurred from a yaw angle of 12°. The hypothesis is that the numerical method has difficulties with predicting the correct onset of flow separation, but when there is indeed flow separation it can accurately predict the effect on the drag coefficient. This hypothesis would also explain why the numerical and experimental results agree much better for the M-E configuration. As the CFD and probably the experimental analysis both predict flow separation from a yaw angle of 6°.

5.1.2 Add-on devices

Both the numerical and the experimental analysis method were applied to investigate the effect of add-on devices on the drag coefficient of the heavy-duty vehicle. This section will compare the results of both methods and describe the differences. As only numerical simulations were performed on the splitter plate and on the rounded vertical edges, only these add-on devices will be included in the comparison. Furthermore these simulations were only executed until a yaw angle of 9°.

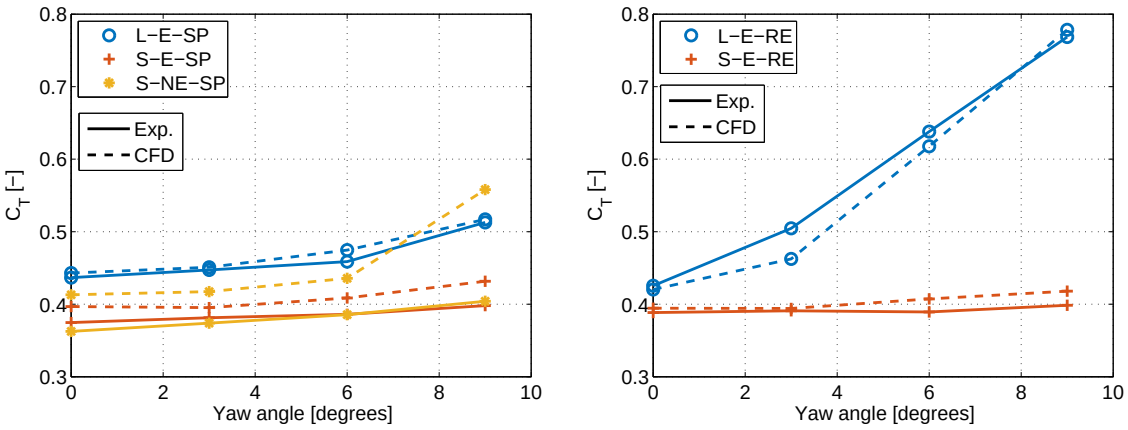

(a) Splitter Plate (SP)

(b) Rounded Edges (RE)

Figure 5.2: Comparison between the numerical and experimental results of the drag coefficient of the configurations equipped with add-on devices for various yaw angles

Figure 5.2 shows the numerical and experimental results for the L-E and S-E configuration equipped with a splitter plate or rounded edges. Regarding the splitter plate also simulations were performed on the S-NE configuration. Although the numerical results do not exactly match with the experimental results, the difference is in average around 5%, the trend is in general followed rather accurately. In contrast with the L-E baseline configuration, the trend of the drag coefficient of the L-E-SP configuration in function of the yaw angle is predicted well by the numerical simulations. The reason why the results are more accurate for the splitter plate case is probably because for the splitter plate case no leeward separation regions are predicted by the CFD, while it is probably incorrectly predicted for the normal L-E baseline

configuration (see also subsection 3.2.3 and specifically Figure 3.23).

As can be seen in 5.2(a) the trend of the numerical and experimental results for the S-NE-SP configuration match very well until a yaw angle of 6°. However at 9° yaw angle the experimental results show a slight increase, while the numerical results indicate a steep increase in drag coefficient. This is again probably due to an incorrectly predicted onset of separation at the leeward side of the vehicle. The numerical results show a large region of separated flow at the leeward side of the cabin, while there is no explicit evidence that the experimental results indicate a region of separated flow at the leeward side.

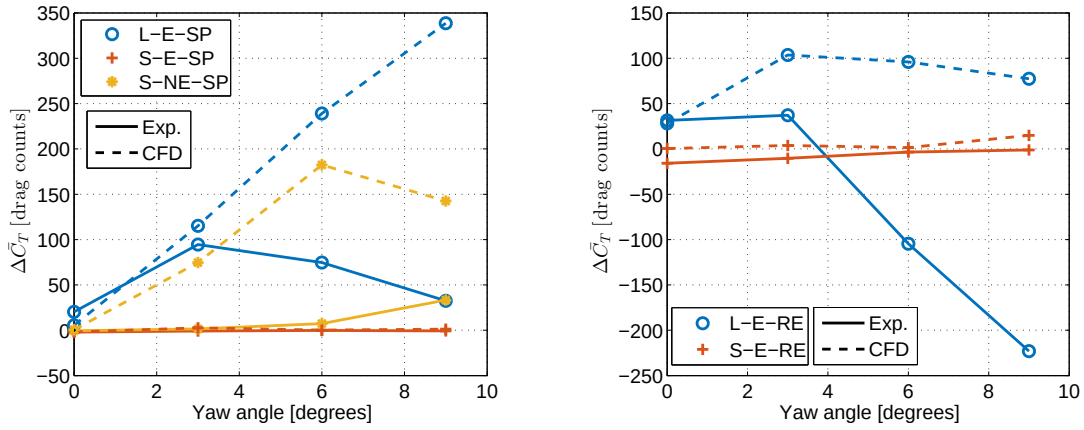

(a) Splitter Plate (SP)

(b) Rounded Edges (RE)

Figure 5.3: Drag reductions in drag counts obtained with the SP and the RE add-on device for various yaw angles according to the numerical and experimental results

Figure 5.3 shows the obtained drag reductions when the splitter plate or the rounded edges add-on device is attached to one of the baseline models. As can be seen in Figure 5.3 the obtained drag reductions for the S-E baseline model are negligibly small, the maximum obtained drag reduction is 15 drag counts (3.5%) with the rounded edges add-on device at a yaw angle of 9° according to the numerical results. The experimental results show that adding the rounded edges add-on device on the S-E baseline model can even slightly increase the drag coefficient, however this is within the uncertainty of the performed measurements (see also section 4.2.3). The increase in drag coefficient can be caused by a slight misalignment of the add-on device during the wind tunnel experiment.

Both the experimental and the numerical results show that the splitter plate add-on device clearly reduces the drag coefficient of the L-E and the S-NE baseline model. For example according to the experimental results a drag reduction of 33 drag counts (7.5%) is obtained at a yaw angle of 9° for the S-NE baseline model. However, the achieved drag reductions are significantly overpredicted by the numerical simulations. This is also the case for the L-E-RE configuration shown in 5.3(b), where the numerical results indicate a drag reduction of up to 104 drag counts (18.4%), while the experimental results show a drag increase of up to 223 drag counts (40.9%). This is because the numerical simulations have difficulties with predicting the correct drag coefficient of the L-E and the S-NE baseline model as was discussed in the

previous section (subsection 5.1.1).

The experimental results show a drag increase at a yaw angle of 6° and 9° when the rounded edges add-on device is attached to the L-E baseline model. This is probably because of the same reason why the experimental results indicate that at the same yaw angles the M-E baseline model has a higher drag coefficient than the L-E baseline model. Due to the addition of the rounded edges add-on device the L-E-RE model has a normalized gap length of 0.560, which is closer to the normalized gap length of the M-E baseline model (0.483) than to the normalized gap length of the L-E baseline model (0.688). As was explained earlier in subsection 4.2.2 the hypothesis is that the wake of the cabin nicely fits in the gap for the L-E baseline model, but when the gap length is shortened, it is not longer the case and then separation at the leeward side of the vehicle occurs at a lower yaw angle. A similar behavior was also observed by Hammache and Browand (2004), but the authors of this study did not give any explanation for this particular behavior.

5.1.3 Pressure comparison

As was explained earlier also pressure measurements were performed during the wind tunnel test. These pressure measurements were only performed on the L-E baseline configuration due to time constraints. From the numerical simulations one can also obtain the pressure coefficient at certain locations on the vehicle. The numerical results of the pressure coefficient are obtained from the last iteration only and are not an average value over the last 1,500 iterations. In this sections the experimental obtained pressure data will be compared with the numerical results.

Figure 5.4 shows the pressure coefficient for 8 different locations at the cabin frontal curved surface obtained by the experimental and numerical analysis. The exact locations of the pressure tabs can be found in section A.2. The numerical and experimental results for the pressure coefficient differ significantly from each other. For example regarding pressure tab L2 the difference can go up to more than 80%. Only for the pressure tabs located in the top of the cabin frontal curved surface, L1 and R1, the absolute difference is not large, more precisely maximum 9.2%. However in this research study the goal is to analyze trends and not specifically the correct absolute values. If one compares the trends predicted by the numerical and experimental analysis, one can see that the trend of the numerical and experimental results is similar for the the pressure tabs located at the left and top side of the cabin (respectively L2, L3 and L4 and L1 and R2). The pressure coefficient at the left side of the cabin increases significantly as it experiences more and more stagnation flow when the yaw angle is increased. Regarding L1 and R1 the pressure coefficient is approximately independent of the yaw angle, because the pressure tabs are located almost in the middle of the width of the vehicle.

Regarding the pressure tabs located at the right side of the vehicle clearly a different pattern in the pressure coefficient as a function of the yaw angle can be observed. Both the experimental and the numerical results indicate a decrease in pressure coefficient between a yaw angle of 0° and 3°, but according to the experimental results the pressure coefficient decreases further

until a yaw angle of 9°, while the numerical results show an increase in pressure coefficient after 3°. So here a trend reversal can be observed. According to the numerical simulations there is flow separation at the leeward side of the cabin at a yaw angle of 6°, which is the reason of the pressure increase between 3° and 6°. However according to the experimental results it is most likely that leeward separation only occurs from a yaw angle of 12°, where a steep increase in drag coefficient and pressure can be observed. So the hypothesis is that the difference in the trend between the numerical and experimental results is due to incorrectly predicting the onset of flow separation by CFD. This also explains why the numerical and experimental results for a yaw angle of 12° match much better with each other, as both methods then predict flow separation at the leeward side of the cabin.

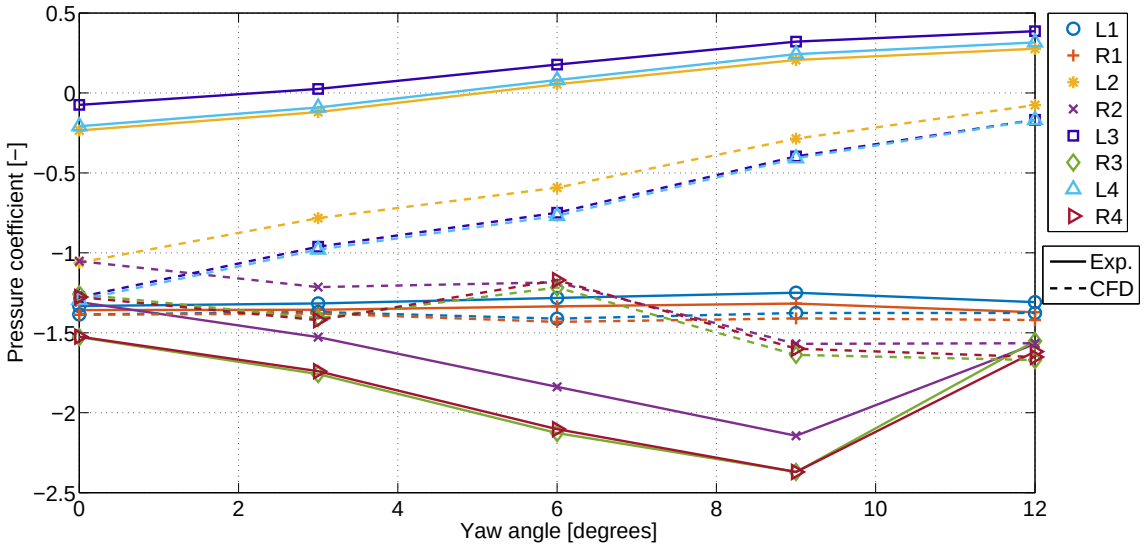

Figure 5.4: Comparison between the numerical and experimental results of the pressure coefficient at the cabin frontal curved surface

Regarding the pressure coefficient on the trailer frontal surface the results of the numerical and experimental analysis differ significantly from each other, more than for the cabin frontal curved surface. This is clearly visible in Figure 5.5 and Figure 5.6. For the pressure tabs L4 and L5 one can say that only the general trend of increasing pressure coefficient between 0° and 12° is captured by both the numerical and the experimental analysis as these pressure tabs experience more and more stagnation flow when the yaw angle is increased. Regarding the other pressure tabs (L1 - L3 and R1 - R5) not even the general trend of the numerical and experimental results match with each other. This is probably because the flow field inside the tractor-trailer gap is rather unsteady and the numerical simulations solve for a steady mean flow. Furthermore only the last iteration was used to compute the pressure coefficient, which also influences the results of the numerical analysis.

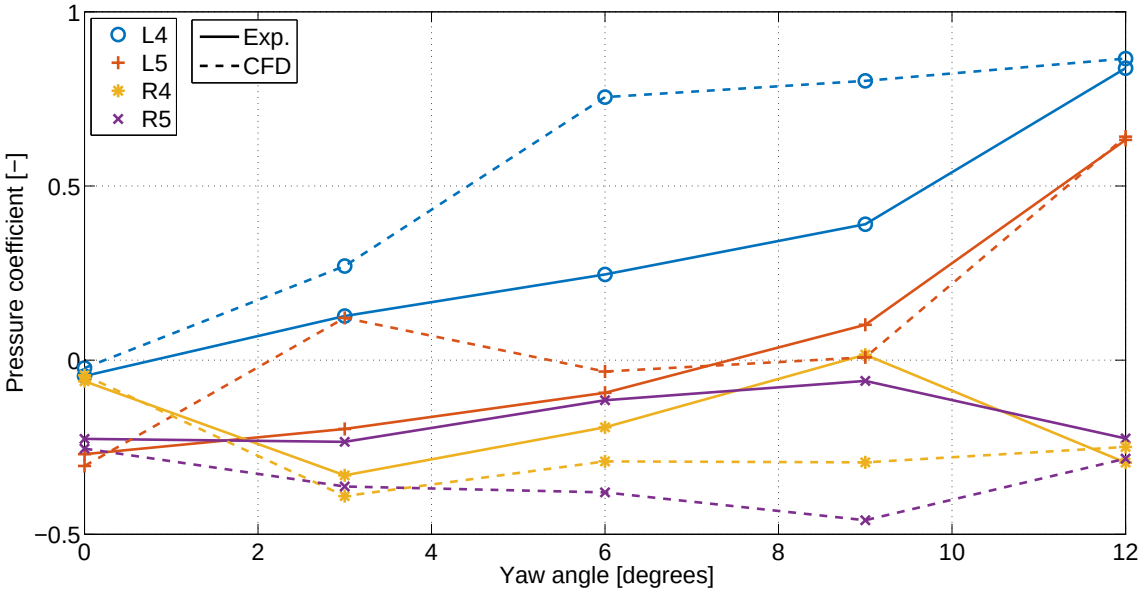

Figure 5.5: Comparison between the numerical and experimental results of the pressure coefficient at the edges of the trailer frontal surface

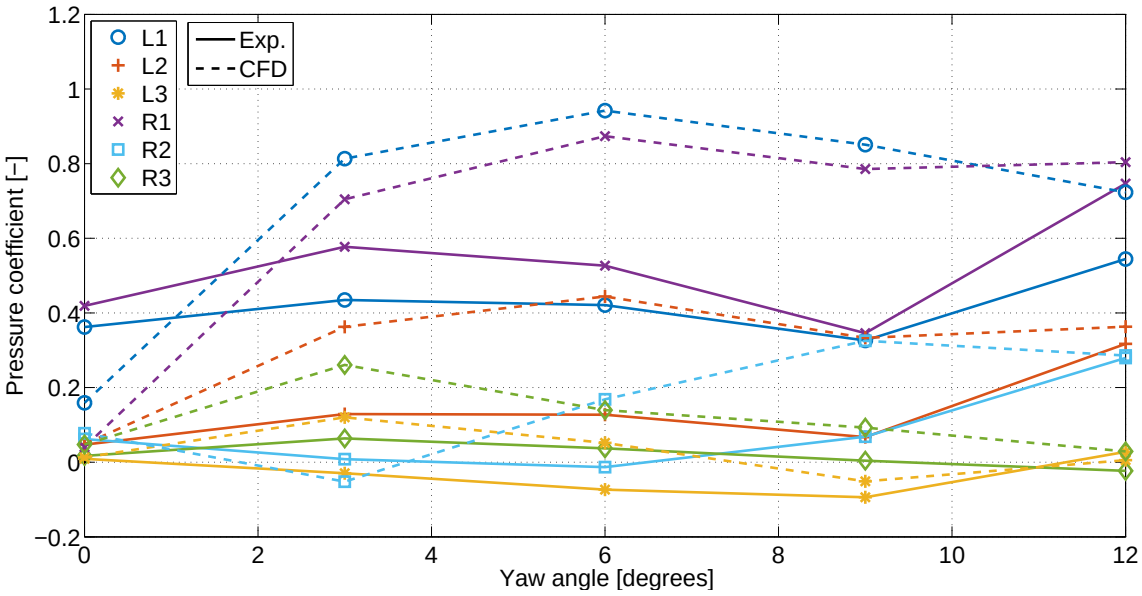

Figure 5.6: Comparison between the numerical and experimental results of the pressure coefficient at the center of the trailer frontal surface

5.2 Explanation of the differences between the numerical and experimental results

In this study both a numerical and an experimental analysis was performed. It was decided to perform both in order to obtain more confidence about the results and to combine the

benefits of the two methods. To be able to compare the results of both methods, the settings and conditions of the two methods should match as good as possible with each other.

Although the aim was to perform the two analysis methods identically, some differences could not be avoided. These differences will be described in this section. Furthermore as was explained in the previous section for certain cases large discrepancies were found between the numerical and experimental results. This section will also elaborate on the reasons for these large discrepancies.

5.2.1 Test model

While designing the heavy-duty vehicle model meshing and manufacturing limitations were kept in mind. This lead to a simple, but still representative design. The simple design improved the consistency between the experimental and numerical analysis as it was easier to keep the geometry the same. Nevertheless, there were some small differences regarding the test model.

Firstly, the wind tunnel model was constructed out of multiple parts and materials. These parts were assembled together to form the complete model, but the connection between two different parts was not always smooth. For example between the 3D-printed front part of the cabin and the wooden side panels there was a small jump in height. To obtain a smooth transition between the parts the connection was covered with clay. However this is still not as smooth as the surfaces of the model that was used for the CFD simulations. Since different materials (for example foam, wood and pvc) were used for different parts, some parts had a different wall roughness. However in the numerical analysis one wall roughness was selected for the complete test model.

Secondly, there were some other imperfections in the wind tunnel model. As the complete wind tunnel model was hand made, the model did not have the exact desired shape. For example the edges were not exactly 90° degrees, but slight rounded. The wheels and some of the add-on devices were constructed out of foam, which was cut by using a hot-wire cutter. With this tool it is hardly impossible to get the parts exactly in the desired shape.

Thirdly, there were some small differences in the wind tunnel model compared to the numerical test model due to some practical limitations of the wind tunnel test set-up. To obtain enough structural integrity a few metal supports were attached to the model as can bee seen in the red circles in Figure 5.7. As can be seen in the same figure, just behind these beams some pressure tubes were located which ran from the bottom of the model to underneath the wooden turning disk (green circle). At the wheels of the trailer some more pressure tubes were mounted. As these pressure tubes are very thin and placed just behind the beams or wheels, it is expected that they do not significantly influence the flow behavior. Furthermore the front cabin wheels and the trailer wheels floated slightly above the ground platform as can be seen in the blue circles (Figure 5.7). If they would touch the ground platform they would induce loads on the platform, instead of on the turning disk and the balance system, which would result in incorrect balance measurements.

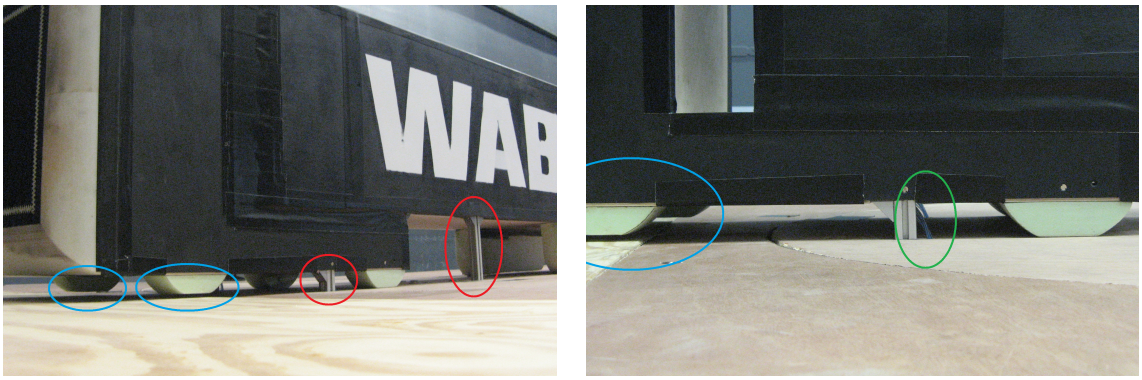

(a) general view (b) close-up

Figure 5.7: Differences between the wind tunnel test model and the numerical test model

Finally the wind tunnel model was not perfectly positioned. As was explained earlier in subsection 4.1.3 the model had a small misalignment ($< 1°$) in the yaw angle due to the accuracy of the turning device. The model was also placed under a very small angle of attack. As these misalignments were very small it was expected that they would not significantly affect the results.

5.2.2 Numerical errors

As was discussed in subsection 5.1.1 and subsection 5.1.2, large discrepancies were found in the drag coefficient for the S-NE and L-E configuration between the numerical and experimental results. It was observed that for every time there was a large difference in drag coefficient between the experimental and numerical results, the numerical results predicted a significantly higher drag coefficient compared with the experimental results. When one analyzed the simulated flow field around the vehicle, large regions of separated flow could be observed at the leeward side of the cabin (and sometimes also at the leeward side of the trailer). From the experimental results there was however no clear indication that there was a large region of separated flow at the leeward side of the vehicle in these cases. When during the wind tunnel experiment flow separation at the leeward side of the vehicle was observed with the use of the smoke plume, for example for the L-E baseline configuration at a yaw angle of 12°, the numerical simulations also predict flow separation and the values for the drag coefficient match again very well. So the hypothesis is that the numerical method is not capable of predicting the correct onset of flow separation, but it can accurately predict the effect on the drag coefficient if there is indeed flow separation.

An example of an incorrectly predicted onset of flow separation is the S-NE baseline configuration at a yaw angle of 3°, which is shown in 5.8(a). 5.8(a) clearly shows these wrongly predicted large regions of separated flow at the leeward side of the vehicle. In this figure one can see that there is strong jet of air coming from the tractor-trailer gap blowing at the

leeward side of the vehicle. Regarding the S-E configuration, which is exactly the same configuration but then with extenders attached to the cabin, this strong jet is not predicted nor any flow separation at the leeward side. The combination of the rounded edge at the front of the cabin with the jet coming from the gap blowing the boundary layer away from the vehicle surface is probably the reason why the numerical model predicts the flow separation regions at the leeward side. For the L-E configuration at higher yaw angles ($\geqslant 6°$) a similar flow pattern is predicted by the numerical simulations.

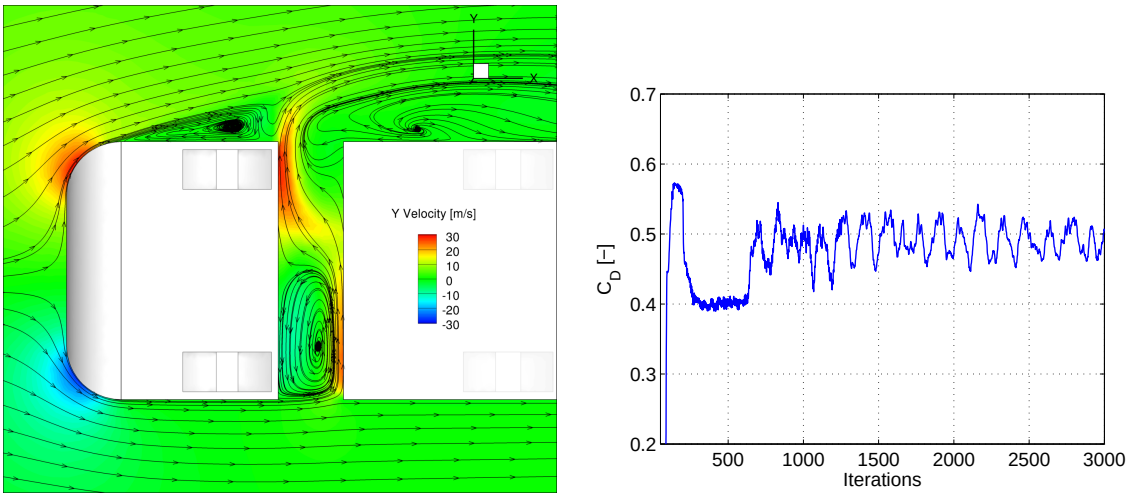

(a) Contour plot of the Y-velocity with arrows indicating the X-Y velocity streamlines at the middle gap height

(b) Convergence history

Figure 5.8: S-NE configuration at a yaw angle of 3°

It was observed that every time that the numerical simulations predict flow separation at the leeward side of the vehicle, the convergence diagram showed large oscillations instead of a smooth convergence with only small oscillations. The convergence history diagram for the S-NE configuration at a yaw angle of 3° is shown in 5.8(b). The large fluctuations are clearly visible in this figure. Furthermore one can see that until iteration 600 the fluctuations in the convergence history were significantly smaller and that the average value of the drag coefficient was much lower, namely around 0.4. This value of 0.4 is around the value that was expected from the experimental analysis. So the hypothesis is that until iteration 600 the flow field was correctly predicted by the numerical simulations (i.e. no regions of separated flow along the leeward side of the vehicle), but then from around iteration 600 flow separation was predicted and from that point all the intermediate solutions contained separated flow at the leeward side.

There are several reasons why the numerical simulations predict the flow behavior incorrectly. As can be seen in 5.8(b) the convergence history diagram contains large fluctuations, which means that the simulation actually does not find a good solution. So the results of the simulations should not be fully trusted as was already pointed out in the previous paragraphs. Furthermore while performing RANS simulations one makes several assumptions. The RANS

equations are a simpler form of the Navier-Stokes equations where one is solving for the steady mean solution. This means that if a problem is rather unsteady, RANS is not the most suitable model as it does not take unsteady effects into account. Furthermore the flow field inside the gap actually contains several small scale vortices and turbulent structures that interact with each other, which are not solved with the RANS equations. The same is valid for the (leeward) separation regions, which is clearly visible in the DES simulations of Hyams et al. (2011) (see Figure 1.10). To capture these small turbulent structures other methods like LES or DNS are required. An interesting follow-up study would be to investigate if other simulations methods like LES, DES or LBM are able to accurately predict the flow field around these baseline configurations when crosswind is applied.

The complete volume of the test domain is divided in many different cells. By discretizing the volume a numerical diffusion error is introduced. This leads to more diffusion in the simulations than what is actually true. According to the research performed by van Leeuwen (2009) the numerical diffusion has a clear effect on the simulated boundary layer around the GETS model. In this research prim layers were constructed to accurately capture the boundary layer and to minimize the numerical diffusion. However it is still possible that numerical diffusion has a certain impact on the numerical results.

The pressure coefficient obtained by the numerical simulations is only derived from the last iteration (i.e. iteration 3,000) and is not an averaged value over the last 1,500 iterations as was done for the drag coefficient. As was just described, the drag history contains large fluctuations for the L-E baseline configuration at large yaw angles, so the intermediate results of different iterations can vary significantly. So for the numerical pressure coefficient an instantaneous value was used, while for the experimental pressure coefficient the average value of 30 s measurement time was applied. This is one of the reasons why the pressure coefficients of the numerical results have large discrepancies compared to the pressure coefficients obtained by the experimental analysis.

5.2.3 Experimental errors

The previous section described the numerical errors, but also the experimental results contain small errors. As was explained in subsection 4.1.3 the balance, which measured the forces and moments, has a measurement error of 0.06% in the x-axis direction (Alons (2008)). The measured values were averaged over a time of 60 seconds, because after 60 seconds the mean value was almost completely converged. However increasing the measurement time even more, could have led to smaller measurement errors, as the mean value would then be even more converged.

Furthermore as was described in subsection 4.2.6 the turning device and the test model vibrated slightly during the measurement. This also affected the experimental results.

Chapter 6

Conclusions and Recommendations

In this chapter the conclusions of the complete study will be drawn. Afterwards recommendations will be stated for further studies concerning the aerodynamics of heavy-duty vehicles and the tractor-trailer gap in particular.

6.1 Conclusions

6.1.1 Conclusions regarding the baseline configurations

The experimental results show that the drag coefficient of the baseline models with a small gap length (S-E and S-NE) or with no gap (NG) is significantly lower for all the tested yaw angles compared with the medium (M-E) and large (L-E) gap length baseline model. The wind averaged drag coefficient of the M-E and the L-E baseline model is respectively 0.592 and 0.546, while for the S-NE, the S-E and the NG baseline model the wind averaged drag coefficient is respectively 0.408, 0.390 and as well 0.390.

Both the experimental and the numerical results indicate that the aerodynamic performance of the average European heavy-duty vehicle nowadays driving on the road (S-E baseline model) lies closely to the aerodynamic performance of the ideal NG baseline model, which has no tractor-trailer gap. From a yaw angle of 0° till 9° the differences in drag coefficient measured during the wind tunnel experiment are negligibly small, only at a yaw angle of 12° the drag coefficient of the S-E baseline model is 47 drag counts (11.1%) larger than the drag coefficient of the NG baseline model.

The experimental results clearly show the benefit of adding extenders to cabin of the heavy-duty vehicle. At large yaw angles ($\geq 9^\circ$) the extenders clearly reduce the drag coefficient. The drag coefficient reduction at a yaw angle of 9° and 12° is respectively 40 drag counts (9.2%) and 179 drag counts (27.7%).

In general the drag coefficient increases with increasing yaw angle for all the baseline configurations. The differences between the different baseline configurations is more distinguishable at larger yaw angles.

The numerical simulations show that at a yaw angle of 0° a significant amount of air flows from the sides and the top of the cabin inside the tractor-trailer gap and impinges on the trailer frontal surface. Subsequently two large counter-rotating vortices develop inside the gap. When a large yaw angle is applied more air enters the gap from the windward side. Inside the gap a stream of air from the windward to the leeward side and only one large vortex are visible. Depending on the configuration and the yaw angle flow separation can occur at the leeward side of the trailer and/or cabin.

6.1.2 Conclusions regarding the drag reduction devices

The add-on devices are the most effective on the M-E and the L-E model, significantly more effective than on the S-NE and the S-E model. The drag reductions achieved by the add-on devices for the M-E model are in the range of 120 to 140 drag counts, for the L-E model in the range of 40-60 drag counts, for the S-NE model in the range of 10-22 drag counts and for the S-E model negligibly small.

Both the numerical and the experimental results confirm the effectiveness of the splitter plate as a drag reduction device for the tractor-trailer gap. According to the experimental results the splitter plate delivers the highest drag reduction of all tested add-on devices for the L-E and the M-E model with respectively a wind averaged drag coefficient reduction of 65 drag counts (11.9%) and 138 drag counts (23.3%). The numerical results show that during crosswind conditions the flow field is drastically changed when a splitter plate is attached to the trailer frontal surface. When a yaw angle is applied the splitter plate clearly reduces the crossflow in the tractor-trailer gap and eliminates or reduces the region of separated flow on the leeward side of the vehicle.

The experimental results show that regarding the S-NE model the most effective drag reduction devices are the cross vortex trap device and the vertical cylinders. The obtained wind averaged drag coefficient reduction with the cross vortex trap device is 21 drag counts (5.1%), with the vertical cylinders add-on device the drag reduction equals 22 drag counts (5.4%). These add-on devices are closely followed by the large side extenders and the splitter plate add-on device with a wind averaged drag coefficient reduction of respectively 20 drag counts (4.9%) and 18 drag counts (4.4%).

6.1.3 Conclusions regarding the analysis methods

The agreement between the numerical and experimental results heavily depends on the baseline model, the yaw angle and the presence of add-on devices. The trend of the drag coefficient matches well for the NG, S-E and the M-E baseline model, especially until a yaw angle of

9°. Regarding the L-E baseline model the trend is incorrectly predicted by the numerical simulations from a yaw angle of 3° onwards. The trend of the drag coefficient of the S-NE baseline model obtained by the numerical and the experimental method also does not match. However when the splitter plate or the rounded edges add-on device is attached to the baseline models, the drag coefficient is accurately predicted by the numerical simulations.

During the wind tunnel experiment pressure measurements were performed on the trailer frontal surface and on the cabin frontal curved surfaces of the L-E baseline model. Regarding the frontal curved surfaces the trend of the pressure coefficient on the windward side was well predicted by the numerical simulations, but incorrectly predicted on the leeward side of the vehicle. Also the trend of the pressure distribution on the trailer frontal surface is incorrectly predicted by the numerical simulations.

The reason of the large discrepancies between the numerical and the experimental results lies mainly in the numerical method. When the discrepancies are large the convergence history of the numerical simulation shows large oscillations. This means that the numerical method does not find a good solution. In these cases the numerical method predicts flow separation on the leeward side of the vehicle, while there is no indication from the experimental results that there is actual a region of separated flow on the leeward side.

The sensitivity and the reliability of the experimental measurements is also investigated. The standard deviation of the wind averaged drag coefficient of the L-E baseline model is determined to be 12 drag counts, which is the highest standard deviation of all the tested baseline models.

6.2 Recommendations

As the numerical method is not always capable of correctly predicting the drag and pressure coefficient, it is recommended to look into other numerical methods. An interesting follow-up research would be to investigate if LES, DES or LBM is better capable of correctly simulating the flow field.

Another recommendation is to perform PIV measurements on the tractor-trailer gap. In this way the hypothesis can be validated that CFD indeed incorrectly predicts flow separation on the leeward side of the vehicle when the discrepancies with the experimental results are large. Furthermore with the use of PIV the numerical results can be validated in more depth as then the numerical and experimental flow fields can be compared with each other. PIV can also give more insight in the reason why the M-E model has a higher drag coefficient compared with the L-E model at a yaw angle of 6° and 9°. This behavior was also observed by Hammache and Browand (2004), but they did not give any explanation for this particular behavior.

The pressure measurement system that was applied during the wind tunnel experiment could only measure one pressure tab at a time, which resulted in a very long total measurement time

per configuration. Hence, due to time constraints it was decided to only perform pressure measurements on the L-E baseline model. For future research it is recommended to use a faster pressure measurement system.

The supporting structure for the ground platform was handmade out of wooden beams. This construction was not very stable and had to be repaired multiple times during the wind tunnel campaign, which reduced the available time for performing tests. For future wind tunnel tests in the Open Jet Facility it is recommended to improve the supporting structure for the ground platform.

Although that many different drag reduction devices were tested on four different baseline models, it can be interesting to test some more concepts for the tractor-trailer gap. Furthermore the number of baseline models can be increased such that the effect of the gap length can be analyzed in more detail.

An interesting follow-up study would be to analyze the effect of the geometrical parameters of the add-on devices on the drag coefficient of the vehicle. In particular it would be interesting to optimize the geometry of the splitter plate as this is one of the most effective add-on devices.

Bibliography

H.J. Alons. OJF External Balance Documentation. Technical Report November, National Aerospace Laboratory NLR, 2008.

A. Altaf, A.A. Omar, and W. Asrar. Passive drag reduction of square back road vehicles. *Journal of Wind Engineering and Industrial Aerodynamics*, 134:30–43, 2014.

J.D. Anderson. *Fundamentals of Aerodynamics*. McGraw-Hill, New York, fifth edition, 2011.

D. Arcas, F. Browand, and M. Hammache. Flow Structure in the Gap Between Two Bluff Bodies. In *34th AIAA Fluid Dynamics Conference and Exhibit*, Portland, 2004.

F. Browand, C. Radovich, and M. Boivin. Fuel Savings by Means of Flaps Attached to the Base of a Trailer: Field Test Results. *SAE Technical Paper*, (2005-01-1016), 2005.

L. Buijs. Numerical and Experimental Analysis on Aerodynamic Solutions for Drag Reduction on Truck-Trailer Combinations. Master's thesis, TU Delft, 2010.

Carrier Transicold. Trailer Refrigeration Units. URL http://www.carrier.com/truck-trailer/en/eu/products/eu-truck-trailer/trailer/.

J. Chen, T. Song, and D. Wang. Research on Air Deflector Optimal Design and Matching for Heavy-Duty Vehicle Based on Design of Experiment Technology. *Applied Mechanics and Materials*, 404:188–193, September 2013.

H. Choi, J. Lee, and H. Park. Aerodynamics of Heavy Vehicles. *Annual Review of Fluid Mechanics*, 46:441–468, 2014.

R.H. Croll, W.T. Gutierrez, B. Hassan, J.E. Suazo, and A.J. Riggins. Experirmental Investigation of the Ground Transportation Systems (GTS) Project for Heavy Vehicle Drag Reduction. *SAE Technical Paper*, (960907), 1996.

P. Das, M. Tsubokura, T. Matsuuki, N. Oshima, and K. Kitoh. Large Eddy Simulation of the Flow-Field around a Full-Scale Heavy-Duty Truck. In *Procedia Engineering*, volume 56, pages 521–530. Elsevier B.V., 2013.

Don-Bur. Aeris, 2015. URL http://www.donbur.co.uk/gb-en/docs/150327-Don-Bur-Aeris-Brochure.pdf.

E. Elofsson. Investigation of Flow Separation around the Front Corners of a Truck using CFD. Master's thesis, 2014.

ETSU and MIRA. Good Practice Guide: Truck aerodynamic styling, 2001. URL http://www.transport-research.info/Upload/Documents/200602/20060210_121817_04842_GPG308.pdf.

European Commission. *EU Transport in Figures: Statistical Pocketbook 2014*. Publications Office of the European Union, 2014.

B. F. R. Ewald. *Wind Tunnel Wall Corrections*. 1998.

Exa Corporation. PowerFLOW. URL http://exa.com/product/simulation-tools/powerflow-cfd-simulation.

Faber Maunsell. Reducing Greenhouse Gas Emissions from Heavy-Duty Vehicles. Technical Report March, AECOM, Altrincham, 2008. URL http://ec.europa.eu/clima/policies/transport/vehicles/heavy/index_en.htm.

Fluent Inc. FLUENT 6.3 Users Guide. Technical report, 2006.

M.J.A. Freeman and C.J. Roy. Application of Optimization Under Uncertainty: 2-D Tractor-Trailer Base Flaps. In *50th AIAA Aerospace Sciences Meeting including the New Horizons Forum and Aerospace Exposition*, Nashville, a.

M.J.A. Freeman and C.J. Roy. Global Optimization Under Uncertainty for Tractor-Trailer Base Flaps. In *51st AIAA Aerospace Sciences Meeting including the New Horizons Forum and Aerospace Exposition*, Grapevine (Dallas/Ft. Worth Region), b.

T. Gheyssens. Aerodynamic Analysis of a Platoon of Bluff Bodies Subjected to Cross Wind, a Numerical Investigation on the Effect of Drag Reduction Devices. Master's thesis, 2016.

M. Hammache and F. Browand. On the Aerodynamics of Tractor-Trailers. In *The Aerodynamics of Heavy Vehicles: Trucks, Buses, and Trains*, pages 185–205. Springer Berlin Heidelberg, 2004.

J.T. Heineck, S.M. Walker, and D. Satran. The Measurement of Wake and Gap Flows of the Generic Conventional Truck Model (GCM) using Three-Component PIV. In *Aerodynamic of Heavy Duty Vehicles: Trucks, Buses and Trains*, pages 173–184. Springer Berlin Heidelberg, 2004.

M. Heinecke, J. Beedy, K. Horrigan, and R. Sengupta. Aerodynamic Study of a Production Tractor Trailer Combination using Simulation and Wind Tunnel Methods. *SAE Technical Paper*, (2010-01-2040), 2010.

L. Hjelm and B. Bergqvist. European Truck Aerodynamics - A Comparison Between Conventional and CoE Truck Aerodynamics and a Look into Future Trends and Possibilities. In *The Aerodynamics of Heavy Vehicles II: Trucks, Buses, and Trains*, pages 469–477. Springer Berlin Heidelberg, 2009.

K. Horrigan, B. Duncan, P. Sivakumar, A. Gupta, and A. Wong. Aerodynamic Simulations of a Class 8 Heavy Truck: Comparison to Wind Tunnel Results and Investigation of Blockage Influences. *SAE Technical Paper*, (2007-01-4295), 2007.

K. Horrigan, B. Duncan, A. Keating, A. Gupta, and J. Gargoloff. Aerodynamic Simulations of a Generic Tractor-Trailer: Validation and Analysis of Unsteady Aerodynamics. *SAE Technical Paper*, (2008-01-2612), 2008.

D. Hyams, K. Sreenivas, R. Pankajakshan, D. Stephen Nichols, W. Roger Briley, and D.. Whitfield. Computational simulation of model and full scale Class 8 trucks with drag reduction devices. *Computers and Fluids*, 41(1):27–40, 2011.

Moni Islam, Friedhelm Decker, Michael Hartmann, Anke Jaeger, Timo Lemke, Joerg Ocker, Volker Schwarz, Frank Ullrich, B Crouse, G Balasubramanian, and F Mendonca. Investigations of Sunroof Buffeting in an Idealised Generic Vehicle Model - Part II: Numerical Simulations. In *14th AIAA/CEAS Aeroacoustics Conference (29th AIAA Aeroacoustics Conference)*, number 2901, Vancouver, 2008.

J. Kim, S. Hahn, J. Kim, D. Lee, J. Choi, W. Jeon, and H. Choi. Active control of turbulent flow over a model vehicle for drag reduction. *Journal of Turbulence*, 5(19):1–12, May 2004.

M. Kim. Numerical Simulation on the Aerodynamic Characteristics Around Corner Vane of a Heavy-Duty Truck. *SAE Technical Paper*, (2000-01-3499), 2000.

Klicktel. Rohstoffe Graf Containerdienst, 2016. URL https://www.klicktel.de/branchenbuch/lingenfeld/06037105823760822/rohstoffe-graf-containerdienst.html.

S. Krajnovic and L. Davidson. Development of Large-Eddy Simulation for Vehicle Aerodynamics. In *ASME 2002 International Mechanical Engineering Congress and Exposition; Heat Transfer, Volume 2*, pages 165–172, New Orleans, 2002. ASME.

M.J. Krause. OpenLB is .... URL http://optilb.org/openlb/.

Laydon Composites Ltd. Nose Fairing and Vortex Stabilizer. URL http://www.laydoncomp.com/nose-fairing-vortex-stabilizer.php.

J. Leuschen and K.R. Cooper. Full-Scale Wind Tunnel Tests of Production and Prototype, Second-Generation Aerodynamic Drag-Reducing Devices for Tractor-Trailers. *SAE Technical Paper*, (2006-01-3456), 2006.

S. Maddox, K.D. Squires, K.E. Wurtzler, and J.R. Forsythe. Detached-Eddy Simulation of the Ground Transportation System. In *The Aerodynamics of Heavy Vehicles: Trucks, Buses, and Trains*, pages 89–104. Springer Berlin Heidelberg, 2004.

V. Malviya, R. Mishra, and J. Fieldhouse. CFD Investigation of a Novel Fuel-Saving Device for Articulated Tractor-Trailer Combinations. *Engineering Applications of Computational Fluid Mechanics*, 3(4):587–607, 2009.

B.R. McAuliffe, L. Belluz, and M. Belzile. Measurement of the On-Road Turbulence Environment Experienced by Heavy Duty Vehicles. *SAE International Journal of Commercial Vehicles*, 7(2):685–702, 2014.

J.D. Miller and C. Façanha. The state of clean transport policy: a 2014 synthesis of vehicle and fuel policy developments. Technical report, The International Counsil on

Clean Transportation (ICCT), Washington DC, 2014. URL http://www.theicct.org/state-of-clean-transport-policy-2014.

J. Ortega, K. Salari, and B. Storms. Investigation of Tractor Base Bleeding for Heavy Vehicle Aerodynamic Drag Reduction. In *The Aerodynamics of Heavy Vehicles II: Trucks, Buses, and Trains*, pages 161–178. Springer Berlin Heidelberg, 2009.

J. Ortega, K. Salari, A. Brown, and R. Schoon. Aerodynamic drag reduction of class 8 heavy vehicles: a full-scale wind tunnel study. Technical report, Lawrence Livermore National Laboratory (LLNL), Livermore, CA, 2013. URL https://e-reports-ext.llnl.gov/pdf/741852.pdf.

J. M. Ortega and K. Salari. Investigation of a Trailer Underbody Fairing for Heavy Vehicle Aerodynamic Drag Reduction. *SAE Technical Paper*, (2008-01-2601), 2008.

J.M. Ortega and K. Salari. An Experimental Study of Drag Reduction Devices for a Trailer Underbody and Base. In *34th AIAA Fluid Dynamics Conference and Exhibit*, Portland, 2004.

Palabos. Palabos - CFD, Complex Physics. URL http://www.palabos.org/.

W.D. Pointer. Evaluation of Commercial CFD Code Capabilities for Prediction of Heavy Vehicle Drag Coefficients. *34th AIAA Fluid Dynamics Conference and Exhibit*, (July): 1–10, 2004. URL http://arc.aiaa.org/doi/abs/10.2514/6.2004-2254.

W.D. Pointer, T. Sofu, J. Chang, and D. Weber. Applicability of Commercial CFD Tools for Assessment of Heavy Vehicle Aerodynamic Characteristics. In *The Aerodynamics of Heavy Vehicles II: Trucks, Buses, and Trains*, pages 349–361. Springer Berlin Heidelberg, 2009.

S.B. Pope. *Turbulent Flows*. Cambridge University Press, 2000.

SAE. SAE Wind Tunnel Test Procedure for Trucks and Buses (J1252). Technical report, 2012.

SAE. Guidelines for Aerodynamic Assesment of Medium and Heavy Commercial Ground Vehicles Using Computational Fluid Dynamics (J2966). Technical report, 2013.

A. Seifert, O. Stalnov, D. Sperber, G. Arwatz, V. Palei, S. David, I. Dayan, and I. Fono. Large Trucks Drag Reduction Using Active Flow Control. In *46th AIAA Aerospace Sciences Meeting and Exhibit*, Reno, 2008.

B. Storms and J. Ross. Aerodynamic Drag Reduction of the Underbody of a Class-8 Tractor-Trailer. *SAE Technical Paper*, (2006-01-3532), 2006.

B. Storms, D. Satran, J. Heineck, and S. Walker. A Summary of the Experimental Results for a Generic Tractor-Trailer in the Ames Research Center 7- by 10-Foot and 12-Foot Wind Tunnels. Technical Report July, NASA Ames Research Center, 2006.

B.L. Storms, D.R. Satran, J.T. Heineck, and S.M. Walker. A Study of Reynolds Number Effects and Drag-Reduction Concepts on a Generic Tractor-Trailer. In *34th AIAA Fluid Dynamics Conference and Exhibit*, Portland, 2004.

TU Delft. Open Jet Facility (HSL), 2015. URL http://www.lr.tudelft.nl/organisatie/afdelingen/aerodynamics-wind-energy-flight-performance-and-propulsion/facilities/wind-tunnel-lab/open-jet-facility-hsl/.

K. Van Ginderdeuren. Design of Guiding Vanes for Bluff Bodies with the aid of Computational Fluid Dynamics. Master's thesis, TU Delft, 2010.

P.M. van Leeuwen. Computational Analysis of Base Drag Reduction Using Active Flow Control. Master's thesis, TU Delft, 2009.

G.M.R. Van Raemdonck. *Design of Low Drag Bluff Road Vehicles*. PhD thesis, TU Delft, 2012.

G.M.R. Van Raemdonck and M.J.L. Van Tooren. Time-Averaged Phenomenological Investigation of a Wake behind a Bluff Body. In *BBAA VI International Colloquium on: Bluff Bodies Aerodynamics & Applications*, Milano, 2008.

S.P. Veluri, C.J. Roy, A. Ahmed, R. Rifki, J.C. Worley, and B. Recktenwald. Joint Computational/Experimental Aerodynamic Study of a Simplified Tractor/Trailer Geometry. *Journal of Fluids Engineering*, 131(8):081201, 2009.

Thomas Welfers, Sven Ginsberg, Michael Funcke, Michael Hamcher, and Ralf Matheis. Design of a Tractor for Optimised Safety and Fuel Consumption (No. 104190). Technical report, Forschungsgesellschaft Kraftfahrwesen mbH Aachen (FKA), Aachen, 2011.

F.M. White. *Viscous Fluid Flow*. McGraw-Hill, third edition, 2006.

R.M. Wood. Impact of Advanced Aerodynamic Technology on Transportation Energy Consumption. *SAE Technical Paper*, (2004-01-1306), 2004.

R.M. Wood. Cross flow vortex trap device and method for reducing the aerodynamic drag of ground vehicles. United States Patent 6986544, 2006.

R.M. Wood and S.X.S. Bauer. Simple and Low-Cost Aerodynamic Drag Reduction Devices for Tractor-Trailer Trucks. *SAE Technical Paper*, (2003-01-3377), 2003.

Appendix A

Technical drawings

A.1 The S-E model

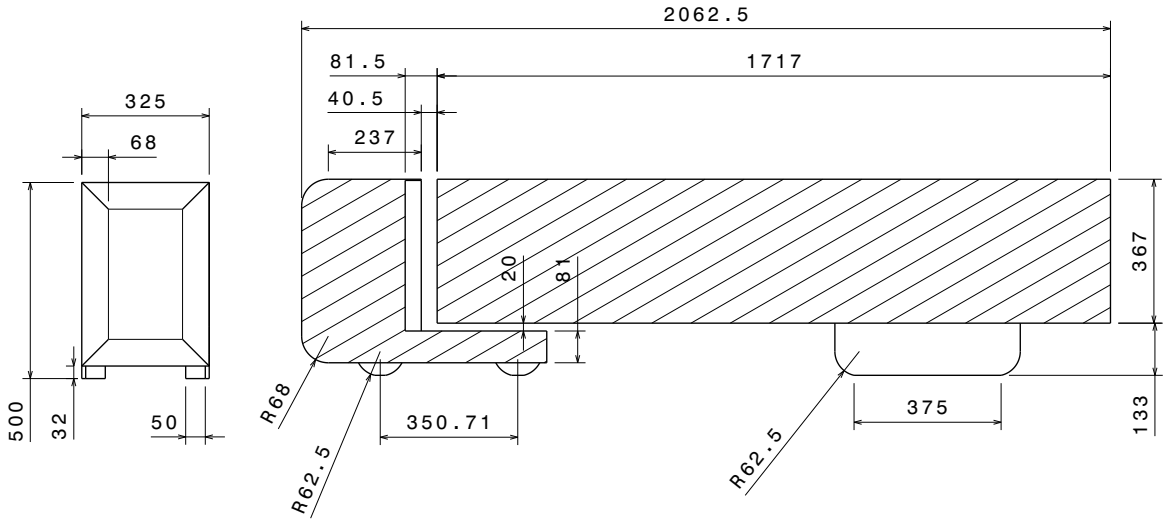

Figure A.1: Front view and cross-section of the 1:8 S-E test model [mm]

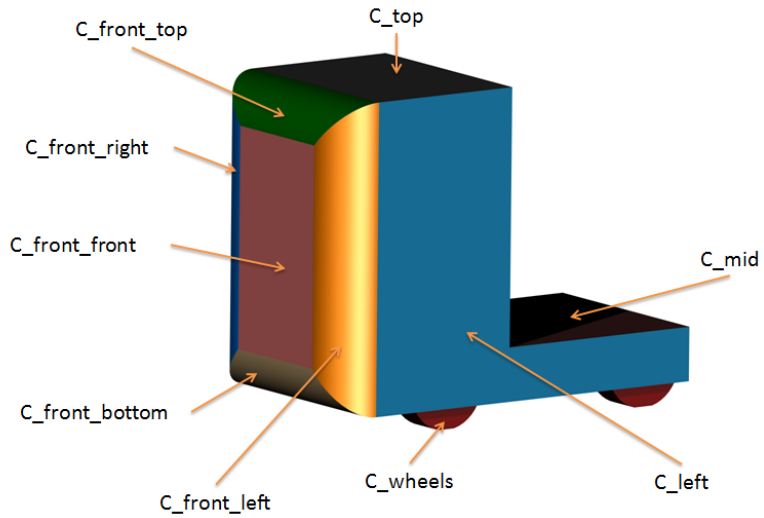

Figure A.2: Parts of the trailer of the S-E model (front view)

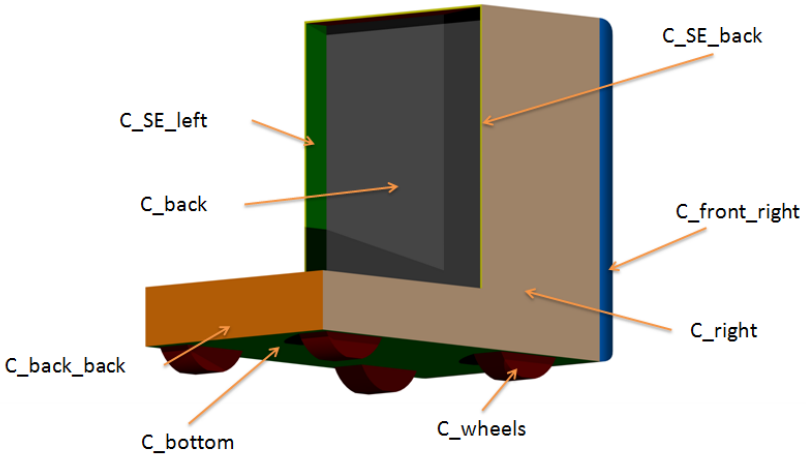

Figure A.3: Parts of the trailer of the S-E model (back view)

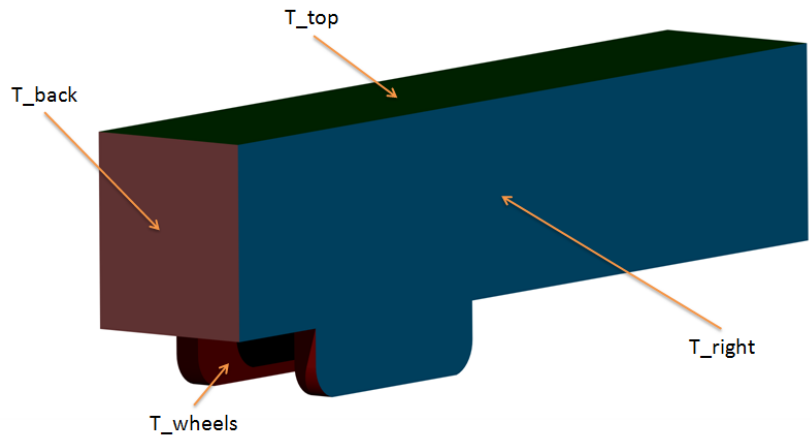

Figure A.4: Parts of the trailer of the S-E model

A.2 Pressure tabs

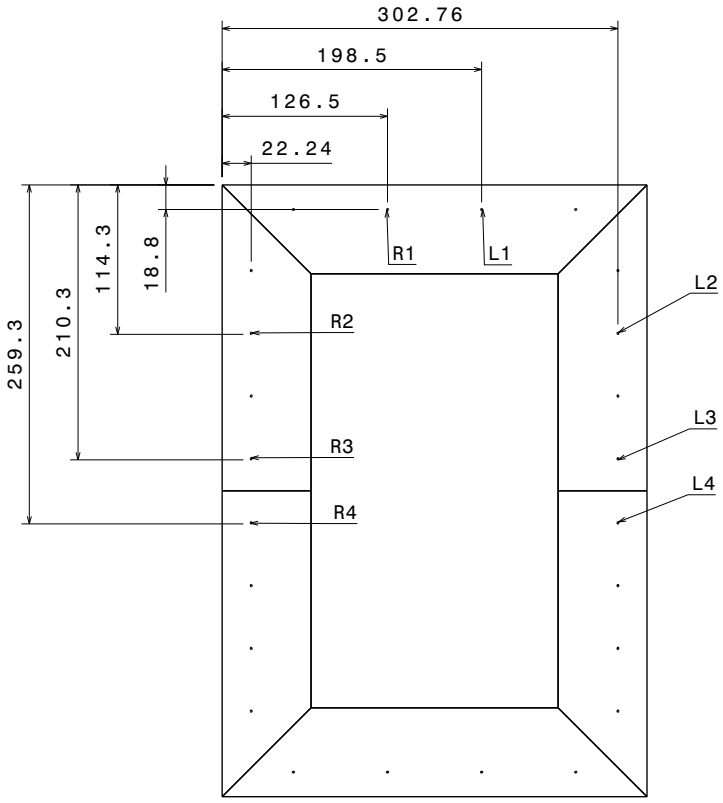

Figure A.5: Pressure tabs locations on the cabin frontal surface of the 1:8 wind tunnel test model [mm]

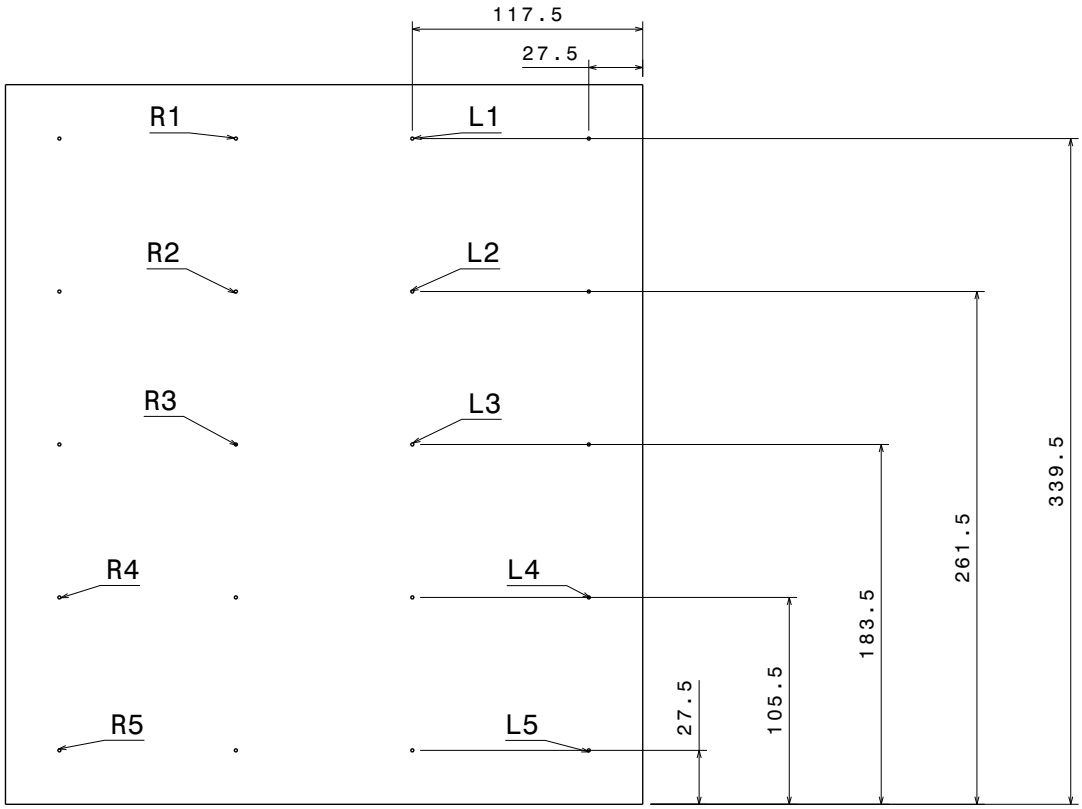

Figure A.6: Pressure tabs locations on the trailer frontal surface of the 1:8 wind tunnel test model [mm]

A.3 Wind tunnel test set-up

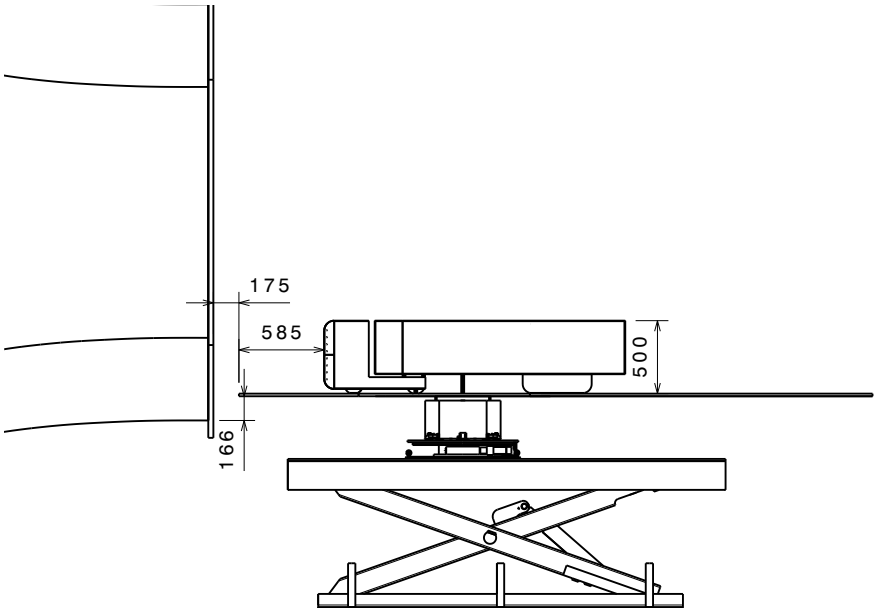

Figure A.7: Side view of the wind tunnel test set-up [mm]

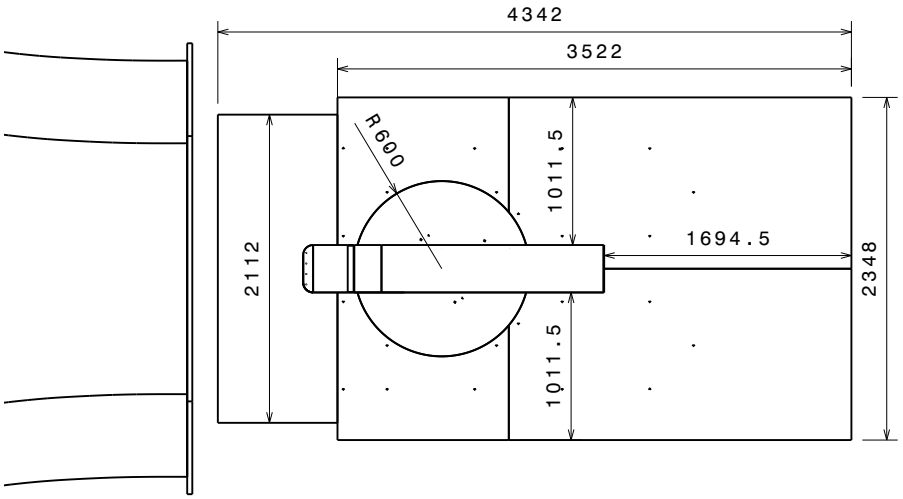

Figure A.8: Top view of the wind tunnel test set-up [mm]